Nonequilibrium dynamics of colloids

Von der Fakultät Mathematik und Physik der Universität Stuttgart
zur Erlangung der Würde eines Doktors der Naturwissenschaften (Dr. rer. nat.)
genehmigte Abhandlung

vorgelegt von

Boris Lander

aus Ludwigsburg

Hauptberichter: Prof. Dr. Udo Seifert
Mitberichter: Jun.-Prof. Dr. Axel Arnold

Tag der Einreichung: 09. April 2013
Tag der mündlichen Prüfung: 08. Mai 2013

II. Institut für Theoretische Physik der Universität Stuttgart

2013

Contents

List of Figures

Notations and symbols

Abbreviations

ATP	adenosine triphosphate
bcc	body-centered cubic
CNT	classical nucleation theory
fcc	face-centered cubic
FDR	fluctuation-dissipation ratio
FDT	fluctuation-dissipation theorem
FT	fluctuation theorem
hcp	hexagonal close packed
liq	liquid
NESS	nonequilibrium steady state
pdf	probability density function
pre	pre-structured
sol	solid

Symbols

a, A, A_i, $\mathcal{A}$	particle diameter, generic observable, amplitude, action functional
B, B^{eq}	magnetic field strength/conjugate quantity in the FDT, in thermal equilibrium
c_i, $\bar{c}_i(n)$	population in state i, average population in state i
C, C^{eq}, χ	correlation function, in thermal equilibrium, magnetic polarizability
$\mathbf{d}$, D_0, D_{ij}	spurious drift, bare diffusion constant, diffusion tensor
ϵ	energy at contact
$\mathbf{F}$, $\mathbf{F}^{\mathrm{int}}$, $\mathbf{F}^{\mathrm{ext}}$	force, interaction, external
$f_{i\to j}$	particle flux from state i to j
$\mathcal{F}$, $\Delta\mathcal{F}$	free energy, free energy barrier
ϕ, ϕ_i	volume fraction, phase shift

g, G, G_{ij}	pair distribution function, Green's function, symmetric matrices
$\dot{\gamma}$, γ_s, Γ	strain rate, surface tension, coupling constant
η	dynamic viscosity
I	excess term in the FDT in a NESS
j, j^s, $\mathcal{J}$	probability current, stationary current, Jacobian
k, κ	stiffness of harmonic potential, inverse screening length of Yukawa potential
λ	control parameter/eigenvalue
m, M	mass, magnetic moment
μ, μ_0, μ_{ij}, $\Delta\mu$	magnetic constant, bare mobility, mobility tensor, chemical potential difference
n, n^*	size of the largest cluster, critical cluster size
N, N_b, $\mathcal{N}$	number of particles/degrees of freedom, list of neighbors, normalization constant
ν, ν^s, $\tilde{\nu}^\mathrm{s}$, $\nu(n)$	mean local velocity, stationary, of accessible degrees of freedom, growth rate
ω	frequency
Ω, Ω_0, $\Delta\Omega$	average local heat production rate with and without hydrodynamic interaction, additional local heat production rate caused by hydrodynamic interaction
p, P, Ψ, Ψ^s	probability, path weitght, pdf, stationary pdf
q, $\bar{q}_l$, q_{lm}, $\bar{q}_{lm}$	heat, order parameters
$\mathbf{r}$, $\mathbf{R}$	position, configuration space vector
R_b, Re	range for set of neighbors, Reynolds number
R, R^eq	linear response function, in thermal equilibrium
ρ, ρ_fl	density, density in a fluid
$S_{ij}^{(l)}$	normalized scalar product used for bonding criterion
s, s_tot, s_m, $\tilde{s}_\mathrm{tot}$	stochastic, total, medium, apparent entropy
θ	kinetic temperature
T, T	temperature, transfer matrix
t, τ_m, τ_D, τ^*	time, relaxation time of momenta, diffusive time scale, duration of crystallization
$\mathbf{u}$, $\mathbf{u}^\mathrm{hyd}$	external flow field, hydrodynamic flow field
u, U	pair potential, internal energy/potential
$\mathbf{v}$, v^s, $\tilde{v}$, $\mathbf{V}$, V	velocity, mean, relative, velocity configuration vector, volume
W	dipole-dipole interaction potential
w, $w(t)$, $\mathbf{w}^{(0)}$, $\bar{w}_l$ ..	work, Wiener process, eigenvector, order parameter
x, $\mathcal{X}$, $\mathcal{X}^\mathrm{c}$, $\boldsymbol{\xi}$	generic variable, path, conjugate path, stochastic force

X, X^{eq}	fluctuation-dissipation ratio, in thermal equilibrium
Y_{lm}	spherical harmonics
Z_n, $\boldsymbol{\zeta}$	normalization constant, stochastic velocity

Operators and mathematical notations

$\bar{f}$	Fourier transform of a function f
$\cdot^{\mathrm{T}}$	transposition operator
$\mathrm{d}, \mathrm{đ}$	complete, incomplete differential
δ_{ij}, $\delta(t)$	Kronecker symbol, Dirac distribution
$\mathcal{O}(\cdot)$	Landau symbol
$\langle\cdot\rangle$, $\langle\cdot\rangle_{\mathrm{eq}}$, $\langle\cdot\rangle^h$	ensemble average, in thermal equilibrium, in a system perturbed by h
$\boldsymbol{\nabla}$, ∂_x	gradient operator, derivative with respect to x
$\mathbb{1}$	identity matrix
$\partial_t A \equiv \dot{A}$	time derivative of A
$p(x)$, $P[\mathcal{X}]$	probability for x, pathweight for $\mathcal{X}$
Tr	trace operator
$\mathbf{x} \equiv (x_i)$, $\mathsf{X} \equiv (x_{ij})$	vector, matrix
$f[\mathcal{X}]$	functional f of $\mathcal{X}$
f'	real part of a function f

Kurzfassung

Diese Arbeit beschäftigt sich mit der Dynamik kolloidaler Systeme unter verschiedenartigen Nichtgleichgewichtsbedingungen. Kolloide bestehen im Allgemeinen aus Teilchen oder Tröpfchen, die fein in einem sogenannten Dispersionsmedium wie beispielsweise Wasser verteilt sind. Sie gehören zur Klasse der mesoskopischen Systeme, deren charakteristische Längenskala sich von einigen Nanometern bis hin zu einigen Mikrometern erstreckt. Neben Kolloiden umfassen mesoskopische Systeme eine Vielzahl interessanter Objekte angefangen von Proteinen über molekulare Motoren, bis hin zu lebenden Organismen wie Bakterien [1]. Zwei Eigenschaften sind für solche Systeme charakteristisch. Erstens ist mit der kleinen Längenskala zumeist auch eine entsprechend kleine Energieskala verbunden, die sich im Bereich der thermischen Energie bewegt. Damit kommt thermischen Fluktuationen eine entscheidende Rolle zu. Zweitens sind insbesondere biologische Systeme oft fernab des thermischen Gleichgewichts angesiedelt. Da die klassische Thermodynamik weder Fluktuationen beinhaltet noch für die Behandlung von Nichtgleichgewichtszuständen ausgelegt ist, ist sie für die Beschreibung solcher Systeme ungeeignet. Die *stochastische Thermodynamik* behebt diese beiden Probleme indem sie thermodynamische Konzepte wie Arbeit, Wärme oder Entropie unter relativ allgemeinen Nichtgleichgewichtsbedingungen auf der Ebene einzelner Trajektorien beschreibt. Eckpfeiler dieser Theorie sind der erste Hauptsatz entlang fluktuierender Pfade [2] sowie die Definition einer stochastischen Entropie auf Trajektorienebene [3]. Wesentlich ist in diesem Zusammenhang, dass die stochastische Thermodynamik lediglich die Kopplung an ein Wärmebad erfordert, das sich im thermischen Gleichgewicht befindet. Das mesoskopische System ist in dieser Hinsicht keinerlei Einschränkung unterworfen.

Durch die Entwicklung optischer Pinzetten [4, 5] und der Rasterkraftmikroskopie [6] wurde die Manipulation und Beobachtung mesoskopischer Systeme auf experimenteller Ebene möglich. Kolloide nehmen im Hinblick auf die stochastische Thermodynamik insofern eine exponierte Rolle ein, als dass sich mit ihnen experimentell gut kontrollierbare Systeme mit wenigen Freiheitsgraden kreieren lassen mit denen man fundamentale Fragestellungen angehen und theoretische Vorhersagen testen kann [7, 8]. Andererseits sind Kolloide auch für komplexe Fragestellungen gut geeignet, da sie ebenso in Form von wechselwirkenden Vielteilchensystemen auftreten, die auch in technischen Anwendungen eine Rolle spielen können [9].

Ziel dieser Arbeit ist es, verschiedene Aspekte der Dynamik kolloidaler Systeme abseits des thermischen Gleichgewichts zu beleuchten. Dazu gehören einerseits fundamentale Problemstellungen der stochastischen Thermodynamik, wie etwa die Messung von Dissipationsraten oder die Rolle von verdeckten Freiheitsgraden, andererseits aber auch die Untersuchung kollektiver Phänomene, die erst durch das Zusammenspiel vieler Freiheitsgrade zustande kommen. Beispiele hierfür sind die Suche nach einer effektiven Nichtgleichgewichtstemperatur oder die Bildung von Kolloidkristallen. Um diese Fragestellungen anzugehen, verwenden wir zwei Systeme. Das erste besteht aus zwei miteinander wechselwirkenden kolloidalen Teilchen, die mittels einer optischen Pinzette auf zwei separate Kreisbahnen gezwungen werden. Mit diesem experimentell gut kontrollierbaren Aufbau werden wir die grundlegenderen Problemstellungen dieser Arbeit angehen. Das zweite System ist eine kolloidale Suspension, die zur Klasse der wechselwirkenden Vielteilchensysteme gehört. Wir setzen diese Suspension einem externen Scherfluss aus und treiben es damit aus dem thermischen Gleichgewicht. Wir nutzen dieses System, um Nichtgleichgewichtseffekte zu untersuchen, die sich aus dem Zusammenspiel vieler Teilchen ergeben.

Kapitel 2: Brownsche Dynamik.– Kapitel 2 gibt einen kurzen Überblick über die dynamischen Grundgleichungen, die für die restlichen Kapitel benötigt werden. Dazu gehören die Langevin Gleichung, die Fokker-Planck Gleichung sowie ein Pfadintegralzugang zur Beschreibung diffundierender Systeme. Detaillierte Darstellungen finden sich in einschlägigen Lehrbüchern [10–13].

Kapitel 3: Dissipation.– Um auf eine umfassende Beschreibung des Nichtgleichgewichts hinzuarbeiten, ist es sinnvoll mit Zuständen zu beginnen, die dem Gleichgewicht am ähnlichsten sind. Stationäre Nichtgleichgewichtszustände (NESS[1]) erfüllen diese Anforderung insofern, als dass sich ihre Eigenschaften zeitlich nicht ändern. Der entscheidende Punkt, der solche Zustände von Gleichgewichtszuständen unterscheidet, ist die ständige Dissipation von Wärme. Die Messung der Dissipationsrate in Experimenten ist daher ein wichtiger Aspekt bei der Charakterisierung eines NESS. Während die Messung der dissipierten Wärme in makroskopischen Systemen über kalorimetrische Methoden realisiert werden kann, ist dies in mesoskopischen Systemen wegen der sehr kleinen Dissipationsraten nicht möglich. Der derzeit einzige Weg, Dissipation in mesoskopischen Systemen zu messen, nutzt, neben Korrelationsfunktionen, die lineare Antwort des Systems auf externe Störungen [14]. In kolloidalen Systemen ist die experimentelle Bestimmung Letzterer jedoch häufig ein schwieriges und aufwändiges Unterfangen. Die Aufzeichnung von Trajektorien kolloidaler Teilchen hingegen ist leicht und präzise durchführbar. In

[1] nonequilibrium steady state

Kapitel 3 stellen wir eine Methode vor wie Dissipationsraten allein aus den Trajektorien der kolloidalen Teilchen erschlossen werden können [15]. Dabei muss das System in keinerlei Form gestört werden. Wir testen diese Methode anhand einer überdämpften Langevindynamik-Simulation des oben beschriebenen kolloidalen Zweiteilchensystems und wenden sie auf experimentelle Daten[2] an. Darüber hinaus zeigen wir wie sich hydrodynamische Wechselwirkungen in die Methode integrieren lassen, ohne dass zusätzliche Messdaten erforderlich werden.

Kapitel 4: Verdeckte Freiheitsgrade.– Die Beschreibung mesoskopischer Systeme erfolgt in der Regel auf eine vergröberte Art und Weise, wie etwa in der Langevin Gleichung [10], die die Lösungsmittelteilchen bei der Diffusion eines kolloidalen Teilchens als effektiv weißes Rauschen beschreibt. Eine solche effektive Beschreibung von Freiheitsgraden ist in der Regel dann gerechtfertigt, wenn eine klare Zeitskalenseparation in der Dynamik beobachteter und verdeckter Freiheitsgrade vorliegt. Ist dies nicht der Fall, kann es zu Inkonsistenzen und Widersprüchen kommen. In Kapitel 4 untersuchen wir diesen Sachverhalt für die Entropieproduktion in einem NESS [16]. Konkret betrachten wir für das oben beschriebene Zweiteilchensystem das Fluktuations-Theorem (FT) [3], welches eine tiefe Symmetriebeziehung für die Verteilung der Fluktuationen der Entropieproduktion beschreibt. Bezieht man in die Berechnung der Entropieproduktion nur eines der beiden Teilchen mit ein, lässt die Wechselwirkung mit dem zweiten (verdeckten) Teilchen aber dennoch bestehen, so erhält man eine *scheinbare* Entropieproduktion, für die die Voraussetzungen des FT verletzt sind. Es stellt sich heraus, dass die scheinbare Entropie dennoch näherungsweise eine solche FT-artige Symmetrie erfüllt. Wir diskutieren warum dieser Befund sowohl für kleine als auch für große Entropiefluktuationen typisch ist, während im Übergangsbereich Abweichungen zu erwarten sind. Für eine spezielle Wahl der Parameter lassen sich diese Abweichungen klar herausstellen. Für den Fall der Entropieproduktion in sehr kurzen Zeitintervallen zeigen wir zudem, dass auch die *scheinbare* Entropieproduktion ein exaktes FT erfüllt.

Kapitel 5: Effektive Temperatur und das Fluktuations-Dissipations-Verhältnis.– Im Gleichgewicht ist die Temperatur eng mit dem Fluktuations-Dissipations-Theorem (FDT[3]) verbunden und kann über das sogenannte Fluktuations-Dissipations-Verhältnis (FDR[4]) bestimmt werden. Das FDT verbindet Gleichgewichtsfluktuationen mit der linearen Antwort eines Systems auf externe Stör-

[2] Alle experimentellen Daten, die in dieser Arbeit verwendet werden, wurden von J. Mehl bereitgestellt.

[3] fluctuation-dissipation theorem

[4] fluctuation-dissipation ratio

ungen, während das FDR korrespondierende Korrelations- und Antwortfunktionen ins Verhältnis setzt. Im Nichtgleichgewicht gilt das FDT in dieser Form nicht mehr, ebenso verliert das Temperaturkonzept seine Gültigkeit. Für kleine Störungen eines NESS lässt sich jedoch noch immer eine lineare Antwort definieren. Gemeinsam mit den in NESSs ebenfalls gültigen Korrelationsfunktionen erhält man damit auch im stationären Nichtgleichgewicht ein wohldefiniertes FDR. Es ist daher ein naheliegender Ansatz, über das FDR eine effektive Temperatur für solche Zustände einzuführen [17]. Kürzlich wurde gezeigt, dass das FDT in NESSs im Allgemeinen einen additiven Korrekturfaktor beinhaltet, der nur ein zeitabhängiges FDR zulässt [18–23]. Eine sinnvolle Temperaturdefinition über das FDR schlägt damit fehl. In Gläsern und unterkühlten Suspensionen wurden jedoch FDRs beobachtet die im Langzeitlimes näherungsweise zeitunabhängig werden [24, 25].

In Kapitel 5 verfolgen wir die Bewegung eines zufällig gewählten Teilchens einer gescherten kolloidalen Suspension in einer Langevindynamik-Simulation. Konkret untersuchen wir Geschwindigkeitskorrelationen und die lineare Antwort der Geschwindigkeit dieses Teilchens auf eine kleine Kraftstörung. Für moderate Dichten finden wir für das zugehörige FDR einen näherungsweise zeitunabhängigen Verlauf [26]. Hierbei beobachten wir dieses Verhalten nicht für das Langzeitverhalten des FDRs, sondern für die anfängliche Relaxation der Korrelations- und Antwortfunktionen. Darüber hinaus untersuchen wir ein einfaches Modellsystem bestehend aus einem einzelnen Teilchen in einer harmonischen Falle ebenfalls im linearen Scherfluss. Auch für dieses System beobachten wir ein näherungsweise zeitunabhängiges FDR für große Fallenstärken. Um einen Einblick in den Ursprung dieses Befundes zu erhalten, leiten wir das FDT in einer hybriden Form her, die sowohl additive als auch multiplikative Anteile beinhaltet. Für beide Systeme führt ein räumliches Einschränken der Bewegungsfreiheit der Teilchen dazu, dass der additive Anteil vernachlässigbar und damit das FDR näherungsweise konstant wird. Darüber hinaus untersuchen wir die mit dem FDT eng verwandte Einstein-Relation, die im Gleichgewicht die Mobilität und die Diffusionskonstante des kolloidalen Teilchens in Verbindung setzt [27]. Über eine effektive Einstein-Relation, die das zuvor bestimmte, näherungsweise konstante FDR entält, finden wir auch im gescherten System eine approximative Verknüpfung dieser beiden Größen.

Kapitel 6: Scherinduzierte Kristallisation.– Im letzten Kapitel verlassen wir die Domäne der stationären Zustände und widmen uns der zeitlichen Entwicklung eines Systems aus einem metastabilen Zustand heraus. Genauer gesagt untersuchen wir den Kristallisationsprozess in einer übersättigten kolloidalen Suspension im Scherfluss. Bisherige Arbeiten haben noch kein abschließendes Ergebnis über den Einfluss der Scherung auf die Entwicklung eines Kristalls geliefert. Einerseits wurde berichtet, dass ein linearer Scherfluss die Kristallisation erle-

ichtert [28–34], andererseits davon, dass die Kristallisation durch Scherung erschwert wird [35–37]. Auch optimale Scherraten für den Kristallisationsprozess wurden beobachtet [38–43].

In diesem Kapitel verwenden wir eine Langevindynamik-Simulation, um diese Fragestellung zu untersuchen [44]. Wir beobachten eine maximale Kristallisationsrate bei einer endlichen Scherrate und erklären dies dadurch, dass sich der Scherfluss auf unterschiedliche Phasen der Kristallisation in unterschiedlicher Weise auswirkt. Zu Beginn der Kristallisation, d. h. in der Keimbildungsphase, erschwert der Scherfluss die Bildung kristalliner Nuklei. Während der Wachstumsphase des Kristalls hingegen beschleunigt der Scherfluss den Prozess. Um die zugrunde liegenden Mechanismen zu analysieren verwenden wir ein diskretes Zustandsmodell. Der Zustandsraum umfasst dabei fünf Zustände, denen Teilchen je nach Konfiguration ihrer direkten Umgebung zugeordnet werden. Dabei unterscheiden wir die Zustände flüssig, vorstrukturiert sowie die drei kristallinen Gitterformen hcp[5], bcc[6] und fcc[7]. Eine Diskussion der Übergangsraten ergibt, dass die erschwerte Nukleation durch die Zerstörung noch relativ loser Strukturen in der Flüssigkeit verursacht wird, während die Scherkräfte nicht stark genug sind, bereits bestehende Nuklei in ihrem Wachstum nachhaltig zu beeinträchtigen. Für das beschleunigte Wachstum extrahieren wir die funktionale Abhängigkeit der Wachstumsrate vom Scherfluss aus den Simulationsdaten. Mittels eines einfachen Modells bringen wir diese funktionale Form mit der durch den Scherfluss verursachten Konvektion in Verbindung. Zudem diskutieren wir den Einfluss der Scherung auf die Zusammensetzung kristalliner Cluster. Eine Erhöhung der Scherrate stabilisiert dabei bcc- im Verhältnis zu hcp- und fcc-Strukturen, was folglich zu einem größeren bcc-Anteil im Kristall führt.

[5] hexagonal close-packed
[6] body-centered cubic
[7] face-centered cubic

Abstract

This thesis is dedicated to the nonequilibrium dynamics of colloidal systems. Colloids consist of particles or droplets dispersed in a continuous medium. They belong to the class of mesoscopic systems at typical length scales ranging from a few nanometers to several micrometers. In addition to colloids, such systems span proteins, molecular motors, up to living organisms such as bacteria [1]. The mesoscopic regime is mainly characterized by two important properties. First, the small length scale typically entails an accordingly small energy scale in the order of the thermal energy. Hence, thermal fluctuations play a prominent role. Second, mesoscopic systems, especially biological ones, occur mostly under far-from-equilibrium conditions. For the description of such systems, classical thermodynamics is inadequate, as it does not incorporate fluctuations and involves equilibrium as a prerequisite. *Stochastic thermodynamics* eliminates these problems by extending thermodynamic concepts such as work, heat, and entropy to the level of fluctuating trajectories under fairly general nonequilibrium conditions. The cornerstones of this approach, which has been developed over the past decades, are the first law along fluctuating trajectories [2] and the definition of a stochastic entropy [3]. A central quality of this framework is that it merely requires the coupling to an equilibrated heat bath, while the mesoscopic system itself can be situated arbitrarily far from equilibrium.

The experimental observation and manipulation of mesoscopic systems has become possible mainly due to the development of optical tweezers [4, 5] and atomic force microscopy [6]. Regarding stochastic thermodynamics, colloids play a prominent role in the sense that they provide ideal systems to construct well-controllable setups with few degrees of freedom that can be used to approach fundamental questions and test theoretical predictions [7, 8]. However, the complexity of colloids can easily be increased to complex, interacting many-body systems which may be of interest for technological applications as well [9].

The goal of this thesis is to examine different aspects of the nonequilibrium dynamics in colloidal systems. This task covers fundamental questions such as the measurement of dissipation or the role of hidden degrees of freedom as well as collective phenomena including the quest for an effective nonequilibrium temperature and the formation of colloidal crystals. In order to tackle these points, we employ two different systems. The first of them consists of two interacting colloidal particles driven along two separate rings by optical tweezers. We employ

this experimentally well-controllable system to approach the more fundamental questions of this thesis. The second system is a colloidal suspension belonging to the class of complex interacting many-body systems. We subject this suspension to an external shear flow and use it to study nonequilibrium phenomena arising from the interplay of many particles.

Chapter 2: Brownian dynamics.– In Chapter 2, we briefly review the basic dynamical concepts we will need for the subsequent chapters. These concepts include the Langevin equation, the Fokker-Planck equation, and a path-integral approach for the description of diffusing systems. More detailed and comprehensive presentations are given in several textbooks [10–13].

Chapter 3: Dissipation.– In order to study nonequilibrium, it is sensible to start with nonequilibrium steady states (NESSs). Such states are similar to equilibrium in the sense that their properties do not change with time. The essential difference distinguishing a system in a NESS from an equilibrium system is the constant dissipation of heat. Therefore, the measurement of the dissipation rate is an important aspect in the characterization of NESSs. In macroscopic systems, the dissipated heat can be obtained from calorimetric methods, whereas in a mesoscopic system this route is not accessible due to the small size of the dissipation rates. So far, the only way to measure dissipation at this scale requires both the measurement of correlation functions and the linear response of the system to an external perturbation [14]. However, determining the latter in colloidal systems is mostly difficult and time-consuming. Yet, precise information about the trajectories of colloidal particles is often readily available. In Chapter 3, we present a method extracting the average dissipation rate exclusively from particle trajectories [15]. Hence, there is no need to perturb the system in any way. We test the validity of this method using an overdamped Langevin dynamics simulation of the colloidal two particle system described above and apply the method to experimental data.[8] Moreover, we show how hydrodynamic interactions can be incorporated in this scheme without requiring further data.

Chapter 4: Hidden degrees of freedom.– The description of mesoscopic systems involves in general some sort of coarse graining, for instance, in the Langevin equation [10], which treats the solvent particles in the diffusion of a colloidal particle as an effectively white noise. In general, an effective treatment of hidden degrees of freedom is justified if there is a clear-cut time-scale separation in the dynamics of observed and hidden degrees of freedom. Otherwise, inconsistencies

[8] All experimental data in this thesis were provided by J. Mehl.

and ambiguities may arise. In Chapter 4, we investigate this issue for the entropy production in a NESS [16]. Specifically, we consider the two-particle system described above and focus on the fluctuation theorem (FT) [3], a deep symmetry relation for the probability density of entropy fluctuations. In the evaluation of the entropy production, we include only one particle, pretending not to know about the presence of the other. Hence, we observe an *apparent* entropy production, for which the requirements of the FT are not met. Surprisingly, we still observe an approximate FT-like symmetry even for the apparent entropy production. We discuss why this result is typical both for small and large entropy productions, while deviations are expected for intermediate values. By fine-tuning the parameters, we expose these deviations. Moreover, we show that, for the entropy production in the limit of very short time intervals, an exact FT is obeyed even in the presence of hidden degrees of freedom.

Chapter 5: Effective temperature and the fluctuation-dissipation ratio.– In thermal equilibrium, temperature is closely related to the fluctuation-dissipation theorem (FDT) and can be measured via the so-called fluctuation-dissipation ratio (FDR). The FDT connects equilibrium fluctuations to the linear response of a system to an external perturbation and the FDR defines the ratio of corresponding correlation and response functions. Beyond the linear response regime around equilibrium the FDT breaks down. Likewise does a well-defined temperature concept cease to exist. Yet, around a NESS, we can still define a linear response regime and measure correlation functions. Hence, the FDR can be observed as well. It is tempting to define an effective nonequilibrium temperature via such an FDR [17]. However, it has recently been shown that a generalization of the FDT in a NESS involves an additive excess term causing a time-dependent FDR [18–23]. Consequently, the FDR does not qualify as an effective nonequilibrium temperature. Yet, in glassy and supercooled suspensions FDRs have been observed to become time-independent in the long-time limit [24, 25].

In Chapter 5, we track the motion of a tagged particle in a sheared colloidal suspension. Specifically, we focus on the velocity autocorrelation function and the linear response of the particle to a small force. For moderate densities, we find an approximately time-independent FDR [26]. In contrast to the time-independent FDR in glassy and supercooled systems, we do not observe this behavior in the long-time limit but for the initial relaxation of the response and correlation functions. Moreover, we study a simple model system consisting of a single colloidal particle in a harmonic trap subject to linear shear flow. For this system, we observe an approximately time-independent FDR as well if the trap strength is sufficiently large. In order to gain more insight into the origin of these results, we derive the FDT in a hybrid form containing both additive and multiplicative contributions.

For both systems, a confinement of the motion of the particles leads to a shrinking additive contribution and thus to a more and more time-independent FDR. Moreover, we investigate the Einstein relation connecting the mobility and diffusivity of, e. g., a colloidal particle in thermal equilibrium. We employ the approximately time-independent FDR to define an effective Einstein relation [27]. We check this relation for the simulation data and find a good agreement

Chapter 6: Shear-induced crystallization.– In the last chapter, we abandon the stationarity condition and focus on the time evolution of a system out of a metastable state. Specifically, we investigate the crystallization of a supersaturated colloidal suspension subject to shear flow. Previous reports on the effect of shearing on the crystallization process are not conclusive. On the one hand, the facilitation of crystallization has been reported [28–34]. Others have observed a shear-induced inhibition of the solidification process [35–37]. Also optimal strain rates for which the crystallization proceeds fastest have been found [38–43].

In order to investigate the influence of a linear shear flow on the crystallization process in a supersaturated charge-stabilized suspension in three dimensions, we perform Langevin dynamics simulations [44]. We observe the fastest crystallization for a finite strain rate, supporting the conjecture of an optimal strain rate. We explain this behavior as a result of two counteracting shear-induced effects which become important at different stages during the evolution of the crystallization process. At the nucleation stage, shear flow inhibits the formation of crystalline clusters, whereas at the growth stage the shear flow accelerates the development of the crystal.

In order to analyze the underlying mechanisms, we employ a discrete state model. The state space comprises five states to which we assign single particles according to their structural environment. We distinguish liquid, pre-structured, and the three crystalline structures, hcp (hexagonal close-packed), bcc (body-centered cubic), and fcc (face-centered cubic). A discussion of the transition rates shows that the inhibition of nucleation under shear flow is caused by the shear-induced destruction of a pre-structuring in the liquid, while the shearing forces are too weak to cause significant damage to existing crystalline clusters. Regarding the shear-enhanced crystalline growth, we are able to extract the functional dependence of the growth rate on the strain rate from the data. Using a simple model, we connect this functional form to shear-induced convection. Furthermore, we discuss the influence of the shearing on the composition of crystalline clusters and find that the shear flow stabilizes bcc in relation to hcp and fcc and thus allows for larger bcc domains in the crystal.

1. Introduction

Thermodynamics describes how macroscopic systems consisting of a vast number of interacting constituents exchange work and heat with their environment. This knowledge has been exploited in various applications, most prominently in the construction of heat engines. The Stirling motor, for instance, employs a cyclic sequence of isochoric and isothermal processes to convert heat into mechanical work. The construction of such an engine at the mesoscale, i. e., at typical length scales in the order of tens of nanometers up to a few micrometers, and thus in the regime of colloids, biomolecules, viruses, and bacteria [45], could provide interesting prospects for future applications. Recently, Blickle and Bechinger did indeed succeed in the construction of an analog of the Stirling engine at the scale of a few micrometers [46], see Fig. 1.1. In their engine, the role of the working gas is played by a single colloidal particle, while cylinder and piston are replaced by a harmonic potential created by optical tweezers [4, 5]. The mesoscopic equivalent of the isothermal compression and expansion steps is realized by changing the stiffness of the harmonic potential and thus the volume accessible to the particle. Beside the compression and expansion of the working gas, the Stirling process involves isochoric heating and cooling. These steps require an alternating coupling to a hot and a cold heat bath, which is realized through an almost instantaneous temperature change in the solvent surrounding the colloidal particle generated by a second laser.

The most important difference between a macroscopic and a mesoscopic engine is the role of thermal fluctuations. For a macroscopic system, the characteristic energy scale is much larger than the thermal energy and fluctuations are irrelevant. At the mesoscale, however, typical energies reach the order of the thermal energy and fluctuations play a prominent role [1]. Consequently, the sharp value for the extracted work per cycle in a macroscopic Stirling engine turns into a stochastically fluctuating quantity which is different for every cycle in the case of a mesoscopic engine. Yet, these fluctuating values for the extracted work still follow a systematic distribution, and one can still make exact statements, e. g., about the average work extracted over many repetitions. Moreover, in the limit of very slow cycles, the mesoscopic engine approaches an efficiency which corresponds to the one of a macroscopic Stirling engine [46, 47].

This colloidal system constitutes an impressive example of how fundamental issues can be tackled at the mesoscopic scale. Colloids, in general, have proved very

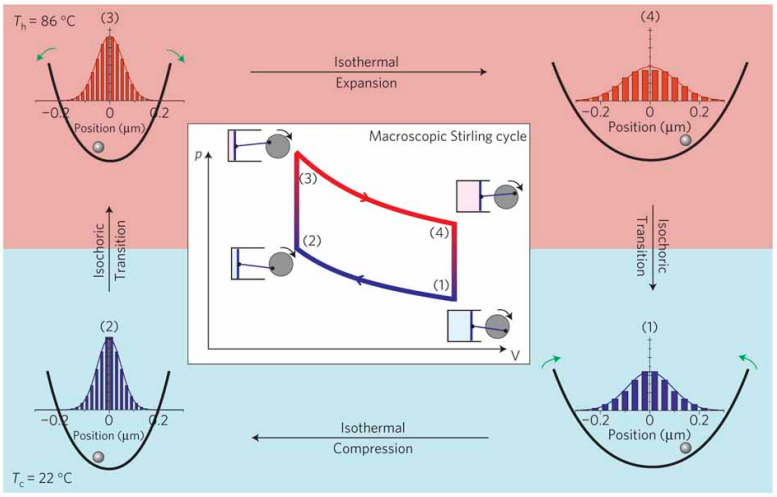

Figure 1.1.: Sketch of the macroscopic (inset) and mesoscopic Stirling motor. The inset schematically shows the four steps of the Stirling process in the pressure-volume diagram. For the colloidal system, the isothermal compression and expansion steps, (1) → (2) and (3) → (4), are realized respectively by increasing and decreasing the stiffness of the trap potential at fixed temperatures. In the isochoric steps, (2) → (3) and (4) → (1), the potential stiffness is kept fixed and the temperature of the environment of the colloidal particle is changed by an additional laser field. Figure from Ref. [46].

valuable for the investigation of mesoscopic dynamics, primarily because of two properties. First, trajectories of colloidal particles can be recorded and manipulated very accurately, which is mainly due to the development of optical tweezers [4,5] and atomic force microscopy [6]. Second, these systems provide a rich variety of interaction types such as steric, electrostatic, and hydrodynamic [9,48,49], as well as magnetic forces [16]. In some cases, these interactions can even be tuned [16,50]. Another merit of colloidal systems is that their complexity can be varied from single particle systems, valuable especially to approach fundamental questions and to test theoretical predictions [7,8], up to interacting many-body systems such as suspensions, which may even be of interest for various technological applications [9].

In this thesis, we focus on two different colloidal systems. The first system consists of two colloidal particles driven along two separate rings by optical tweezers, see Fig. 1.2(a). The particles interact via a repulsive potential whose strength can be controlled externally. We employ this experimentally well-controllable system to address rather fundamental questions such as the measurement of heat dissipation [15] and the role of hidden degrees of freedom [16]. The second system, see Fig. 1.2(b), is a colloidal suspension comprising a large number of interacting degrees of freedom belonging to the class of complex many-body systems. Using this system, we will approach issues arising from collective phenomena such as the quest for an effective nonequilibrium temperature [26] and crystallization under shear flow. **In Chapter 2**, we will review the fundamental dynamical concepts necessary to describe these systems.

First law and dissipation

For the theoretical description of mesoscopic systems, classical thermodynamics is inadequate since fluctuations are not incorporated. Moreover, mesoscopic systems frequently occur under nonequilibrium conditions [45]. For thermodynamics, however, equilibrium is a prerequisite. A more promising approach requires a framework generalizing the thermodynamic concepts to fluctuating systems under fairly general nonequilibrium conditions. Such a framework, now termed *stochastic thermodynamics* [52–54], has been developed in the past two decades. In 1997, Sekimoto provided the starting point by establishing an energy balance which can be regarded as the first law on the level a fluctuating trajectory of, e. g., a colloidal particle diffusing through water. The solvent, which typically surrounds mesoscopic systems, serves as a heat bath and is assumed to rest in thermal equilibrium with a well-defined temperature T at all times. A central quality of this framework is that thermal equilibrium is only required for the heat bath, while the mesoscopic system can be driven out of equilibrium arbitrarily far.

In order to study nonequilibrium, it is convenient to start with stationary states.

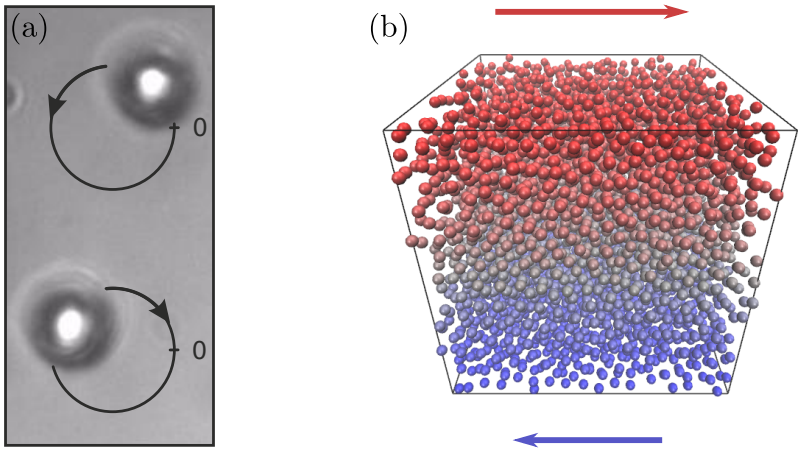

Figure 1.2.: (a) Snapshot of the experimental system from Ref. [51]. Two interacting colloidal particles are driven along two separate rings (see black circles) by optical tweezers. (b) Snapshot of a Langevin dynamics simulation of a sheared suspension containing 4860 interacting colloidal particles. The color gradient indicates the velocity of the surrounding solvent.

These *nonequilibrium steady states* (NESSs) occur in various contexts. They can be found in molecular motors [55–57], in colloidal suspensions subject to a steady shear flow [27], as well as in strongly-correlated dissipative electron systems [58], and even in traffic jams on public roads [59]. NESSs are similar to equilibrium in the sense that observables have time-independent expectation values. However, there is an essential difference distinguishing them from equilibrium: while in equilibrium there is no net transfer of heat to the environment, a NESS is characterized by stationary currents which constantly dissipate energy into the heat bath.

In macroscopic systems, the dissipated heat can be inferred indirectly from the knowledge of the work applied to a system or directly through the measurement of temperature changes. By contrast, measuring dissipation at the mesoscale is rather difficult as calorimetric methods fail because of the small magnitude of the dissipation rates. In principle, the first law of stochastic thermodynamics allows for the measurement of heat dissipation if both the external driving and the internal energy change in the system can be measured. However, in practice, this information is generally not accessible. Knowing, for instance, the external force applied to a colloidal particle by a laser field beyond the paradigmatic harmonic trap [7] is rather challenging [8,60]. Likewise, measuring directly the amount of the *adenosine triphosphate* (ATP) hydrolyzed by a single molecular motor is impossible [61]. The first, and so far only, viable method for measuring heat dissipation in mesoscopic systems extracts the dissipation rate from the fluctuations and the linear response of the system to external perturbations [14].

In Chapter 3, we develop a method to determine the dissipation rate exclusively from the knowledge of trajectories in configuration space, which is readily available for colloidal systems [62]. We test this method in a Langevin dynamics simulation for an experimentally accessible colloidal system and apply the procedure to experimental data [15]. Moreover, we show how hydrodynamic interactions can be incorporated in the procedure and discuss the entailing consequences for heat dissipation.

Stochastic entropy and the role of hidden degrees of freedom

Endowed with the first law on the level of fluctuating trajectories, the next step is to ask for an analogous extension of entropy. The answer was given by Seifert in the definition of a *stochastic entropy* along fluctuating trajectories [3], thus completing the fundament of stochastic thermodynamics [52–54]. On the level of fluctuating trajectories, the stochastic entropy produced by the mesoscopic system also becomes a fluctuating quantity. However, the distribution of these fluctuations is not entirely arbitrary but obeys a deep symmetry relation which for NESSs can be cast into the transparent form [3]

$$\ln\left[\frac{p(\Delta s_{\mathrm{tot}})}{p(-\Delta s_{\mathrm{tot}})}\right] = \Delta s_{\mathrm{tot}}, \tag{1.1}$$

where we set the Boltzmann constant to unity throughout this thesis. This *fluctuation theorem* (FT) for the total entropy production Δs_{tot} in the mesoscopic system and the heat bath quantifies the relative frequencies of positive and negative entropy fluctuations in a finite time interval. Here, $p(\Delta s_{\mathrm{tot}})$ denotes the probability density for finding the total entropy production Δs_{tot} in an arbitrary but fixed time interval. Eq. (1.1) is one representative of a large class of FTs, the first of which has been found by Evans et al. in a numerical simulation of a two-dimensional, sheared colloidal suspension [63]. For deterministic dynamics, a rigorous proof resting on the *chaotic hypothesis*, time-reversibility, and a phase-space contraction associated with dissipation was given by Gallavotti and Cohen [64]. In stochastic dynamics, FTs can be proved for Markovian systems [3, 65, 66]. For mesoscopic systems, the Markovian property rests on a time-scale separation between the dynamics of fast and slow degrees of freedom. Interactions with fast degrees of freedom, such as the coordinates of solvent molecules, lead to an effectively white noise and thus to a Markovian dynamics for the slow degrees of freedom, such as the positions of colloidal particles. For this type of dynamics, the FT has been confirmed experimentally for colloidal systems [7,67] and a harmonic oscillator coupled to a thermal bath [68]. FTs can also be formulated for time-dependent driving. Among them, the Jarzynski [69] and the closely related Crooks relation [70] had the largest impact, not least because of their practical importance. Most prominently, Hummer

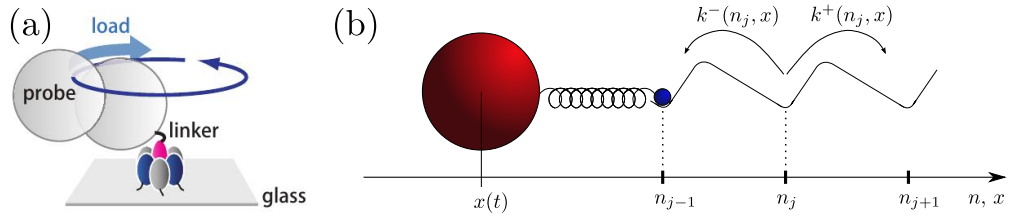

Figure 1.3.: (a) Polystyrene particle dimer coupled via a linker protein (streptavidin) to the γ-shaft (pink) of the F_1-ATPase. The $\alpha_3\beta_3$-ring (blue and dark gray) is fixed on a glass surface. Picture from Ref. [61]. (b) Schematic sketch of the shaft of the motor protein (blue) at state n coupled via a linker to a probe particle (red) at the continuous position x. The motor jumps to neighboring sites with the state-dependent rates $k^{\pm}$. Figure from Ref. [79] (changed).

and Szabo [71] showed that the Jarzynski relation can be used to determine the free-energy profiles in biomolecules [72–74], see Ref. [75] for a review.

Recently, Hayashi et al. [76] used a variant of the FT given in Eq. (1.1) to determine the rotary torque exerted by the motor protein F_1-ATPase during ATP hydrolysis. As the rotor is too small to be seen under an optical microscope ($\simeq$ 10 nm), it must be observed indirectly through a much larger probe (358 – 940 nm) coupled to the motor by a linker protein [76–78], cf. Fig. 1.3. In solving the microscopy issue, this coupling introduces a different problem. One observes merely one out of two coupled degrees of freedom [79]. This situation is fundamentally different from describing fast degrees of freedom only implicitly through white noise, since there is no clear-cut time-scale separation between the dynamics of the probe and that of the motor. Hence, the conditions for the derivation of the FT are not met and inconsistencies may arise if the FT is still applied.

In Chapter 4, we use the experimental system shown in Fig. 1.2(a) to approach this problem [16]. Specifically, we determine the probability distribution for an *apparent* total entropy production caused by only one particle, while ignoring the presence of the other. Hence, the ignored particle constitutes a *hidden slow* degree of freedom with an influence of tunable strength. For this apparent total entropy production, there is no such relation as the FT. Surprisingly, we find that the functional form of Eq. (1.1) is preserved up to a constant factor. We show that this behavior is merely approximate and give explanations for its origin. Moreover, we show that, considering the entropy production in short time-intervals, the exact form of the FT is approached even if hidden degrees of freedom are present.

Linear response and effective temperatures

In the linear response regime around equilibrium, the fluctuation theorem implies the *fluctuation-dissipation theorem* (FDT) [80]. This remarkable relation connects equilibrium fluctuations to the linear response of an arbitrary observable to small perturbations [81]. The virtue of this connection is twofold. On the one hand, we gain information about the linear response regime around equilibrium simply by observing equilibrium fluctuations, i. e., without actually leaving the equilibrium state. On the other hand, macroscopic response coefficients, such as the magnetic susceptibility, yield insight into microscopic fluctuations.

The first form of the FDT has been derived in 1905 by Einstein for a Brownian particle diffusing through a solvent [82]. In 1928, Nyquist discovered another form relating thermal fluctuations to the electromotive force in an electrical circuit [83], before Onsager formulated the FDT in full generality in 1931 [84, 85]. A rigorous proof was provided by Callen and Welton in 1951 [86].

An important property of the FDT is that it is the temperature T which links the response to fluctuations. More precisely, the ratio between corresponding time-dependent correlation and response functions, the so-called *fluctuation-dissipation ratio* (FDR), is time-independent and yields the same value T for any choice of observable and perturbation. Beyond the linear response regime around equilibrium, the FDT breaks down. Likewise, even in stationary nonequilibrium, there is still no such concept as temperature. Yet, around each stationary state, it is still possible to delineate a linear response regime. It is therefore tempting to define an *effective* temperature by evaluating the equilibrium form of the FDR in NESSs [87–90], see Ref. [17] for a review. However, recent progress both in theory [18–20] and experiment [21–23] has shown that the extension of the FDT to NESSs requires an additive form which is not compatible with a time-independent FDR. Moreover, in general, the FDR will also depend on the choice of observable and perturbation defining the shape of the response and correlation functions [91]. Nevertheless, there are still situations in which these dependencies vanish to a very good degree. In supercooled and glassy systems, for instance, a time-scale separation in the dynamics leads to an approximately constant FDR for long time scales [24, 25].

In Chapter 5, we investigate the FDT for a tagged particle in a sheared colloidal suspension, see Fig. 1.2(b). In this NESS, we observe an approximately constant FDR already at moderate densities deviating significantly from the equilibrium value [26]. Motivated by a simple model system, in which we find a similar behavior, we argue that this effect stems from an effective confinement [26] caused by the neighboring particles. Moreover, we investigate the implications on the Einstein relation connecting the mobility and diffusivity of the tagged particle [27].

Colloidal crystallization in shear flow

Increasing the density of such a colloidal suspension, the disordered configurations will at some point become unstable and turn into a solid with long-range order. Also for simple hard-sphere systems, a larger density leads to crystallization or even to glassy states [49, 92]. The solidification of such a hard-sphere fluid is paradigmatic for a purely entropic phase transition, since there is no difference in the internal energies of the solid and the liquid [92].

Typically, a solidification in colloidal suspensions involves a free-energy barrier arising from the energetically expensive liquid-solid interface that must be formed in order to create the energetically favorable solid bulk. In order to overcome this free-energy barrier, a fluctuation must form a crystalline nucleus of a critical size above which further growth decreases the free-energy of the cluster. Avoiding nucleation, the density of a colloidal suspension can be increased even beyond the thermodynamic freezing density without solidification. Such a suspension is then called *supersaturated*. The *classical nucleation theory* (CNT) [93–95] provides a means to obtain simple analytic expressions for the height of this free-energy barrier and the size of the corresponding *critical nucleus*.

Subjecting such a supersaturated suspension to a stationary shear flow drives the system out of equilibrium. Hence, the free energy is no longer well defined, rendering the CNT invalid. Nevertheless, sheared suspensions still crystallize, although with underlying dynamics and mechanisms that might be significantly different from the unsheared case. Previous studies examining the effect of shear flow on crystallization report both the suppression [35–37] and the facilitation [28, 32–34] of crystallization. Others report an optimal strain rate in hard-sphere-like systems [38, 39] and in protein solutions [40]. Optimal strain rates have been observed also in two dimensions for Yukawa-type [41], Ising [42], and depletion-driven attractive [43] systems.

In Chapter 6, we introduce a discrete state model exploiting a time-scale separation between fast transitions between different structures and the overall progress of crystallization. Using this model, we investigate the influence of a weak but steady shear flow on the crystallization rate for a highly supersaturated, charge-stabilized colloidal suspension in three dimensions [44]. Our data supports the conjecture of an optimal strain rate. We explain this result as a consequence of two counteracting, shear-dependent effects which become important at different stages during the crystallization process. At the nucleation stage, the flow field suppresses the development of a loose structure in the liquid thus significantly increasing the time the suspension needs to form a critical nucleus. Once a growing nucleus is formed, the shear flow accelerates the growth process. We extract the functional dependence of the growth rate on the strain rate from our data and explain it through a simple convective mechanism. Moreover, we discuss how the

flow field affects the structural composition of the crystalline clusters and suggest a second mechanism how the flow field might accelerate the crystalline growth.

Publications

Parts of this thesis have been published previously:

- "Mobility and diffusion of a tagged particle in a driven colloidal suspension" B. Lander, U. Seifert, and T. Speck, EPL **92**, 58001 (2010)
- "Effective confinement as origin of the equivalence of kinetic temperature and fluctuation-dissipation ratio in a dense shear-driven suspension" B. Lander, U. Seifert, and T. Speck, Phys. Rev. E **85**, 021103 (2012)
- "Role of hidden slow degrees of freedom in the fluctuation theorem" J. Mehl, B. Lander, C. Bechinger, V. Blickle, and U. Seifert, Phys. Rev. Lett. **108**, 220601 (2012)
- "Noninvasive measurement of dissipation in colloidal systems" B. Lander, J. Mehl, V. Blickle, C. Bechinger, and U. Seifert, Phys. Rev. E **86**, 030401(R) (2012)
- "Crystallization in a sheared colloidal suspension" B. Lander, U. Seifert, and T. Speck, J. Chem. Phys. (accepted)

2. Brownian motion in a nutshell

2.1. Introduction

The size of colloidal particles covers a range from roughly 1 nm to 10μm [96]. Therefore, they belong to the mesoscopic scale and are subject to thermal fluctuations. Tracking the motion of a colloidal particle suspended in water, one will observe that the particle is not at rest but moves erratically through the solvent. This so-called *Brownian motion* was observed in 1785 by Jan Ingenhousz in the irregular motion of coal dust particles on the surface of ethanol, but also by the Scottish botanist Robert Brown in 1828, who reported on the jittery motion of pollen grains in water [97], and after whom it was named. The physical explanation of this type of motion as a result of the vast number of collisions between the observed Brownian particle and the much smaller, unobserved solvent molecules was provided early in the 20th century by Einstein [82] and Smoluchowski [98]. Their work, in combination with the experimental confirmation by Perrin [99], provided for the first time strong evidence for the existence of atoms and molecules.

On one side, an appropriate description of the dynamics of such mesoscopic particles which are coupled to a heat bath requires the incorporation of thermal fluctuations. On the other side, details about the microscopic trajectories of the heat-bath particles are generally neither available nor relevant. In order to appreciate these points, one usually employs coarse-grained descriptions including the correct statistical properties of the thermal fluctuations. In this chapter, we will briefly review three complementary but equivalent approaches described in detail in several textbooks [10–13]. First, we focus on the Langevin equation modeling Brownian motion most intuitively on a trajectory level by including the coupling to the solvent through friction forces and a stochastic noise term. Second, we discuss the Fokker-Planck equation describing the time evolution of the probability density function of stochastic variables. Finally, we briefly elucidate a path-integral approach assigning a weight to every possible path the configuration of the system can take.

2.2. Langevin equation

The Langevin approach models the motion of colloidal particles on a trajectory level, in which collisions of the colloidal particles with the solvent molecules are effectively described by a random force and a friction term. The goal is to obtain an equation that generates trajectories with statistical properties equivalent those of the full microscopic dynamics, however, with a much smaller effort. Such trajectories would then provide a means to make exact statements about averaged quantities such as expectation values and correlation functions. The crucial assumption for this approach is a separation of the time scales on which the momenta of the solvent molecules and those of the much larger colloidal particles equilibrate. For colloidal particles in water, this assumption is satisfied to a very good degree: the momenta of the solvent molecules relax to equilibrium in the order of 10^{-14} s, whereas the equilibration of the colloidal momenta is slower by roughly five orders of magnitude [96].

The Langevin approach implements these ideas by augmenting the Newton equations by an interaction with the solvent at temperature T in terms of friction and stochastic forces. Specifically, the Langevin equations couple the set of position and velocity vectors, $\mathbf{R} \equiv \{\mathbf{r}_i | 1 \leq i \leq N\}$ and $\mathbf{V} \equiv \{\mathbf{v}_i | 1 \leq i \leq N\}$, respectively, of N colloidal particles with masses m_i by $\dot{\mathbf{r}}_i = \mathbf{v}_i$ and

$$m_i \dot{\mathbf{v}}_i = \mathbf{F}_i(\mathbf{R}, \lambda) - \mu_0^{-1}[\mathbf{v}_i - \mathbf{u}(\mathbf{r}_i)] + \boldsymbol{\xi}_i \quad \text{for} \quad i \in \{1, \ldots, N\}, \tag{2.1}$$

where the dot denotes a time derivative. At velocities characteristic for colloidal systems, the friction term is proportional to the difference between the particle velocity and the local solvent velocity $\mathbf{u}(\mathbf{r}_i)$. The Stokes law fixes the inverse mobility, i. e., the friction constant, to $\mu_0^{-1} = 3\pi\eta a$ with the dynamic viscosity of the solvent η and the particle diameter a. The stochastic forces $\boldsymbol{\xi}_i$ are chosen as Gaussian white noise with zero mean $\langle \boldsymbol{\xi}_i \rangle = 0$ and correlations

$$\left\langle \boldsymbol{\xi}_i(t) \boldsymbol{\xi}_j^{\mathrm{T}}(t') \right\rangle = 2\mu_0^{-1} T \delta_{ij} \mathbb{1} \delta(t - t') \tag{2.2}$$

with the transposition operator $\cdot^{\mathrm{T}}$ and where unless stated otherwise the angular brackets $\langle \cdot \rangle$ are interpreted as an ensemble average in a stationary state throughout this thesis. The Dirac distribution $\delta(t)$ accounts for the infinitesimally short correlation time of the stochastic forces, the Kronecker symbol δ_{ij} ensures that those forces acting on different particles are uncorrelated, and $\mathbb{1}$ denotes the identity matrix. The magnitude of the stochastic forces is determined by the temperature T and the mobility μ_0, which are connected to the bare diffusion constant D_0 by the Einstein relation $D_0 = \mu_0 T$. This relation expresses the closely related origin of friction and diffusion and ensures that in thermal equilibrium the dynamics given in Eq. (2.1) leads to the Boltzmann distribution [100, 101]. The forces

$\mathbf{F}_i(\mathbf{R},\lambda) = \mathbf{F}_i^{\mathrm{ext}}(\mathbf{r}_i,\lambda) + \mathbf{F}_i^{\mathrm{int}}(\mathbf{R},\lambda)$ can be tuned by an external control parameter λ and comprise both externally imposed forces $\mathbf{F}_i^{\mathrm{ext}}(\mathbf{r}_i,\lambda)$ and interactions between the colloidal particles

$$\mathbf{F}_i^{\mathrm{int}}(\mathbf{R},\lambda) = -\sum_{j\neq i} \boldsymbol{\nabla}_i u(\mathbf{r}_{ij},\lambda). \tag{2.3}$$

Throughout this thesis, we restrict ourselves to two-body interactions described by pairwise interaction potentials of the form $u(\mathbf{r}_{ij})$ with $\mathbf{r}_{ij} \equiv \mathbf{r}_i - \mathbf{r}_j$ and the gradient operator with respect to the position of the ith particle $\boldsymbol{\nabla}_i$.

Overdamped limit

So far, we have already used a time scale separation between the motion of the solvent and that of the colloidal particles. Yet, in the description of the colloidal dynamics, there is another time scale separation left to exploit. In such systems, inertial effects are typically much smaller than their frictional counterparts. More specifically, the momenta of the colloidal particles relax on a time scale $\tau_{\mathrm{m}} \equiv \mu_0 m \sim 10^{-9}$ s, while experimental observation times are typically in the order of the diffusive time scale $\tau_{\mathrm{D}} \equiv a^2/D_0 \sim 10^{-3}$ s [96]. In most situations, we can therefore neglect inertial contributions and describe colloidal dynamics in the so-called overdamped limit using only particle positions.

In order to expose the relevance of this time-scale separation in the Langevin equation (2.1), we switch to dimensionless quantities marked by asterisks. Specifically, we measure lengths in units of the particle diameter a, energies in units of the thermal energy T, and time in units of the diffusive time scale τ_{D}. Multiplying Eq. (2.1) with $\mu_0\tau_{\mathrm{D}}/a$, we obtain

$$\frac{\mu_0 m_i}{\tau_{\mathrm{D}}}\dot{\mathbf{v}}_i^* = \mathbf{F}_i^*(\mathbf{R},\lambda) - [\mathbf{v}_i^* - \mathbf{u}^*(\mathbf{r}_i)] + \boldsymbol{\xi}_i^*. \tag{2.4}$$

We can now exploit $\mu_0 m_i \equiv \tau_{\mathrm{m}} \ll \tau_{\mathrm{D}}$. Switching back to dimensionful quantities and replacing the velocity by $\mathbf{v} = \dot{\mathbf{r}}$, we obtain the overdamped Langevin equation

$$\dot{\mathbf{r}}_i = \mu_0 \mathbf{F}_i(\mathbf{R},\lambda) + \mathbf{u}(\mathbf{r}_i) + \boldsymbol{\zeta}_i, \tag{2.5}$$

where we use the stochastic velocities $\boldsymbol{\zeta}_i \equiv \mu_0 \boldsymbol{\xi}_i$ with $\langle \boldsymbol{\zeta}_i \rangle = 0$ and

$$\left\langle \boldsymbol{\zeta}_i(t)\boldsymbol{\zeta}_j^{\mathrm{T}}(t') \right\rangle = 2D_0\delta_{ij}\mathbb{1}\delta(t-t'). \tag{2.6}$$

Hydrodynamic interaction

A colloidal particle moving through a solvent drags the surrounding liquid along. The resulting flow field influences the trajectories of other nearby colloidal particles and vice versa. So far, we have neglected such hydrodynamic interactions between the colloidal particles. Yet, depending on the specific system, they can play a significant role.

Flow fields can be characterized by the Reynolds number [96]

$$\mathrm{Re} = \frac{\rho_{\mathrm{fl}} v a}{\eta}, \tag{2.7}$$

which quantifies the relative importance of inertial and viscous effects. It relates the typical velocity v of objects of typical size a moving through a fluid of density ρ_{fl} to the fluid viscosity η. For colloidal particles, typical Reynolds numbers are small. For instance, a colloidal particle with a diameter of 1 µm moving with a velocity of 1 µm/s through water at room temperature, we obtain $\mathrm{Re} \sim 10^{-6}$. Hence, inertial effects can be neglected. In addition, we assume that the flow field caused by the motion of a particle spreads instantaneously, which is well justified on the diffusive time scale [96]. The flow fields resulting from the motion of colloidal particles are thus classified as creeping flow and can be described by the Stokes equation.

The Stokes equation is linear and independent of time. Thus, there is a linear relation between the hydrodynamic flow field and the forces acting on the particles. The total hydrodynamically induced flow field at the position of the ith particle is given by

$$\mathbf{u}^{\mathrm{hyd}}(\mathbf{r}_i) = \sum_{j=1}^{N} \boldsymbol{\mu}_{ij}(\mathbf{R}) \mathbf{F}_j(\mathbf{R}, \lambda) \tag{2.8}$$

where $\boldsymbol{\mu}_{ij}(\mathbf{R})$ are the mobility matrices coupling the motion of the ith and the jth particle. The mobility matrices depend on all instantaneous particle coordinates $\mathbf{R}$ and are computed for a hydrodynamically interacting pair of spheres in Appendix A. In the dilute limit the mobility matrices reduce to

$$\boldsymbol{\mu}_{ij}(\mathbf{R}) \to \mu_0 \mathbb{1} \delta_{ij} \tag{2.9}$$

reproducing the Stokes friction for isolated spheres.

Including the hydrodynamic contribution in the overdamped Langevin equation, we obtain

$$\dot{\mathbf{r}}_i = \sum_{j=1}^{N} \boldsymbol{\mu}_{ij}(\mathbf{R}) \mathbf{F}_j(\mathbf{R}, \lambda) + \mathbf{u}(\mathbf{r}_i) + \mathbf{d}_i^{(\alpha)}(\mathbf{R}) + \boldsymbol{\zeta}_i \tag{2.10}$$

where $\langle \boldsymbol{\zeta} \rangle = 0$ and $\left\langle \boldsymbol{\zeta}_i(t)\boldsymbol{\zeta}_j(t') \right\rangle = 2\,\mathsf{D}_{ij}(\mathbf{R})\delta(t-t')$ with the Einstein relation $\mathsf{D}_{ij}(\mathbf{R}) = T\mu_{ij}(\mathbf{R})$. The so-called spurious drift $\mathbf{d}^{(\alpha)}$ is caused by the space-dependent diffusion coefficient varying the magnitude of the stochastic velocities multiplicatively [102], see Appendix B. For the treatment of stochastic differential equations with *multiplicative noise*, it is crucial to specify the configuration $\mathbf{R}^{(\alpha)} \equiv (1-\alpha)\mathbf{R}(t)+\alpha\mathbf{R}(t+\Delta t)$ for $\alpha \in [0,1]$ during a time step Δt for which we determine the magnitude of the stochastic velocities [10–12]. As different choices for α lead to different solutions, we need to include the spurious drift [102],

$$\mathbf{d}_i^{(\alpha)}(\mathbf{R}) = (1-2\alpha)\sum_{j=1}^{N} \boldsymbol{\nabla}_j \cdot \mathsf{D}_{ji}(\mathbf{R}) + \alpha \sum_{j,k=1}^{N} [\boldsymbol{\nabla}_k \cdot \mathsf{G}_{kj}(\mathbf{R})]\mathsf{G}_{ji}(\mathbf{R}), \tag{2.11}$$

to ensure that the stationary distribution converges to the Boltzmann distribution in thermal equilibrium. Here, the symmetric matrices $\mathsf{G}_{ij}(\mathbf{R})$ are defined by their connection to the diffusion coefficient $\mathsf{D}_{ij}(\mathbf{R}) \equiv \sum_{k=1}^{N} \mathsf{G}_{ik}(\mathbf{R})\mathsf{G}_{kj}(\mathbf{R})$.

2.3. Fokker-Planck equation

In the Langevin description, we model Brownian motion on a trajectory level. Precise predictions, however, can only be made for expectation values. The complete information about ensemble averages of an observable $A(x)$ is also contained in the time-dependent probability density function (pdf) $\Psi(x,t)$ for a stochastic variable x. In this sense, the description of the time evolution of the pdf constitutes a complementary but equivalent approach to model Brownian motion.

The time-evolution of $\Psi(x,t)$ is described by the Fokker-Planck equation

$$\partial_t \Psi(x,t) + \partial_x j(x,t) = 0, \tag{2.12}$$

here, written in the form of a continuity equation ensuring the conservation of probability, where we denote the partial derivative respect to x as ∂_x. The Kramers-Moyal expansion, which is detailed in several textbooks, see, e. g., Refs. [10–12], yields the probability current

$$j(x,t) = \sum_{n=1}^{\infty} (-\partial_x)^{n-1}\, D^{(n)}(x,t)\Psi(x,t) \tag{2.13}$$

with the Kramers-Moyal coefficients

$$D^{(n)}(x,t) \equiv \partial_\tau \left\langle [x(t+\tau)-x(t)]^n \right\rangle |_{\tau=0}/n!, \tag{2.14}$$

where ! denotes the factorial operator. For systems with a diffusive contribution to the dynamics, the displacement $x(t+\tau) - x(t)$ is statistically of the order $\tau^{1/2}$ [11]. Hence, all Kramers-Moyal coefficients vanish for $n \geq 3$ and the current contains only the first two summands. These coefficients can be obtained from the Langevin Equation and therefore connect the Fokker-Planck equation to the Langevin dynamics discussed above.

This approach can be easily generalized to arbitrary many degrees of freedom [10–12]. With the dynamics given, e. g., in Eq. (2.10), we can compute the Kramers-Moyal coefficients and obtain the Fokker-Planck equation

$$\partial_t \Psi(\mathbf{R}, t) = -\sum_{i=1}^{N} \boldsymbol{\nabla}_{\mathbf{r}_i} \cdot \mathbf{j}_i(\mathbf{R}, t) \tag{2.15}$$

with the corresponding probability currents

$$\mathbf{j}_i(\mathbf{R}, t) \equiv \sum_{j=1}^{N} \left[\mu_{ij}(\mathbf{R})\mathbf{F}_j(\mathbf{R}, \lambda) + \mathbf{u}(\mathbf{r}_i) - \mathsf{D}_{ij}(\mathbf{R})\boldsymbol{\nabla}_j\right] \Psi(\mathbf{R}, t). \tag{2.16}$$

It is instructive to consider the mean local velocity [18]

$$\boldsymbol{\nu}_i(\mathbf{R}, t) \equiv \langle \dot{\mathbf{r}}_i | \mathbf{R}, t \rangle \equiv \lim_{\Delta t \to 0} \langle \mathbf{r}_i(t + \Delta t) - \mathbf{r}_i(t - \Delta t) | \mathbf{R} \rangle / (2\Delta t) \tag{2.17}$$

defined as the locally averaged velocity of all trajectories passing through a configuration $\mathbf{R}$, see Fig. 2.1. Note that the derivative is evaluated in mid-step position, corresponding to the Stratonovich convention. The conditional average on the right-hand side can be evaluated by employing a path integral approach [54],

$$\boldsymbol{\nu}_i(\mathbf{R}, t) = \mathbf{j}_i(\mathbf{R}, t)/\Psi(\mathbf{R}, t) = \sum_{j=1}^{N} \left[\mu_{ij}(\mathbf{R})\mathbf{F}_j(\mathbf{R}, \lambda) + \mathbf{u}(\mathbf{r}_i)\right] - \mathsf{D}_{ij}(\mathbf{R})\boldsymbol{\nabla}_j \ln \Psi(\mathbf{R}, t), \tag{2.18}$$

where the last equality holds for the dynamics defined in Eq. (2.10). In the following, this notion will prove useful, especially for the physical interpretation of systems in NESSs.

2.4. Path integral formalism

Up to now, we have introduced two complementary but equivalent ways to treat stochastic dynamics theoretically: the Langevin and the Fokker-Planck representation. While the former provides a means to generate typical trajectories from which

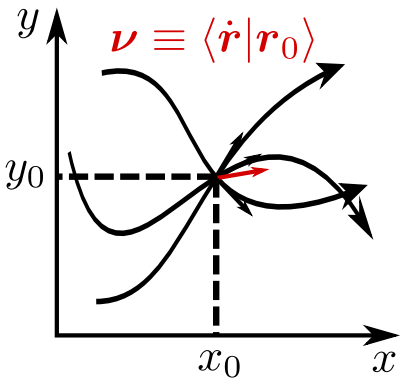

Figure 2.1: Mean local velocity ν for a single particle determined from averaging the particle velocity for an ensemble of trajectories passing through a fixed position $\mathbf{r}_0$.

averaged quantities can be computed, the latter describes the evolution of pdfs for the configuration of the system. Yet another equivalent description [53, 103] is based on the idea that the value of any observable $A[\mathcal{X}]$ can be determined from the knowledge about the path $\mathcal{X} \equiv \{x(\tau)|\tau \in \mathcal{I}\}$ the degrees of freedom in the system take in a time interval $\mathcal{I}$. The square brackets denote a functional dependence on the argument. If we are only interested in ensemble averages, it is sufficient to know the normalized weight $P[\mathcal{X}]$ of every path $\mathcal{X}$ to be able to compute any expectation value,

$$\langle A(t) \rangle = \int A[\mathcal{X}] P[\mathcal{X}] \mathrm{d}\mathcal{X}, \tag{2.19}$$

with the path-independent functional measure $\mathrm{d}\mathcal{X}$ determined by the normalization condition

$$\int P[\mathcal{X}] \mathrm{d}\mathcal{X} = 1. \tag{2.20}$$

For one-dimensional overdamped Langevin dynamics, the only nondeterministic variable is the stochastic velocity ζ modeled as Gaussian white noise, see Eq. (2.6). The path weight leading to the same statistical properties is

$$P[\mathcal{Z}] \equiv \exp\left\{ \frac{1}{4D_0} \int_{\mathcal{I}} \zeta(\tau)^2 \mathrm{d}\tau \right\}, \tag{2.21}$$

with $\mathcal{Z} \equiv \{\zeta(\tau)|\tau \in \mathcal{I}\}$. Given some starting point x_0, we can obtain the weight for the evolution of a trajectory in a time interval $\mathcal{I}$ by a change of variables. We substitute $\zeta(\tau)$ with $\dot{x}(\tau) - \mu_0 F(x(\tau))$ and obtain the conditional path weight

$$P[\mathcal{X}|x_0] = \mathcal{N} \exp\{-\mathcal{A}[\mathcal{X}|x_0]\}, \tag{2.22}$$

with the normalization constant $\mathcal{N}$, the action functional

$$\mathcal{A}[\mathcal{X}|x_0] \equiv \frac{1}{4D_0} \int_{\mathcal{I}} \left[\dot{x}(\tau) - \mu_0 F(x(\tau))\right]^2 \mathrm{d}\tau + \mathcal{J}[\mathcal{X}|x_0], \tag{2.23}$$

and the Jacobian [53]

$$\mathcal{J}[\mathcal{X}|x_0] \equiv \frac{\mu_0}{2} \int_{\mathcal{I}} \partial_x F(x)|_{x=x(\tau)} \mathrm{d}\tau. \tag{2.24}$$

The analytical or numerical computation of such path integrals is quite challenging in many cases. Therefore, in practice, the two formalisms presented in the preceding sections are employed more frequently. Nevertheless, this approach can yield valuable insights, e. g., if we are interested in symmetry properties with respect to time reversal, see Chapter 4.

3. Heat dissipation along trajectories

3.1. Introduction

The fundamental difference between nonequilibrium and equilibrium systems is dissipation. Every NESS contains stationary currents which are connected with a steady dissipation of heat. Measuring the corresponding dissipation rates is therefore a central point in the characterization of these states. However, in mesoscopic systems such a measurement is a nontrivial task. Calorimetric methods usually employed for macroscopic systems fail due to the tiny values of heat generated. So far, the only available method, introduced by Harada and Sasa in 2005 [104], infers dissipation from measuring response and correlation functions. In many colloidal systems, however, response functions are difficult to obtain. By contrast, details about steady-state trajectories are easily accessible. In this chapter, we will introduce a simple averaging procedure which can be used to exploit this data in order to reliably obtain the average heat production rate. We will test this method using a Langevin dynamics simulation and apply it to experimental data of an interacting driven colloidal system [15]. Moreover, we will show how hydrodynamic interactions between the colloidal particles can be incorporated in this scheme and discuss its effect on the average heat production rate in the same experiment.

3.2. First law along fluctuating trajectories

Before discussing the measurement of heat dissipation in colloidal systems, we need to review the extension of the first law of thermodynamics to the mesoscopic scale. Of course, energy must be conserved also along a fluctuating trajectory, e. g., for a colloidal particle moving erratically through an aqueous solvent. Starting from this idea, Sekimoto established an energy balance in which he identified work and heat. Putting it differently, he transferred the notion of the first law to the level of fluctuating trajectories [2, 101]. Blickle et al. demonstrated the validity of this concept experimentally for an overdamped colloidal particle in a time-dependent anharmonic potential in 2006 [8].

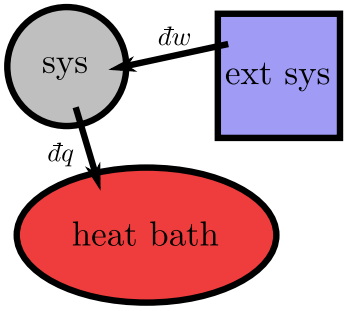

Figure 3.1: The mesoscopic system (sys) is coupled to an external system (ext sys) which performs work on ($đw > 0$) or extracts work from ($đw < 0$) the system. In addition, the system can dissipate heat into ($đq > 0$) and absorb heat from ($đq < 0$) a coupled heat bath.

Along the lines of Refs. [52, 54, 101], we recapitulate the essential steps leading to the first law along fluctuating trajectories. In particular, we discuss the matter paradigmatically for a system consisting of a single colloidal particle coupled to both a heat bath at temperature T and an external system serving as a work reservoir, see Fig. 3.1. The dynamics of the system is described by an overdamped Langevin equation in the form of Eqs. (2.5) and (2.6),

$$\dot{x} = -\mu_0 F(x, \lambda) + \zeta. \tag{3.1}$$

The externally applied force

$$F(x, \lambda) = -\partial_x U(x, \lambda) + f(x, \lambda) \tag{3.2}$$

can be decomposed into the gradient of the potential $U(x, \lambda)$ and a nonconservative force $f(x, \lambda)$.[1]

Energy conservation along a fluctuating trajectory implies that the work

$$đw = \mathrm{d}U + đq \tag{3.3}$$

performed by the external system is either dissipated as heat $đq$ or used to increase the potential energy U of the system, where we use the convention that both work injected into the system and heat dissipated into the bath are positive. By đ, we denote an incomplete differential. The work $đw$ performed on the colloidal particle is provided exclusively by the external system. It can be transferred to the system either by external nonconservative forces or by changing the shape of the potential U through the external control parameter λ, see Fig. 3.2,

$$đw \equiv \partial_\lambda U \mathrm{d}\lambda + f \mathrm{d}x. \tag{3.4}$$

[1] Note that in a one-dimensional system without boundaries, any force can be derived from a potential U. However, employing periodic boundary conditions and a constant force f, there is no potential U with $-\partial_x U = f$ which is compatible with the periodicity. In the present context, we consider such a force as nonconservative.

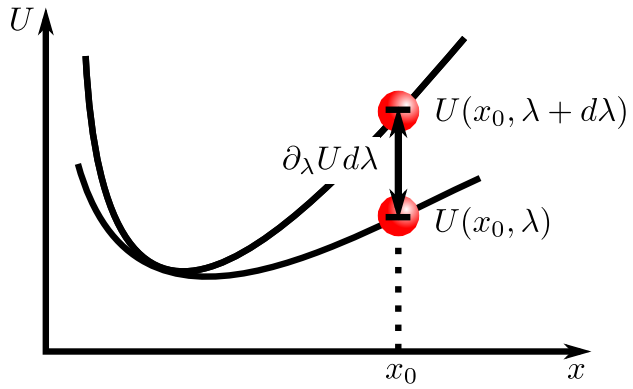

Figure 3.2.: Without nonconservative forces, work is defined as the change in the internal energy at fixed configuration.

With the change of the total energy in the system

$$\mathrm{d}U = \partial_\lambda U \mathrm{d}\lambda + \partial_x U \mathrm{d}x \tag{3.5}$$

and the first law along a trajectory, see Eq. (3.3), we obtain the heat exchanged with the heat bath

$$đq \equiv đw - \mathrm{d}U = -\partial_x U \mathrm{d}x + f \mathrm{d}x = F \mathrm{d}x. \tag{3.6}$$

It is straightforward to generalize these results to N particles in three dimensions

$$đw \equiv \partial_\lambda U \mathrm{d}\lambda + \sum_{i=1}^{N} \mathbf{f}_i \cdot \mathrm{d}\mathbf{r}_i, \tag{3.7}$$

$$\mathrm{d}U \equiv \partial_\lambda U \mathrm{d}\lambda + \sum_{i=1}^{N} \boldsymbol{\nabla}_i U \cdot \mathrm{d}\mathbf{r}_i, \tag{3.8}$$

$$đq \equiv \sum_{i=1}^{N} (-\boldsymbol{\nabla}_i U + \mathbf{f}_i) \cdot \mathrm{d}\mathbf{r}_i = \sum_{i=1}^{N} \mathbf{F}_i \cdot \mathrm{d}\mathbf{r}_i. \tag{3.9}$$

Note that $\mathrm{d}\mathbf{r}(t)$ includes stochastic contributions stemming from the noise in the Langevin equation. As in general the forces and potentials in Eqs. (3.7), (3.8), and (3.9) depend on $\mathbf{r}$, we are confronted with multiplicative noise, see Appendix B. Here, Eqs. (3.4) and (3.9) describe the physical quantities correctly only if we interpret the products according to the Stratonovich convention [10, 101]. Unless stated otherwise, we will implicitly assume this convention throughout this thesis.

External flow fields

So far, we have included external influences in two forms. First, by externally steering the potential U via λ. Second, by adding a nonconservative force $\mathbf{f}$. Additionally, there is a third way to act on the system externally. We can impose an external flow field $\mathbf{u}(\mathbf{r})$ to the solvent. One might wonder why such a flow field cannot be simply absorbed into the nonconservative force $\mathbf{f}$ by an additional term $\mu_0^{-1}\mathbf{u}(\mathbf{r})$. The reason is that a flow field affects a particle via the solvent, whereas forces act on the particle directly. This difference is essential for the definition of heat dissipation. To make this point more obvious, we consider a colloidal particle carried along with the flow. Of course, this particle does not dissipate any heat. Yet, if a force is dragging the same particle through a resting solvent at the same speed, heat is dissipated. Therefore, in the presence of an external flow field, the definition of the heat transfer into the solvent should be extended to [105]

$$đq \equiv \sum_{i=1}^{N}(-\boldsymbol{\nabla}_i U + \mathbf{f}_i)\cdot[\mathrm{d}\mathbf{r}_i - \mathbf{u}(\mathbf{r}_i)\mathrm{d}t] = \sum_{i=1}^{N}\mathbf{F}_i\cdot[\mathrm{d}\mathbf{r}_i - \mathbf{u}(\mathbf{r}_i)\mathrm{d}t]\,. \tag{3.10}$$

With Eq (3.8), we obtain the work

$$đw = \mathrm{d}U + đq = \partial_\lambda U\mathrm{d}\lambda + \sum_{i=1}^{N}\mathbf{f}_i\cdot[\mathrm{d}\mathbf{r}_i - \mathbf{u}(\mathbf{r}_i)\mathrm{d}t] + \boldsymbol{\nabla}_i U\cdot\mathbf{u}(\mathbf{r}_i)\mathrm{d}t. \tag{3.11}$$

We recognize the contributions already present in the case without external flow, cf. Eq. (3.9), in the first and the second term on the right-hand side. However, here, the latter gives rise to additional work only if the velocity of the particle deviates from the velocity of the local flow field. The third term describes the additional work performed by the solvent when pushing the particle up a potential gradient.

3.3. Harada-Sasa relation

Having defined work and dissipated heat along trajectories, the next step is to ask whether these quantities can be measured experimentally. The short answer is yes. One needs to record the particle trajectories and the corresponding forces acting on the particles at each point in time and to apply Eqs. (3.7) and (3.9) afterwards. The catch is that, in practice, details about the interaction are mostly unknown and hence forces cannot be inferred. For instance, the external force applied by a laser field beyond the paradigmatic harmonic trap [7] is quite tough to estimate [8,60]. Therefore, the ingredients required to infer dissipation from the first law in mesoscopic systems are, in general, out of reach.

An elegant way to determine the average dissipation rate in NESSs without the knowledge of interaction details has been put forward by Harada and Sasa [104] for overdamped Langevin dynamics. They relate the average heat production to the violation of a fluctuation-dissipation theorem (FDT) [81] in a NESS. Starting from the definition of heat dissipation along trajectories, we obtain the Harada-Sasa relation in a few steps [79]. For the overdamped Langevin dynamics defined in Eq. (3.1), the average heat transfer into the solvent is given by

$$\langle \dot{q} \rangle \equiv \langle \dot{x} F(x) \rangle = \left\langle \dot{x} \mu_0^{-1} \left[\dot{x} - \zeta \right] \right\rangle = \mu_0^{-1} \left[\left\langle \dot{x}^2 \right\rangle - \langle \dot{x} \zeta \rangle \right] . \tag{3.12}$$

We define the autocorrelation function for the velocity relative to the global mean velocity v^{s}

$$C(t) \equiv \left\langle [v(t) - v_i^{\mathrm{s}}][v(0) - v_j^{\mathrm{s}}] \right\rangle \tag{3.13}$$

and the linear response of the mean velocity to an external force f

$$R(t) \equiv \left. \frac{\delta \langle v(t) \rangle^f}{\delta f(0)} \right|_{f=0} , \tag{3.14}$$

where $\langle \cdot \rangle^f$ denotes an average in the perturbed system. Using a path integral approach, one can show that [18, 100]

$$TR(t) = \frac{1}{2} \langle v(t) \zeta(0) \rangle , \tag{3.15}$$

see Appendix C. We can therefore write Eq. (3.12) as

$$\begin{aligned} \langle \dot{q} \rangle &= \mu_0^{-1} \left\{ (v^{\mathrm{s}})^2 + C(0) - 2TR(0) \right\} \\ &= \mu_0^{-1} \left\{ (v^{\mathrm{s}})^2 + \int_{-\infty}^{\infty} \left[\bar{C}(\omega) - 2T \bar{R}'(\omega) \right] \frac{\mathrm{d}\omega}{2\pi} \right\} , \end{aligned} \tag{3.16}$$

where $\bar{C}$ and $\bar{R}$ are the Fourier transform of the correlation and the response function, respectively. The prime denotes the real part of a function. The straightforward generalization to N-particle systems reads

$$\langle \dot{q} \rangle = \sum_{i=1}^{N} \mu_{0,i}^{-1} \left\{ (\mathbf{v}_i^{\mathrm{s}})^2 + \int_{-\infty}^{\infty} \mathrm{Tr} \left[\bar{\mathsf{C}}_i(\omega) - 2T \bar{\mathsf{R}}_i'(\omega) \right] \frac{\mathrm{d}\omega}{2\pi} \right\} \tag{3.17}$$

with the trace operator $\mathrm{Tr}(\cdot)$ and the response and correlation functions replaced by the corresponding matrices.

A rigorous proof of the Harada-Sasa relation along with a generalization to many-body systems for both over and underdamped Langevin dynamics is given

in Ref. [14]. The relation was experimentally tested for an optically driven colloidal system [106] and applied to gain information about the nonequilibrium energetics of the F_1-ATPase [107]. Further generalizations and experiments applying this technique comprise Hamiltonian systems [108], Langevin systems including memory [109,110], quantum Langevin systems [111], and FDT violations involving field variables [112].

From a theoretical point of view, the fundamental insight gained from the Harada-Sasa relation is the direct connection between FDT violations and dissipation. From an experimental perspective, it provided the first, and so far only, way to measure dissipation in colloidal systems. However, this route is open only if correlation and response functions are accessible in the experiment. Determining the latter for driven colloidal systems often poses a nontrivial and time-consuming task for the following reasons. First, the system must be perturbed from its steady state, which needs to be done separately for each degree of freedom. Second, this perturbation must be sufficiently small to stay within the linear response regime, which can result in a low signal-to-noise ratio. Another difficulty arises from the limits in the integration over frequencies in Eq. (3.16). Of course, one cannot measure up to infinitely high ω and must therefore choose a cut-off frequency which is sufficiently high to obtain a good approximation for the integral. However, in the high-frequency regime, technical issues such as a limited sampling rate, a finite exposure time, and the noise inherent to the measurement devices limit the accuracy of any experiment [107].

The main drawback of this method boils down to the fact that one needs to determine the full time-dependent response and correlation functions but in the end only requires the integral over their difference. One thus needs to put much experimental effort into the extraction of information, the better part of which remains unused. In the following, we will address the question whether there is a more efficient way to measure dissipation in colloidal systems.

3.4. Noninvasive measurement of dissipation

In both experiments and simulations, good statistics for NESS trajectories of colloidal particles are often readily available. In the following, we will show how to extract the average dissipation rate from this data. In particular, we will employ a conditional averaging procedure on the trajectories from which the mean local velocity field can be obtained. Combined with the measured stationary distribution, this field yields the average heat production rate. Here, there is no need to perturb the system since only steady-state trajectories are required as input. Therefore, we call this procedure noninvasive. This point constitutes a main advantage of this approach as issues connected with the application of external perturbations are

evaded. Moreover, the effort to create the statistics necessary for the evaluation is relatively small for typical systems. This method complements the one given by Harada and Sasa by making the average heat production rate easily inferable from steady-state trajectories.

Starting from the definition of heat dissipation along a trajectory $x(\tau)$, see Eq. (3.6), the average heat production rate in a NESS for the dynamics given in Eq. (3.1) reads

$$\langle \dot{q} \rangle \equiv \langle \dot{x} F(x) \rangle \,. \tag{3.18}$$

The average can be split into two steps. The average over all realizations of the stochastic velocity at fixed configuration x, and the subsequent average over the configuration space [3]. Performing only the first step yields [3]

$$\langle \dot{q} \rangle = \langle \nu^{\mathrm{s}}(x) F(x) \rangle \tag{3.19}$$

with the stationary mean local velocity

$$\nu^{\mathrm{s}}(x) \equiv \langle \dot{x} | x \rangle = \frac{j^{\mathrm{s}}(x)}{\Psi^{\mathrm{s}}(x)} = \mu_0 F(x) - D_0 \partial_x \ln \Psi^{\mathrm{s}}(x), \tag{3.20}$$

see Eq. (2.17), the stationary pdf Ψ^{s}, and the stationary probability current j^{s}. We eliminate the force in Eq. (3.19) using Eq. (3.20) and write the remaining average over the configurations as

$$\langle \dot{q} \rangle = \mu_0^{-1} \int \nu^{\mathrm{s}}(x)^2 \Psi^{\mathrm{s}}(x) \mathrm{d}x + T \int \nu^{\mathrm{s}}(x) \partial_x \Psi^{\mathrm{s}}(x) \mathrm{d}x. \tag{3.21}$$

In a stationary state, the probability currents become divergence-free, i. e., $\partial_x j^{\mathrm{s}} = 0$, in one dimension they are even constant, see Eq. (2.12). Exploiting this property, the second term on the right-hand side vanishes

$$\int \nu^{\mathrm{s}}(x) \partial_x \Psi^{\mathrm{s}}(x) \mathrm{d}x = \int j^{\mathrm{s}}(x) \partial_x \ln \Psi^{\mathrm{s}}(x) \mathrm{d}x = - \int \partial_x j^{\mathrm{s}}(x) \ln \Psi^{\mathrm{s}}(x) \mathrm{d}x = 0, \tag{3.22}$$

where we have used a partial integration with a vanishing boundary term. Therefore, the average heat production rate is

$$\langle \dot{q} \rangle = \mu_0^{-1} \int \nu^{\mathrm{s}}(x)^2 \Psi^{\mathrm{s}}(x) \mathrm{d}x = \mu_0^{-1} \left\langle \nu^{\mathrm{s}}(x)^2 \right\rangle . \tag{3.23}$$

The generalization to N particles in arbitrary many spatial dimensions is straightforward and reads

$$\langle \dot{q} \rangle = \sum_{i=1}^{N} \mu_{0,i}^{-1} \left\langle \boldsymbol{\nu}_i^{\mathrm{s}}(\mathbf{R})^2 \right\rangle . \tag{3.24}$$

For the computation of the average heat production rate, we merely need the bare mobility μ_0 and the mean local velocity field as input. The latter can be obtained via Eq. (2.17) from a long steady-state trajectory.

Hydrodynamic interaction

So far, we have neglected hydrodynamic interactions in our treatment of dissipation. However, a colloidal particle moving through the solvent drags the surrounding liquid along. Therefore, other particles in the vicinity are not moving through a quiescent solvent but through the flow field induced by the moving particle. Likewise, the neighboring particles in turn act back on the moving one and alter the local flow field at its position. Analogously to the role of external flow fields discussed in Sect. 3.2, this point should affect heat dissipation as well. Instead of the particle velocity, the velocity in relation to the surrounding flow field then becomes the relevant quantity. Hence, Eq. (3.24) needs to be modified accordingly. Using the definition for heat dissipation given in Eq. (3.10), we have

$$\langle \dot{q} \rangle \equiv \sum_{i=1}^{N} \langle [\dot{\mathbf{r}}_i - \mathbf{u}_i(\mathbf{R})] \cdot \mathbf{F}_i(\mathbf{R}) \rangle \tag{3.25}$$

with the hydrodynamic flow field

$$\mathbf{u}_i(\mathbf{R}) = \sum_{j \neq i} \mu_{ij}(\mathbf{R}) \mathbf{F}_j(\mathbf{R}). \tag{3.26}$$

In the case of two hydrodynamically interacting spheres in three dimensions, we can approximate μ_{ij} up to the Rotne-Prager level [96, 113, 114], cf. Appendix A, as

$$\mu_{ii} = \mu_0 \mathbb{1}, \tag{3.27}$$

$$\mu_{ij}(\mathbf{r}_{ij}) = \frac{3}{8}\mu_0 \frac{a}{r_{ij}} \left(\mathbb{1} + \frac{\mathbf{r}_{ij}\mathbf{r}_{ij}^{\mathrm{T}}}{r_{ij}^2} \right) + \frac{1}{4}\mu_0 \left(\frac{a}{r_{ij}} \right)^3 \left(\mathbb{1} - 3\frac{\mathbf{r}_{ij}\mathbf{r}_{ij}^{\mathrm{T}}}{r_{ij}^2} \right), \quad \text{for} \quad i \neq j, \tag{3.28}$$

with $r_{ij} \equiv |\mathbf{r}_{ij}|$. Note that this approximation incorporates only two-body interactions and that the accuracy of the underlying expansion decreases with increasing ratio a/r_{ij}.

Again, we evaluate the average in Eq. (3.25) at fixed configuration $\mathbf{R}$ and substitute Eq. (3.26) for the flow field,

$$\begin{aligned} \langle \dot{q} \rangle &= \sum_{i=1}^{N} \left\langle (\boldsymbol{\nu}_i^{\mathrm{s}} - \sum_{j \neq i} \mu_{ij} \mathbf{F}_j) \cdot \mathbf{F}_i \right\rangle \\ &= \sum_{i=1}^{N} \langle \boldsymbol{\nu}_i^{\mathrm{s}} \cdot \mathbf{F}_i \rangle - \sum_{i,j=1}^{N} \langle \mu_{ij} \mathbf{F}_j \cdot \mathbf{F}_i \rangle + \sum_{i=1}^{N} \mu_0 \left\langle \mathbf{F}_i^2 \right\rangle, \end{aligned} \tag{3.29}$$

where we suppress the dependence on $\mathbf{R}$ for ease of notation. Using Eq. (2.18) and the stationary Fokker-Planck equation, we obtain the average heat production rate

$$\begin{aligned}\langle \dot{q} \rangle &= \mu_0 \sum_{i=1}^{N} \left\langle \mathbf{F}_i^2 \right\rangle - \sum_{i,j=1}^{N} T \left\langle \mu_{ij} \boldsymbol{\nabla}_j \ln \Psi^{\mathrm{s}} \cdot \mathbf{F}_i \right\rangle \\ &= \mu_0 \sum_{i,j,k=1}^{N} \left\langle \mu_{ik}^{-1} \boldsymbol{\nu}_k^{\mathrm{s}} \cdot \mu_{ij}^{-1} \boldsymbol{\nu}_j^{\mathrm{s}} \right\rangle + 2\mu_0 T \sum_{i,j=1}^{N} \left\langle \mu_{ij}^{-1} \boldsymbol{\nu}_j^{\mathrm{s}} \cdot \boldsymbol{\nabla}_i \ln \Psi^{\mathrm{s}} \right\rangle \\ &\qquad + T^2 \sum_{i,j=1}^{N} \left\langle \boldsymbol{\nabla}_i \ln \Psi^{\mathrm{s}} \cdot (\mu_0 \mathbb{1} \delta_{ij} - \mu_{ij}) \boldsymbol{\nabla}_j \ln \Psi^{\mathrm{s}} \right\rangle . \end{aligned} \tag{3.30}$$

With Eq. (3.22), it is straightforward to check that for negligible hydrodynamic interaction, i. e., for $\mu_{ij} = \mu_0 \mathbb{1} \delta_{ij}$, the right-hand side reduces to Eq. (3.24). In contrast to the case without hydrodynamic interaction, this result depends on gradient of the logarithm of the stationary pdf in addition to the mean local velocities and the mobility matrices. Yet, this quantity can still be easily obtained from a long trajectory. Therefore, to include hydrodynamics, we do not need any additional experimental input if an appropriate approximation for the mobility matrices is available.

3.5. Applicability to a realistic system

We have derived the average heat production rate from nothing but fundamental definitions and the dynamics of the system. Merely in the treatment of hydrodynamic interactions approximations do enter in the form of the Rotne-Prager tensor. Hence, there is no point in checking the correctness of Eq. (3.24) in an experiment or simulation. In practice, however, the accuracy to which, for instance, the mean local velocity field can be obtained is limited. In configuration-space regions rarely visited by the system, no data might be obtainable at all. These difficulties can affect the quality of the results generated by this method. As precisely the facilitation of the practical measurement of dissipation is the main objective in this context, it is crucial to check this point for a realistic colloidal system.

Such a test can be conducted by employing Langevin dynamics simulations. This class of simulations combines two properties essential for such a task. First, steady-state trajectories of the same form as those obtained from experiments are created. Second, details about the interaction are known, allowing for a direct determination of the heat dissipation via Eq. (3.9). We can thus benefit from reliable reference results.

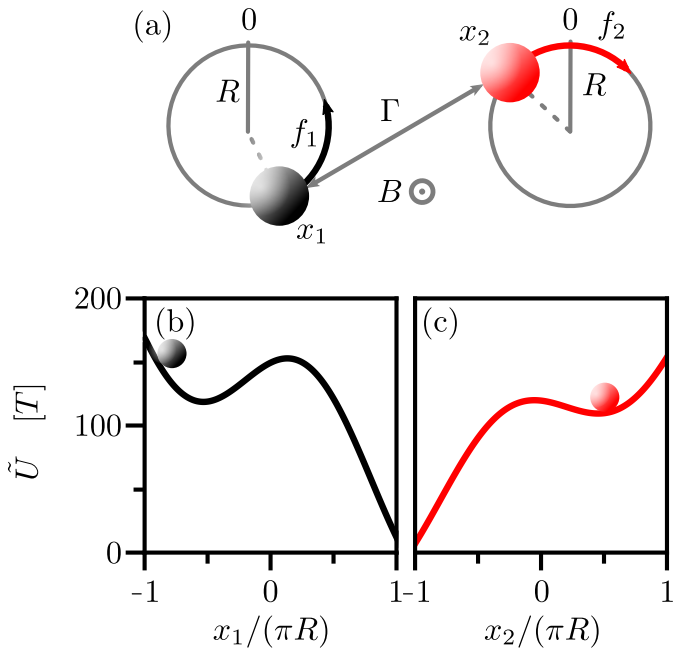

Figure 3.3.: (a) Schematic sketch of the system: Two paramagnetic colloidal particles driven along two rings of radius R by constant forces f_i. The coordinates $x_i \in (-\pi R, \pi R]$ are given by the corresponding arc length measured in counterclockwise direction. The magnetic field B perpendicular to the rings induces a magnetic moment parallel to the magnetic field in each particle. The strength of the resulting interaction is described by the dimensionless coupling parameter Γ. As indicated by the arrows, the driving forces are chosen such that the left particle moves in counterclockwise direction while the right particle moves in clockwise direction. (b)-(c) Potential landscape on the left and right ring, respectively, in the uncoupled case for parameter set *III* in Table 3.1.

Regarding the choice of the specific system, we should mention that for a serious investigation of the present method's practical value, a one-dimensional system is insufficient. The crucial point is that a one-dimensional stationary probability current is always constant in space, see Eq. (2.12). Measuring the mean local velocity field then reduces essentially to the measurement of the pdf [115], which in many cases is done quite easily in a one-dimensional system. In order to provide a meaningful test, we investigate the following two-dimensional, experimentally accessible system in a Langevin dynamics simulation [15, 16]. Two paramagnetic colloidal particles are driven by constant forces f_i along two nonoverlapping rings of radius R, see Fig. 3.3. In addition to the constant forces, we impose a sinusoidal potential $U_i(x_i) = A_i \sin(x_i/R - \phi_i)$ of amplitude A_i and phase shift ϕ_i on each ring leading to the tilted (nonperiodic) potential $\tilde{U}_i(x_i) \equiv U_i(x_i) - f_i x_i$, see Fig. 3.3(b) and (c). By applying a small homogeneous magnetic field of strength B normal to the plane containing the rings, the particles acquire parallel magnetic dipole moments of magnitude $M \approx \chi B$ with $\chi \simeq 5.9 \times 10^{-12}$ Am^2/T. The resulting repulsive interaction is described by the potential $W(\mathbf{x}) = \mu M^2/[\pi r^3(\mathbf{x})]$, where μ is the magnetic constant and $r(\mathbf{x})$ is the distance between the particles with $\mathbf{x} \equiv (x_1, x_2)$. We quantify the interaction strength by introducing the dimensionless coupling constant $\Gamma \equiv \Delta W/T$, often referred to as plasma parameter, where ΔW is the difference between the maximal and minimal interaction energy. The total force acting on the ith particle is then given by

$$F_i(\mathbf{x}) = f_i - \partial_{x_i}[U_i(x_i) + W(\mathbf{x})] \quad \text{for} \quad i \in \{1, 2\} \tag{3.31}$$

and the dynamics of the system is defined by the Langevin equation

$$\dot{x}_i = \mu_0 F_i(\mathbf{x}) + \zeta_i, \tag{3.32}$$

cf. Eq. (2.5), where we neglect hydrodynamic interactions and assume a resting solvent. We integrate the equations of motion numerically using the Milstein scheme [116] with a time step $\Delta t = 0.0001\ (\mu\text{m})^2/(\mu_0 T)$.

The central task in the application of Eq. (3.24) is the determination of the mean local velocity fields ν_i^{s} and the pdf Ψ^{s}. In order to judge the quality of the results, we determine the force field $\mathbf{F}(\mathbf{x}) \equiv (F_1(\mathbf{x}), F_2(\mathbf{x}))^{\text{T}}$ in two independent ways. First, we compute $\mathbf{F}(\mathbf{x})$ analytically, which is possible since details about the potential parameters are known in this simulation. Second, we determine the forces via Eq. (3.20) by evaluating $\nu_i^{\text{s}}(\mathbf{x})$ and $\Psi^{\text{s}}(\mathbf{x})$ from the simulated data. A comparison of the two independently determined force fields yields a very good agreement, see Fig. 3.4.

In the next step, we compute the average heat production rate in the system from a long trajectory in two different ways:

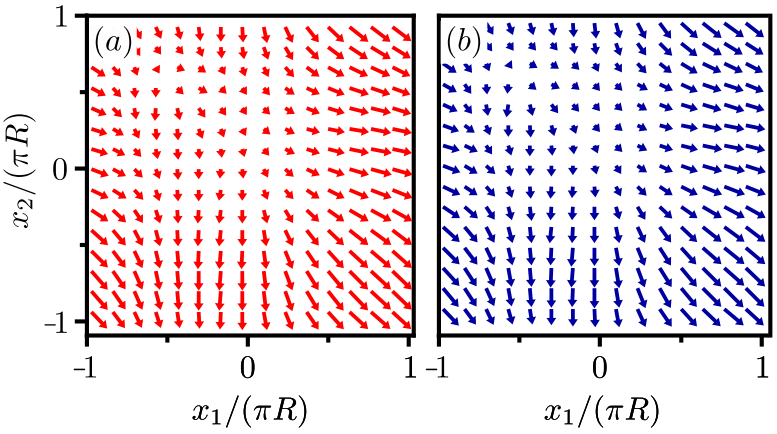

Figure 3.4.: Comparison between the force fields $\mathbf{F}(\mathbf{x})$ computed (a) analytically and (b) from simulated NESS trajectories via Eq. (3.20) for parameter set I in Table 3.1.

(A) We use the trajectory-based method introduced in this chapter, i. e., we determine ν_i^{s} and Ψ^{s} from the simulated trajectories and use Eq. (3.24) to obtain $\langle \dot{q} \rangle$.

(B) We determine the heat production rate directly via Eq. (3.9) by using the knowledge of the forces acting on the particles along the trajectory. This procedure then yields the reference result, i. e., the true average heat production rate along this particular trajectory.

In Fig. 3.5, we juxtapose the results determined by method (A) and (B) for the three different parameter sets given in Table 3.1 and find a very good agreement, in support of the consistency between our approach (A) and the reference result (B).

A difficult point in the application of method (A) is the determination of the mean local velocity field ν_i^{s} for configurations in which the system is found only with a low probability. We also address this difficulty in our test. Specifically, we choose the parameter sets II and III such that ν_i^{s} can only be obtained in a part of the configuration space, see Fig. 3.5(c) and (d). In spite of this impediment, the results for $\langle \dot{q} \rangle$ still match the reference results very accurately. This point can be understood as follows. The average heat production rate $\langle \dot{q} \rangle$ is computed from an integral in which the square of the mean local velocity enters weighted by the probability density, see Eq. (3.23). Since poor statistics for $\nu_i^{\mathrm{s}}(\mathbf{x})$ are expected typically in regions where $\Psi^{\mathrm{s}}(\mathbf{x})$ is also very low, the contribution of these parts of the data to $\langle \dot{q} \rangle$ is thus only minor, provided that the ν_i^{s} stay finite. This property holds for our system and should also be true for many other well-behaved systems.

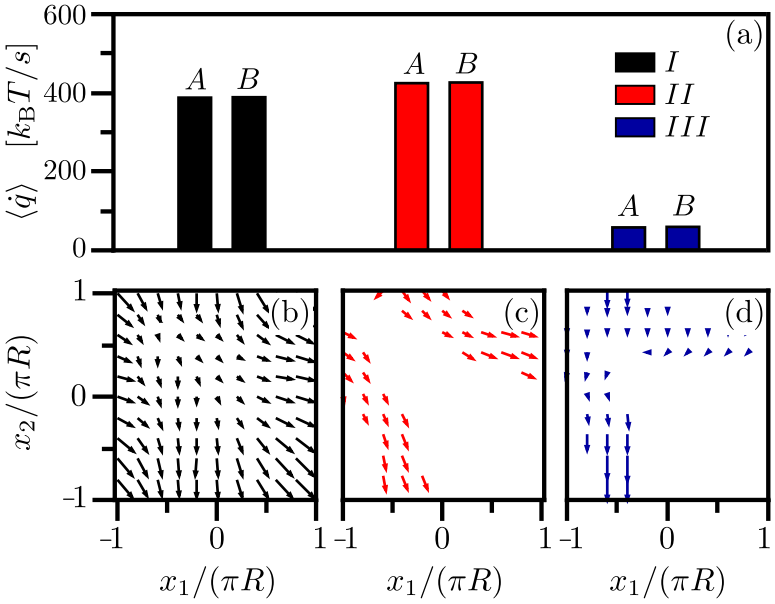

Figure 3.5.: (a) Average heat production rates $\langle \dot{q} \rangle$ obtained from methods (A) and (B) for the three different parameter sets I, II, and III given in Table 3.1. To relate $\langle \dot{q} \rangle$ to an experimental scale, we choose $a = 5.2$ µm. Error bars are smaller than 1%. (b)-(d) Corresponding mean local velocity fields evaluated in the process of determining $\langle \dot{q} \rangle$. Regions without arrows are rarely visited by the system.

Thus, for the measurement of averaged quantities such as $\langle \dot{q} \rangle$, only regions in configuration space of substantial weight must be sampled accurately. Regions of minor probability merely add small-sized corrections to the result.

3.6. Heat dissipation and hydrodynamics in an experimental system

Having demonstrated the validity and applicability of the method in a Langevin simulation, the next and final step is to employ this technique to measure dissipation in an experimental realization of the above system [16]. For this purpose, the focus of a three-dimensional optical trap [4, 5], created by a laser beam of wavelength 1070 nm, is moved rapidly along two nonoverlapping, coplanar rings. The rings have a radius of $R = 3.5$ µm and a center-to-center distance of 17.0 µm. On each ring, we place a paramagnetic colloidal particle of diameter $a = 5.2$ µm and magnetic polarizability $\chi \simeq 5.9 \times 10^{-12}$ Am^2/T (cf. Langevin simulation). Strong viscous forces due to the quick motion of the trap prevent the colloidal particles

	I	II	III
Γ	310.0	670.0	310.0
f_1 [T/μm]	50.0	56.0	25.0
f_2 [T/μm]	−65.0	−54.0	−35.0
A_1 [T]	225.0	175.0	175.0
A_2 [T]	175.0	170.0	175.0
ϕ_1	$-\pi/5$	$-\pi/5$	$-\pi/5$
ϕ_2	$-4\pi/5$	$-4\pi/5$	$-4\pi/5$
R [μm]	3.5	3.5	3.5
center-center distance [μm]	17.0	17.0	17.0

Table 3.1.: Parameter sets I, II, III.

from being dragged along [117]. Instead, the laser focus runs over the particles very quickly. In the process, they experience a short kick along the trajectory of the trap and are forced towards the focus in the direction perpendicular to this trajectory. In the time interval between two such kicks, the particles diffuse freely. In this case, these intervals are short compared to both the observation time scale and the diffusive time scale. This point has two important implications. First, as single kicks cannot be resolved, they can be effectively described by a constant tangential force f_i exerted on the ith particle. Apart from this force, the particle is diffusing freely along the ring. Second, in the radial direction, the particles barely have time to diffuse away from the rings. This point effectively confines their motion to one dimension. Moreover, by modulating the intensity of the laser beam, an effective optical potential $U_i(x_i)$ can be imposed on each ring. The interaction between the two particles is of the same form as described for the Langevin dynamics simulation. Here, we use magnetic fields of magnitudes $B \leq 40$ mT resulting in coupling constants in the range of $0 \leq \Gamma \leq 1100$. We record the particle trajectories using digital video microscopy with a spatial and temporal resolution of 20 nm and 25 ms, respectively.[2]

In Fig. 3.6(a), we show the average heat production rate as a function of Γ with [gray bars obtained via Eq. (3.30)] and without [red bars via Eq. (3.24)] hydrodynamic interaction. Note that no matter which of the two equations we choose in order to evaluate the average heat production rate, we always use the same set of experimental trajectories as input. Of course, these trajectories follow the full dynamics of the system including hydrodynamic interactions. Consequently, the average heat dissipation rate evaluated via Eq. (3.24) contains the correct hydrodynamic mean local velocity fields and pdfs shown in Figs. (3.6)(b) and (c) but

[2]Experiments were performed by J. Mehl. For a detailed experimental description refer to Ref. [51].

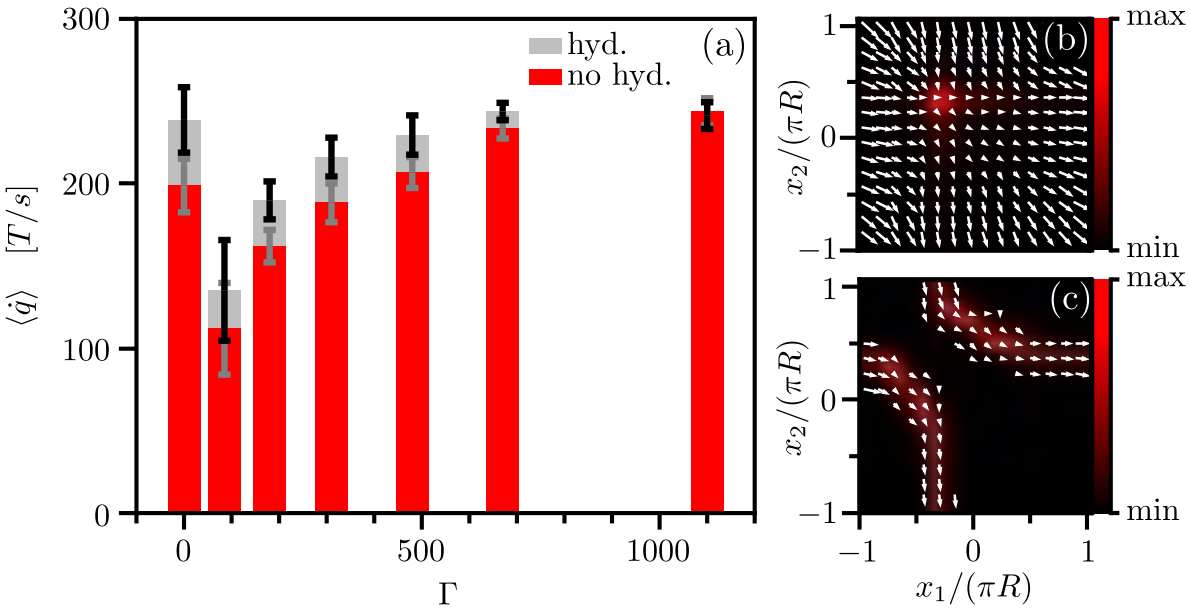

Figure 3.6.: (a) Average heat production rate $\langle \dot{q} \rangle$ as a function of the coupling strength Γ with standard error bars. The potentials on the left and right ring are approximately sinusoidal with amplitudes $A_1 = 175$ T and $A_2 = 164$ T, respectively. The driving forces are $f_1 = 56$ T/µm and $f_2 = -51$ T/µm. The red (gray) bars are computed without (with) hydrodynamic correction terms. (b),(c) Mean local velocity fields ν_i^s (white arrows) over the corresponding pdf in configuration space for coupling constants (b) $\Gamma = 0$ and (c) $\Gamma = 1100$.

misses the hydrodynamic correction terms contained in Eq. (3.30). Apparently, these hydrodynamic terms add measurable corrections for $\Gamma \lesssim 500$ but do not change the qualitative behavior of $\langle \dot{q} \rangle$ in dependence of Γ. In the following, we will discuss this qualitative dependence first and focus on the role of the hydrodynamic correction terms later.

Nonmonotonous dependence of $\langle \dot{q} \rangle$ on Γ

The most prominent feature in Fig. 3.6(a) is that $\langle \dot{q} \rangle$ depends nonmonotonously on Γ. The origin of this feature lies in a transition between two distinct dynamical steady states mediated by Γ. These states are characterized by their qualitatively different pdfs shown together with their corresponding mean local velocity fields in Figs. 3.6(b) and (c) for $\Gamma = 0$ and 1100, respectively.

In the absence of coupling, the particles move independently along their rings. The average time for a round-trip is 12 s, and the particles spend the longest part of their revolutions in the proximity of the, relatively shallow, local potential

minima. There, they fluctuate at small mean local velocities. These minima are located at $x_1/R \simeq -\pi/4$ and $x_2/R \simeq \pi/4$, i. e., at relatively short particle distances. The steep parts in the potential landscape are traversed rapidly leading to large mean local velocities and small probabilities for the occurrence of such configurations, see Fig. 3.6(b). A large Γ has a significant effect on the shape of the pdf in the steady state. The entailing strong repulsive interaction makes configurations with short particle distances energetically unfavorable. Hence, if the particles are close to their local potential minima simultaneously, at least one of the particles will be pushed over the shallow potential barrier at the boundary of its local minimum. This point initiates the following mechanism, see Fig. 3.7. While one particle fluctuates around its local minimum, the other one is "running" down the steep part of the potential on its ring. Once this "running" particle approaches its local potential minimum again, it pushes the "resting" particle out of its potential valley. Now, the roles switch and the formerly "running" particle "rests" in its potential minimum, while the formerly "resting" particle is "running" down its potential hill. This mechanism reduces the time both particles spend in their local potential minima considerably. Moreover, the particles cannot overtake one another anymore, which results in a highly synchronized pattern of motion, see Fig. 3.6(c). In the crossover regime between these two dynamical steady states, the particles do repel each other, but they can still overtake one another. During such an overtaking process, the faster particle can hinder the slower one in overcoming the potential barrier effectively slowing down the motion.

With this mechanism in mind, we can understand the nonmonotonous dependence of $\langle \dot{q} \rangle$ on Γ, see Fig. 3.6(a). Going from zero to small coupling constants, the motion of the particles slows down due to the repulsive interaction, reducing the average heat production rate in the process. A further increase of Γ leads to the synchronized pattern of motion described above, cf. Fig. 3.7. In this mode, the time the particles spend fluctuating in their potential valleys is considerably reduced, which in turn increases the weight of the highly dissipative trajectories of particles running down the steep potential hills. These changes result in a larger average dissipation rate.

Hydrodynamic interaction

In order to include hydrodynamics in the computation of the average dissipation rate via Eq. (3.30), we need the appropriate mobility tensor. Although the Rotne-Prager tensor given in Eqs. (3.27) and (3.28) provides a good starting point, it cannot be used without adaption. The point is that this tensor was derived as an approximation for two hydrodynamically interacting spheres in three spatial dimensions. Here, the hydrodynamic interaction is mediated via a three-dimensional medium as well. However, the motion of the particles is restricted to a single dimen-

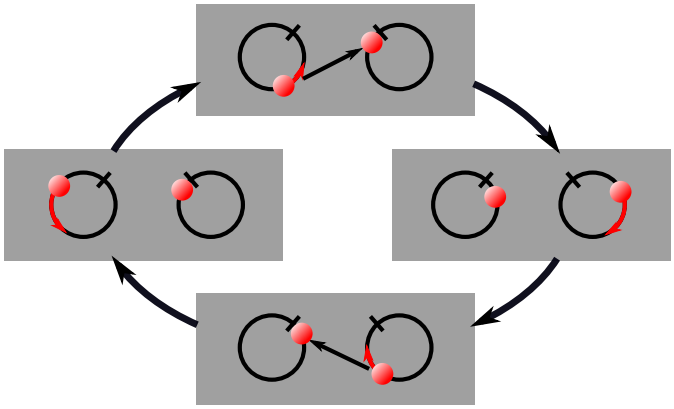

Figure 3.7.: Sketch of the dynamical mechanism. Upper picture: In the process of completing a circulation, the left particle pushes the right one over its potential barrier depicted by the bar blocking the path. Right picture: The left particle cannot overcome the barrier and is fluctuating in front of it, while the right particle quickly completes a circulation. Lower picture: Arriving again at its barrier, the right particle pushes the left one over the barrier. Left picture: The right particle is fluctuating in front of the potential barrier, while the left one quickly completes a circulation.

sion each. Consequently, we need to project the full mobility tensor $\boldsymbol{\mu}_{ij}$, consisting of four 3×3 matrices, onto four 1×1 matrices μ_{ij} coupling the one-dimensional motion of the two particles. How this projection is done in particular can be seen by writing the effective dynamics as a projection of the full three-dimensional Langevin equations

$$\dot{x}_i = \mathbf{e}_i \cdot \dot{\mathbf{r}}_i = \sum_{j=1}^{2} \mathbf{e}_i \cdot \boldsymbol{\mu}_{ij} \mathbf{F}_j + \mathbf{e}_i \cdot \boldsymbol{\zeta}_i = \sum_{j=1}^{2} \mathbf{e}_i \cdot \boldsymbol{\mu}_{ij} \mathbf{e}_j F_j + \zeta_i \equiv \sum_{j=1}^{2} \mu_{ij} F_j + \zeta_i, \quad (3.33)$$

where, for the sake of clarity, we refrain from making the dependence of the mobility and the forces on the particle coordinates explicit. Here, we used that, as each particle is confined to its ring, all forces act parallel to the normalized vectors $\mathbf{e}_i(x_i) \equiv (-\sin x_i, \cos x_i, 0)^{\mathrm{T}}$ spanning a basis of the effectively two-dimensional system. Thus, we have $\mathbf{F}_i = F_i \mathbf{e}_i$ and $\boldsymbol{\zeta}_i = \zeta_i \mathbf{e}_i$. The symmetric mobility matrix of the confined dynamics is given by

$$\mu_{ij}(\mathbf{x}) \equiv \mathbf{e}_i(x_i) \cdot \boldsymbol{\mu}_{ij}(\mathbf{x}) \mathbf{e}_j(x_j), \quad (3.34)$$

in which the diagonal elements have the simple form $\mu_{ii}(\mathbf{x}) = \mu_0$. The resulting hydrodynamic corrections to the average heat production rate shown in Fig. 3.6(a) increase $\langle \dot{q} \rangle$ by roughly 20% for small Γ, while there is no significant effect for large

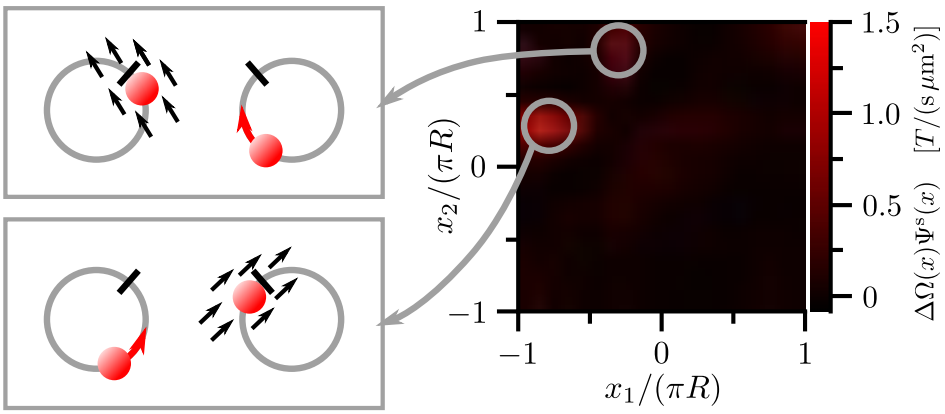

Figure 3.8.: Left: Sketch of mechanism leading to the main deviation from the average heat production rate. The moving particle causes a hydrodynamic flow field, depicted as black arrows, at the position of the resting particle. The resting particle is not advected by the flow due to a potential barrier marked by the black bar. The resulting nonzero velocity in relation to the flow field causes an additional heat production compared to the case neglecting hydrodynamics. As the system is not perfectly symmetric, the configurations do not contribute equally. The configuration depicted in the lower panel is dominant. Right: Hydrodynamic correction term for the average local heat production rate.

Γ. In order to figure out the mechanism leading to this type of contribution, we investigate the average *local* heat production rates

$$\Omega(\mathbf{x}) \equiv \Omega_0(\mathbf{x}) + \Delta\Omega(\mathbf{x}) \tag{3.35}$$

and

$$\Omega_0(\mathbf{x}) \equiv \mu_0^{-1} \sum_{i=1}^{2} \nu_i^2(\mathbf{x}), \tag{3.36}$$

with and without hydrodynamic interactions, respectively. The hydrodynamic correction terms cause the additional average local heat production rate

$$\begin{aligned}\Delta\Omega(\mathbf{x}) \equiv{}& 2\mu_0 \frac{\nu_1(\mathbf{x})\nu_2(\mathbf{x})}{\mu_{12}(\mathbf{x})^2} - 2T^2 \mu_{12}(\mathbf{x})[\partial_{x_1} \ln \Psi^{\mathrm{s}}(\mathbf{x})][\partial_{x_2} \ln \Psi^{\mathrm{s}}(\mathbf{x})] \\ &+ 2\mu_0 T \sum_{i,j=1}^{2} \mu_{ij}^{-1}(\mathbf{x}) \nu_j(\mathbf{x}) \partial_{x_i} \ln \Psi^{\mathrm{s}}(\mathbf{x}),\end{aligned} \tag{3.37}$$

which follows from Eqs. (3.24) and (3.30) after a simple calculation using the projected mobility tensor. Note that taking the mean of the average *local* heat production rate over configuration space yields the average *global* heat production rate. By considering $\Delta\Omega(\mathbf{x})$ weighted with the stationary pdf $\Psi^{\mathrm{s}}(\mathbf{x})$, we can identify the configurations with the largest contribution to the difference in the average global heat production rate, see Fig. 3.8. The quantitative difference caused by the hydrodynamic correction terms can be traced back to the contribution of essentially two symmetric configurations. In these configurations, one particle is fluctuating around its local potential minimum, while the other one is approaching it frontally and rapidly. Without the magnetic repulsion, the potential barrier is strong enough to help the fluctuating particle resist the hydrodynamic flow field generated by the approaching particle. This resistance against the flow field is dissipating heat in the process. For strong coupling, the repulsion is strong enough to simply push the fluctuating particle over the potential barrier, cf. Fig. 3.7. The particle is then able to follow the hydrodynamic flow field more accurately and less additional heat is dissipated. Note that this result depends strongly on the specific system. In general, hydrodynamics can cause a negative correction just as well as a positive one.

3.7. Conclusion and outlook

In this chapter, we have introduced an approach to determine the average heat production rate for colloidal systems in a NESS. While the so far only method

introduced by Harada and Sasa quantifies dissipation via response and correlation functions, the present method exclusively uses information obtained from steady-state trajectories without the need to perturb the system. In particular, the method neither requires any information about the underlying potentials nor about the driving forces. Moreover, for measuring the average heat production, only parts of the configuration space with a significant weight are important. This point makes the application of the method to experiments very convenient as good statistics are only needed for such configurations in which good statistics are easily achieved anyway. Thus, if the relevant configuration space stays sufficiently small, the method can still be applied to interacting systems with a larger number of degrees of freedom. Therefore, the approach constitutes a complementary way to measure dissipation, which is easily implemented, particularly in setups for small colloidal systems. Moreover, we have shown that hydrodynamic interactions can be incorporated in the scheme, where we require additional information only about the geometry of the particles and the boundary conditions.

For future work, it would be interesting to check the usefulness of this method for other nonequilibrium systems. Particularly interesting examples are molecular motors such as the F_1-ATPase. In an experiment, the state of such a motor is inferred indirectly from an attached probe [77]. In principle, to apply our method, we need the trajectories of both the attached probe and the motor. However, although the state of the motor is not detectable directly, one should be able to reliably estimate its state from the trajectory of the probe if the motor is moving sufficiently slowly. Moreover, by replacing the stationary distribution function and the stationary mean local velocity field by their time-dependent counterparts, a generalization of the present method should also be applicable to relaxing and time-dependent systems.

4. Hidden degrees of freedom in the fluctuation theorem

4.1. Introduction

In general, the description of mesoscopic systems is possible only if we accept some degree of coarse graining. Knowledge about the dynamics of all the solvent particles surrounding a colloidal particle, for instance, is neither available nor necessary to describe most relevant physical properties. Hidden degrees of freedom are usually accounted for in some effective way, e. g., as Gaussian white noise in the Langevin equation. Such an effective description is justified if a time-scale separation in the dynamics of observed and unobserved degrees of freedom exists. In the description of mesoscopic systems, such time-scale separations are exploited, for instance, in the effective treatment of solvent molecules or in the negligence of momenta in the overdamped dynamics of colloidal particles. However, in systems without a clear-cut time-scale separation, neglecting hidden degrees of freedom naively can lead to inconsistencies.

In this chapter, we investigate the role of slow hidden degrees of freedom for a most relevant concept: entropy production. More precisely, we scrutinize this issue for the fluctuation theorem (FT), an important symmetry relation characterizing the fluctuations of entropy in a NESS [16].

4.2. Stochastic entropy

In the previous chapter, we have discussed how the first law of thermodynamics can be transferred to fluctuating mesoscopic systems. The next step is to ask whether the concept of entropy, the central quantity of the second law of thermodynamics, can be extended to the level of fluctuating trajectories as well. A consistent definition for such a *stochastic entropy* was suggested by Seifert in 2005 [3]. In this section, we discuss the stochastic entropy along the lines of Ref. [3].

For simplicity, we start with the one-dimensional dynamics already defined in the preceding chapter by Eq. (3.1). The total system consists of two parts: the mesoscopic system and the surrounding heat bath. Therefore, we need to consider also two contributions to the total stochastic entropy: the stochastic system

entropy and the stochastic medium entropy. The former is defined as

$$s(\tau) \equiv -\ln \Psi(x(\tau), \tau) \tag{4.1}$$

with the, in general, time-dependent solution of the Fokker-Planck equation (2.12) Ψ evaluated along the trajectory $x(\tau)$ for $\tau \in [0, t]$. The entropy is thus a function of the fluctuating configuration of the system and becomes a fluctuating quantity itself. This definition is motivated by the fact that the ensemble average of s is equivalent to the nonequilibrium Gibbs entropy

$$\langle s(\tau) \rangle = -\int \ln \Psi(x, \tau) \Psi(x, \tau) \mathrm{d}x \equiv S(\tau). \tag{4.2}$$

Moreover, in thermal equilibrium, the stochastic entropy obeys the thermodynamic relation $s(\tau) = [U(x(\tau)) - \mathcal{F}]/T$ with the free energy [3]

$$\mathcal{F} \equiv -T \ln \int \exp\left[-U(x)/T\right] \mathrm{d}x. \tag{4.3}$$

The entropy change in the surrounding medium should be identified with the heat flux from the system into the surrounding solvent, cf. Eq. (3.6),

$$\Delta s_{\mathrm{m}}[x(\tau)] \equiv q[x(\tau)]/T = \frac{1}{T} \int_0^t F(x(\tau)) \dot{x}(\tau) \mathrm{d}\tau. \tag{4.4}$$

While a change in the system entropy is completely determined by the initial and final configuration, the entropy change in the medium depends on the complete trajectory $x(\tau)$. We denote such a functional dependence by square brackets around the argument.

The total entropy change along a trajectory is then given by the heat dissipated into the environment and an additional boundary term arising from the initial and final configurations of the system, see Eq. (4.1),

$$\Delta s_{\mathrm{tot}}[x(\tau)] \equiv \Delta s[x(\tau)] + \Delta s_{\mathrm{m}}[x(\tau)] = -\ln \left[\frac{\Psi(x(t), t)}{\Psi(x(0), 0)}\right] + \frac{1}{T} \int_0^t F(x(\tau)) \dot{x}(\tau) \mathrm{d}\tau. \tag{4.5}$$

In the following, we will understand that the entropy changes are trajectory-dependent and suppress the functional arguments.

4.3. Fluctuation theorems

At first glance, a highly disconcerting property of the total stochastic entropy is that it can be negative, seemingly in conflict with the second law of thermodynamics. In this context, one should keep in mind that just as work and heat, the total

entropy production is also a trajectory-dependent and thus fluctuating quantity. However, thermodynamics does not incorporate fluctuations and does therefore not make any statement about the value of single fluctuations. It merely demands the nonnegativity of the ensemble average of the total entropy production, i. e., $\langle \Delta s_{\mathrm{tot}} \rangle \geq 0$. In fact, the second law enters the world of fluctuating trajectories not only in the form of this averaged thermodynamic analog but also in another, refined way [54]. Specifically for NESSs, it fixes the ratio of the probability weight for positive and negative total entropy production along paths of arbitrary but constant duration Δt to [3]

$$p(\Delta s_{\mathrm{tot}})/p(-\Delta s_{\mathrm{tot}}) = \exp\{\Delta s_{\mathrm{tot}}/T\}. \tag{4.6}$$

Not only does this theorem allow for negative values of Δs_{tot}, it even implies and quantifies their existence. In particular, if a positive fluctuation Δs_{tot} occurs with finite probability, its negative counterpart must appear as well, albeit with an exponentially suppressed probability. From Eq. (4.6), we easily recover the second law in its familiar form. First, we solve for $p(-\Delta s_{\mathrm{tot}})$ and average over all realizations

$$\langle \exp\{-\Delta s_{\mathrm{tot}}/T\} \rangle = 1, \tag{4.7}$$

then we employ Jensen's inequality to obtain $\langle \Delta s_{\mathrm{tot}} \rangle \geq 0$.

Eqs. (4.6) and (4.7) belong to a large family of remarkable symmetry relations known as fluctuation theorems [3, 63–66]. FTs of various forms have been proved for deterministic and stochastic dynamics. For the former class, the proof rests on the *chaotic hypothesis*, time-reversibility, and a phase-space contraction associated with dissipation [64]. For the latter dynamics, the FT requires the concept of entropy production along trajectories as introduced in the preceding section. It can be proved for Markovian systems [3, 65, 66] and compatible experimental tests have been performed for driven colloidal particles [7, 67] and a harmonic oscillator coupled to a thermal bath [68]. Further experimental tests of FT-like symmetries have been reported for Rayleigh-Bénard convection [118], turbulent flow [119], granular matter [120], and self-propelled particles [121]. For these systems, the appropriate class of dynamics is less obvious and hence the status regarding the assumptions of the FT is unclear a priori. One should also appreciate that the measured observable for some of these systems is typically not Δs_{tot} directly, but rather some dimensionful quantity, like, e. g., the injected or dissipated work [120, 122].

In order to derive Eqs. (4.6) and (4.7), we follow Refs. [103, 123, 124] in the proof of a master FT for Langevin dynamics from which, among several other FTs, these two can be deduced.

4.3.1. Master FT

Generally speaking, fluctuation theorems are symmetry properties of functionals of the system trajectories under conjugation of the dynamics. A path-integral approach is ideally suited to approach this class of relations as it explicitly incorporates the trajectories of the complete set of the degrees of freedom in the system. Hence, it will be employed in the subsequent derivation. Although the following is in principle valid for several types of conjugation, we restrict ourselves to time reversal for simplicity. Moreover, we focus exclusively on steady states since we will need the FT only in connection with stationary systems. For a more general discussion, see Ref. [54].

We consider a trajectory $\mathcal{X} \equiv \{x(\tau)|\tau \in \mathcal{I}\}$ in a time interval $\mathcal{I}$ ending at a time t and denote the time reversed path as $\mathcal{X}^{\mathrm{c}} \equiv \{x^{\mathrm{c}}(\tau) = x(t-\tau)|\tau \in \mathcal{I}\}$. We define the functional

$$\mathcal{R}[\mathcal{X}] \equiv \ln\left[\frac{P[\mathcal{X}]}{P[\mathcal{X}^{\mathrm{c}}]}\right] = -\mathcal{R}[\mathcal{X}^{\mathrm{c}}] \tag{4.8}$$

and compute for an arbitrary function $g(\mathcal{R})$ the weighted average [103, 123, 125]

$$\begin{aligned}\left\langle g(\mathcal{R})e^{-\mathcal{R}}\right\rangle &= \int g(\mathcal{R}[\mathcal{X}])e^{-\mathcal{R}[\mathcal{X}]}P[\mathcal{X}]\mathrm{d}\mathcal{X} \\ &= \int g(\mathcal{R}[\mathcal{X}])P[\mathcal{X}^{\mathrm{c}}]\mathrm{d}\mathcal{X} \\ &= \int g(-\mathcal{R}[\mathcal{X}^{\mathrm{c}}])P[\mathcal{X}^{\mathrm{c}}]\mathrm{d}\mathcal{X}^{\mathrm{c}} = \langle g(-\mathcal{R})\rangle\,. \end{aligned} \tag{4.9}$$

In the second step, we used the definition of $\mathcal{R}$, see Eq. (4.8), and, in the last line, we have substituted $\mathcal{X}^{\mathrm{c}}$ for $\mathcal{X}$ keeping in mind that the set of integration paths remains unchanged under time reversal. Choosing $g(\mathcal{R}) = \delta(\mathcal{R}' - \mathcal{R})$ and $g(\mathcal{R}) = 1$ yields the detailed and the integral FTs

$$\frac{p(\mathcal{R}')}{p(-\mathcal{R}')} = e^{\mathcal{R}'} \tag{4.10}$$

and

$$\left\langle e^{-\mathcal{R}}\right\rangle = 1, \tag{4.11}$$

respectively, where we used that $\langle\delta(\mathcal{R}' - \mathcal{R})\rangle = p(\mathcal{R}')$. These equations are already of the form of Eqs. (4.6) and (4.7). However, the physical interpretation of $\mathcal{R}$ is not yet clear.

4.3.2. Physical interpretation

From a physical point of view, the relation derived in Eq. (4.9) becomes interesting only if one can provide the functional $\mathcal{R}[\mathcal{X}]$ with a physical meaning. The interpretation of $\mathcal{R}[\mathcal{X}]$ becomes obvious if we decompose the path weights in Eq. (4.8) into the stationary probability weight for their respective starting points, $\Psi^{\mathrm{s}}(x_0)$ and $\Psi^{\mathrm{s}}(x_0^{\mathrm{c}})$, and the conditional probability for their subsequent evolution

$$\mathcal{R}[\mathcal{X}] \equiv \ln\left[\frac{P[\mathcal{X}]}{P[\mathcal{X}^{\mathrm{c}}]}\right] = \underbrace{\ln\left[\frac{\Psi^{\mathrm{s}}(x_0)}{\Psi^{\mathrm{s}}(x_0^{\mathrm{c}})}\right]}_{\equiv\mathcal{R}_0} + \underbrace{\ln\left[\frac{P[\mathcal{X}|x_0]}{P[\mathcal{X}^{\mathrm{c}}|x_0^{\mathrm{c}}]}\right]}_{\equiv\mathcal{R}_1}. \tag{4.12}$$

The first summand is easily identified as the entropy change in the system

$$\mathcal{R}_0 = \ln\Psi^{\mathrm{s}}(x_0) - \ln\Psi^{\mathrm{s}}(x_0^{\mathrm{c}}) = -\ln\Psi^{\mathrm{s}}(x_f) + \ln\Psi^{\mathrm{s}}(x_0) \equiv \Delta s, \tag{4.13}$$

where the starting point of the time-reversed trajectory $x_0^{\mathrm{c}} = x_f$ is the endpoint of the original one. The second summand can be interpreted as well by employing the conditional path-weight for the evolution of a trajectory following overdamped Langevin dynamics. Using Eqs. (2.22) and (2.23) the term becomes

$$\mathcal{R}_1 = \mathcal{A}[\mathcal{X}^{\mathrm{c}}|x_0^{\mathrm{c}}] - \mathcal{A}[\mathcal{X}|x_0] = \frac{1}{T}\int_{\mathcal{I}} F(x(\tau))\dot{x}(\tau)\mathrm{d}\tau = \Delta s_{\mathrm{m}}, \tag{4.14}$$

i. e., the medium entropy produced along the path $\mathcal{X}$. Applying these results to Eq. (4.12) yields $\mathcal{R}[\mathcal{X}] = \Delta s_{\mathrm{tot}}$. Hence, the functional is equivalent to the total entropy produced along $\mathcal{X}$. With this result, Eqs. (4.10) and (4.11) turn into the detailed and the integral fluctuation theorem for the total entropy production given respectively in Eqs. (4.6) and (4.7).

4.4. Hidden degrees of freedom

The proof of the FT discussed in the previous section implicitly rests on a time-scale separation. Unobserved fast degrees of freedom contribute to an effectively white noise and lead thus to a Markovian dynamics of the visible slow degrees of freedom. Entropy production can be deduced from observing the dynamics of *all* slow degrees of freedom. If some of these degrees of freedom are not or cannot be observed, the inferred entropy production is only an apparent one for which the status of an FT-like symmetry is unclear a priori. Theoretical efforts to describe coarse-graining in general have been restricted, so far, to the case of well-separated time scales [126–128] and to the question how such coarse-graining affects bounds on dissipated work [129].

Here, we investigate the influence of such hidden slow degrees of freedom on the FT for the apparent entropy production. In order to put the subsequent discussion on a firm ground, we first need to elucidate what we mean precisely with "apparent" entropy production. Therefore, we dedicate the next subsection to clarifying which entropy production an experimentalist would infer from a reduced set of degrees of freedom if he were not aware of the missing ones.

4.4.1. Apparent entropy production

We consider a Langevin system in a NESS with n slow degrees of freedom collected in the configuration vector $\mathbf{x}(\tau) \equiv (x_1(\tau), \ldots, x_n(\tau))^{\mathrm{T}}$. The total entropy production along a trajectory in the time interval $\mathcal{I} = [0, t]$ is given by

$$\begin{aligned}\Delta s_{\mathrm{tot}} &= -\ln\left[\frac{\Psi^{\mathrm{s}}(\mathbf{x}(t))}{\Psi^{\mathrm{s}}(\mathbf{x}(0))}\right] + \int_0^t \sum_{i=1}^{n} \dot{x}_i(\tau) F_i(\mathbf{x}(\tau)) \mathrm{d}\tau / T \\ &= \int_0^t \sum_{i=1}^{n} \dot{x}(\tau) \nu_i^{\mathrm{s}}(\mathbf{x}(\tau)) \mathrm{d}\tau / D_0, \quad (4.15)\end{aligned}$$

where we used the stationary mean local velocities $\nu_i^{\mathrm{s}}(\mathbf{x}(\tau))$ given by Eq. (3.20) in the last step. Both the sum and the arguments of the mean local velocities involve all n degrees of freedom. If only the first $\tilde{n}$ coordinates, $\tilde{\mathbf{x}} \equiv (x_1, \ldots, x_{\tilde{n}})^{\mathrm{T}}$, can be accessed, an observer would be forced to deduce all information from the trajectories of this reduced set. For the accessible coordinates $\tilde{\mathbf{x}}$, one can still measure the actual velocities $\dot{\tilde{\mathbf{x}}}$ correctly. For the mean local velocities, however, the lack of knowledge changes the results to

$$\tilde{\nu}_i^{\mathrm{s}}(\tilde{\mathbf{x}}) \equiv \int \nu_i^{\mathrm{s}}(\mathbf{x}) p(\hat{\mathbf{x}}|\tilde{\mathbf{x}}) \mathrm{d}\hat{\mathbf{x}} \quad (4.16)$$

with the conditional probability $p(\hat{\mathbf{x}}|\tilde{\mathbf{x}})$ to find the set of hidden degrees of freedom $\hat{\mathbf{x}} \equiv (x_{\tilde{n}+1}, \ldots, x_n)^{\mathrm{T}}$ in this specific configuration for given $\tilde{\mathbf{x}}$. The apparent entropy production is therefore

$$\Delta \tilde{s}_{\mathrm{tot}} = \int_0^t \sum_{i=1}^{\tilde{n}} \dot{x}_i(\tau) \tilde{\nu}_i^{\mathrm{s}}(\tilde{\mathbf{x}}(\tau)) \mathrm{d}\tau / D_0. \quad (4.17)$$

In the following, we investigate the status of the FT in the presence of hidden degrees of freedom, i. e., if we substitute $\Delta \tilde{s}_{\mathrm{tot}}$ for Δs_{tot} in Eq. (4.6).

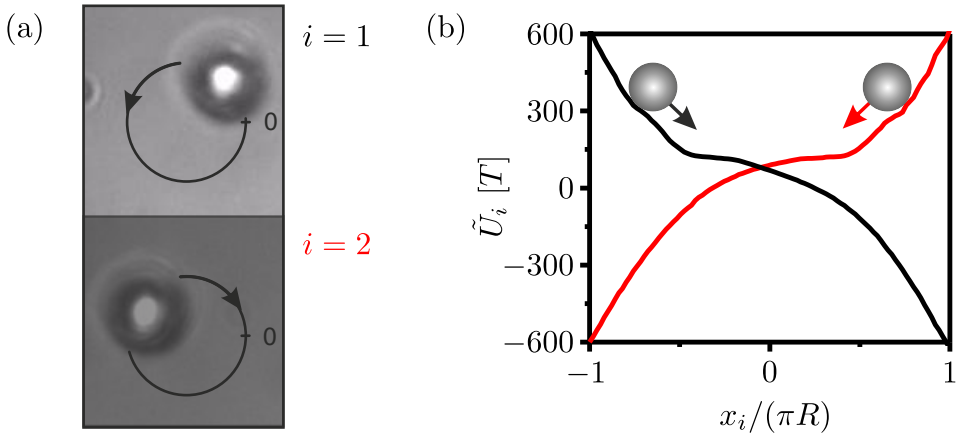

Figure 4.1.: (a) Snapshot of the experimental system augmented by a drawing of the rings to which the particles are confined. The second particle (shaded lower picture) is considered as the hidden degree of freedom. (b) Effective nonperiodic potentials for parameter set I in Table 4.1. Figure from Ref. [51].

4.4.2. Experimental results

We now turn to the experimentally accessible[1] system consisting of two magnetically coupled colloidal particles driven along two coplanar, nonoverlapping rings of radius R, see Fig. 4.1. This system has been already introduced in the previous chapter, see Fig. 3.3 for a schematic sketch. Its dynamics is given by the overdamped Langevin equation (2.5) with the forces defined in Eq. (3.31). Here, we prepare the system as follows. The particles are driven in opposite directions on their respective ring with equally strong driving forces on symmetrically adjusted potentials. The specific parameters are listed as set I in Table 4.1. In particular, the driving forces are so strong that there are no local minima left in the tilted potentials $\tilde{U}_i(x_i) \equiv A_i \sin(x_i/R - \phi_i) + f_i x_i$ on both rings, cf. Fig. 4.1(b). The phase shifts ϕ_i are adjusted such that the flattest parts of the $\tilde{U}_i(x_i)$ are near the position where the two rings are closest. In this NESS, we record the positions of the two particles as functions of time for coupling constants in the range $0 \leq \Gamma \leq 300$.

This setup provides a means to experimentally scrutinize the role of hidden slow degrees of freedom in the FT for the total entropy production. In the following, we evaluate $\Delta\tilde{s}_{\mathrm{tot}}$, the apparent entropy produced by the first particle only, which represents the accessible degree of freedom. Meanwhile, the second particle acts as a hidden degree of freedom with the coupling constant Γ controlling the strength of its influence, cf. Fig. 4.1(a).

[1] Experiments have been performed by J. Mehl.

	I	II
f_1 [T/μm]	57	57
f_2 [T/μm]	−57	−57
A_1 [T]	181	262
A_2 [T]	181	71
R [μm]	3.5	3.5
center-center distance [μm]	17	17

Table 4.1.: Parameter sets I and II. Note that the phase shifts ϕ_i can be estimated only roughly and are therefore not listed here. They are adjusted such that they fall into the region where the particles are closest.

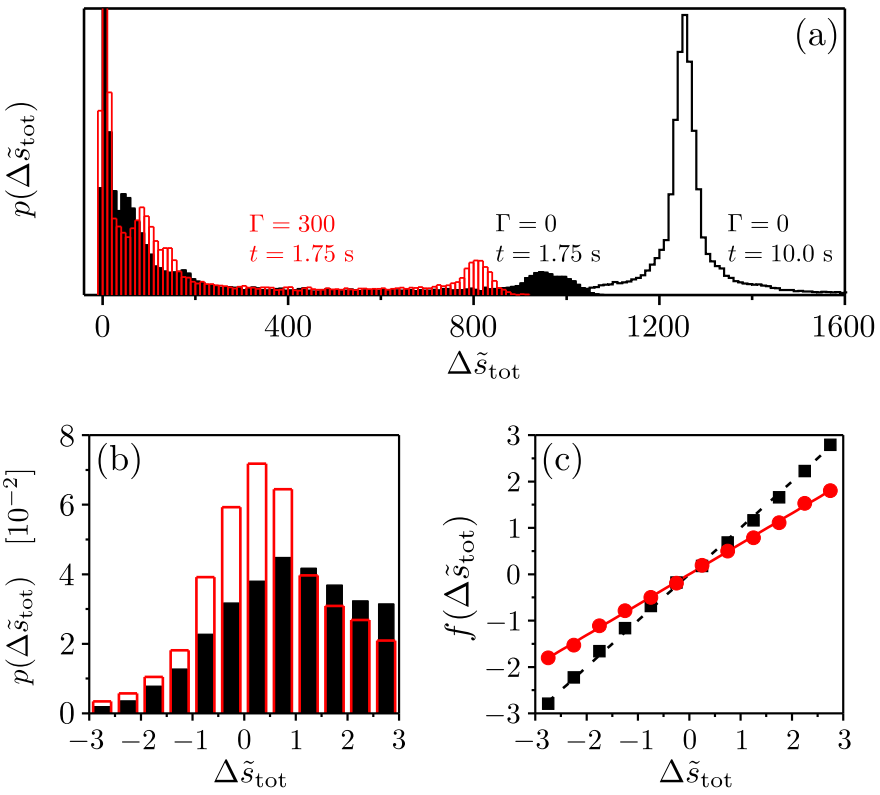

Figure 4.2.: (a) Distribution of the apparent entropy production $p(\tilde{s}_{\mathrm{tot}})$ for different trajectory lengths t and coupling constants Γ. (b) Section of previous histograms around $\tilde{s}_{\mathrm{tot}} = 0$. (c) Corresponding logarithmic probability ratio $f(\Delta\tilde{s}_{\mathrm{tot}})$ as a function of $\Delta\tilde{s}_{\mathrm{tot}}$. The dashed black line has the theoretically predicted slope 1, whereas the red line is a linear fit with slope $\alpha = 0.65$.

Entropy production without coupling

First, we discuss the pdf of the apparent entropy produced along trajectories of duration $t = 1.75$ s and 10 s in the absence of coupling, see Fig. 4.2(a). Note that for $\Gamma = 0$, the two particles become independent and $\Delta\tilde{s}_{\mathrm{tot}}$ is equivalent to the total entropy production of a single particle system. The distribution for $\Delta\tilde{s}_{\mathrm{tot}}$ is characterized by peaks of strongly varying magnitude. For $t = 1.75$ s, we find the largest peak close to zero at small positive $\Delta\tilde{s}_{\mathrm{tot}}$. This contribution is caused by fluctuations in the flat part of $\tilde{U}$ producing only little entropy. The second peak at $\Delta\tilde{s}_{\mathrm{tot}} \simeq 950$ belongs to trajectory segments in which the particle is moving rapidly down the steep part of $\tilde{U}$. For longer trajectories, the probability for larger $\Delta\tilde{s}_{\mathrm{tot}}$ increases and the corresponding distribution shifts to higher $\Delta\tilde{s}_{\mathrm{tot}}$. If the duration of the trajectory segments matches the average time $t \simeq 10$ s of a revolution, the probability that a complete round-trip takes place in such a time segment is very high. Hence, we have a large peak at entropy productions associated with heat transfer for a full revolution $\Delta\tilde{s}_{\mathrm{tot}} \simeq 2\pi R f_1 = 1250$. An experimental check of the FT, or equivalently the determination of the function

$$f(\Delta\tilde{s}_{\mathrm{tot}}) \equiv \ln\left[p(\Delta\tilde{s}_{\mathrm{tot}})/p(-\Delta\tilde{s}_{\mathrm{tot}})\right], \tag{4.18}$$

requires the accurate measurement of events with both entropy productions $\Delta\tilde{s}_{\mathrm{tot}}$ and $-\Delta\tilde{s}_{\mathrm{tot}}$. As trajectory segments with negative entropy production become increasingly rare with both growing t and $\Delta\tilde{s}_{\mathrm{tot}}$, the trajectory length is limited by $t \lesssim 2$ s and the range of f restricted to $-3 \lesssim \Delta\tilde{s}_{\mathrm{tot}} \lesssim 3$. Fig. 4.2(b) magnifies the section of the black histogram (closed bars) from Fig. 4.2(a) around $\Delta\tilde{s}_{\mathrm{tot}} = 0$. The excellent agreement between $f(\Delta\tilde{s}_{\mathrm{tot}})$, black squares in Fig. 4.2(c), and the straight black dashed line with slope one crossing the origin expectedly confirms the validity of the FT (4.6) for one ring in the uncoupled case.

Approximate FT-like symmetry for $\Gamma \neq 0$

The red histograms (open bars) in Figs. 4.2(a) and (b) demonstrate the situation for coupled particles. Most prominent is the change in the structure of the pdf in the range $0 \lesssim \Delta\tilde{s}_{\mathrm{tot}} \lesssim 200$. While for the maximum at $\Delta\tilde{s}_{\mathrm{tot}} \simeq 0$ the probability density is enhanced, it passes through a local minimum for slightly larger $\Delta\tilde{s}_{\mathrm{tot}}$ before we observe another local maximum at $\Delta\tilde{s}_{\mathrm{tot}} \simeq 100$. The peak around $\Delta\tilde{s}_{\mathrm{tot}} = 800$ is shifted towards lower entropy productions due to the slower average velocities of the particle for this Γ. Since the red dots in Fig. 4.2(c) do not agree with the dashed line of slope one, this apparent entropy production does not obey the FT. Surprisingly, we still find a linear relation

$$f(\Delta\tilde{s}_{\mathrm{tot}}) \simeq \sigma\Delta\tilde{s}_{\mathrm{tot}} \tag{4.19}$$

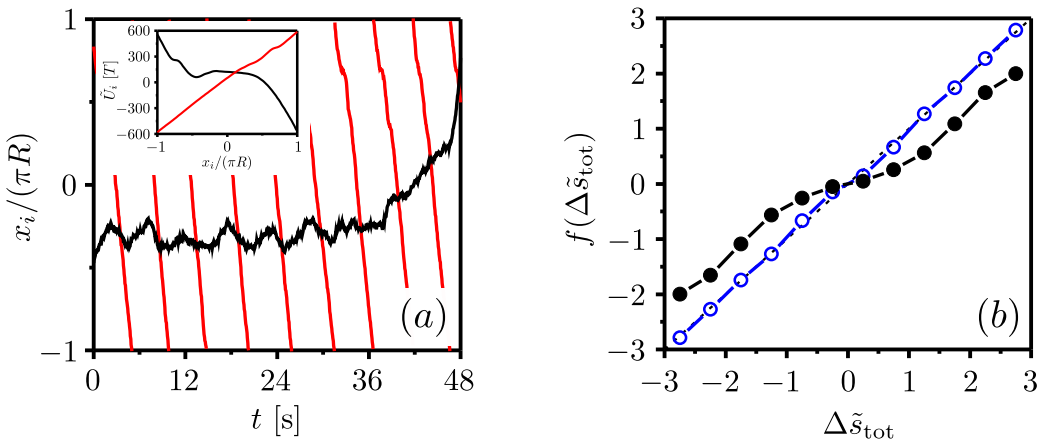

Figure 4.3.: (a) Typical trajectories of the observed (black line) and hidden particle (red line) for parameter set *II* in Table 4.1 and coupling constant $\Gamma = 380$. Inset: Corresponding tilted potentials for the observed (black line) and the hidden (red line) particle. (b) Logarithmic probability ratio f as a function of $\Delta\tilde{s}_{\rm tot}$ for $t = 3$ s (black) and 0.25 s (blue). Figure from [51].

within the experimental error margins with a slope $\sigma \simeq 0.65$ deviating significantly from one. We find such linear functions for various coupling strengths albeit with different slopes. One might speculate that this behavior results from the symmetric choice of parameters employed here. However, such linear relations appear as well in additional measurements performed for asymmetric configurations. Hence, we exclude geometrical symmetry in the setup as the sole origin of this behavior.

Deviations from linearity

Despite all this experimental evidence, it would be very surprising if this result was a strict relation. However, if this results holds only approximately, we should be able to find parameters for which deviations become visible. Indeed, we observe an obviously nonlinear result by fine-tuning the parameters, see Fig. 4.3(b). In this special case, the coupling constant is set to $\Gamma = 380$ and two particles are subjected to quite different potentials, while the driving forces remain unchanged, cf. parameter set *II* in Table 4.1. Specifically, the potential of the hidden particle is adjusted such that it moves along the ring almost freely. By contrast, for the observed particle, a deep minimum remains in the tilted potential $\tilde{U}_1(x_1)$ which the particle is not able to leave on its own. A complete revolution can only be observed when the hidden particle pushes the observed one over the barrier. We elucidate this pattern of motion by means of a typical trajectory shown in Fig. 4.3(a). The hidden particle (red line) moves with a period of 4 s at an almost constant velocity

along $\tilde{U}_2(x_2)$. Only around $x_2 = 0.75$, the repulsive interaction ($\Gamma = 380$) causes it to slow down somewhat. By contrast, the observed particle (black line) is not moving quickly but fluctuating at low mean local velocities around a potential minimum at $x_1 = -0.35$. In addition, we find oscillations whose characteristic frequency matches the revolution frequency of the hidden particle, see Fig. 4.3(b). These oscillations arise due to the following mechanism. Each time the hidden particle traverses the region close to the neighboring ring, it pushes the observed particle up the potential hill towards positive x_1. In most cases, however, the push is not strong enough for the observed particle to overcome the barrier. Hence, once the hidden particle has passed by, the observed one relaxes into the potential minimum again. The process repeats itself as soon as the hidden particle returns. These oscillations enhance the probability for the occurrence of events with the apparent entropy productions corresponding to the up and downhill sections of the oscillating trajectories. The entailing changes in $p(\Delta\tilde{s}_{\mathrm{tot}})$, in turn, cause the deviations from a linear $f(\Delta\tilde{s}_{\mathrm{tot}})$.

Discussion

So far, we have worked out that relation Eq. (4.19) is not an exact law but rather a good approximation for many cases. In order to explain this result, we discuss the logarithmic probability ratio $f(\Delta\tilde{s}_{\mathrm{tot}})$ [Eq. (4.18)] in more detail. First, we note that $f(\Delta\tilde{s}_{\mathrm{tot}})$ is antisymmetric by construction. For small entropy productions, $\Delta\tilde{s}_{\mathrm{tot}} \ll 1$, $f(\Delta\tilde{s}_{\mathrm{tot}})$ must therefore be linear up to corrections of third order or higher [130]. Second, we discuss $f(\Delta\tilde{s}_{\mathrm{tot}})$ for large entropy productions, $\Delta\tilde{s}_{\mathrm{tot}} \gg 1$. Solving Eq. (4.18) for $p(-\Delta\tilde{s}_{\mathrm{tot}})$ and integrating over all $\Delta\tilde{s}_{\mathrm{tot}}$ yields

$$\int_{-\infty}^{+\infty} p(\Delta\tilde{s}_{\mathrm{tot}})\, e^{-f(\Delta\tilde{s}_{\mathrm{tot}})}\, \mathrm{d}\Delta\tilde{s}_{\mathrm{tot}} = 1 \tag{4.20}$$

by normalization. We assume that $p(\Delta\tilde{s}_{\mathrm{tot}})$ does not decay faster than a Gaussian. We have observed this property in all measurements and expect the assumption to be rather weak because for any quantity consisting of independent contributions, the central limit theorem would imply a Gaussian. Any correlation would typically lead to a slower decay. Under this assumption, convergence of the integral in Eq. (4.20) requires that $f(\Delta\tilde{s}_{\mathrm{tot}}) = \mathcal{O}(\Delta\tilde{s}_{\mathrm{tot}}^2)$. Since, in addition, $f(\Delta\tilde{s}_{\mathrm{tot}})$ is antisymmetric, we expect the generic asymptotic behavior to be linear, $f(\Delta\tilde{s}_{\mathrm{tot}}) \sim \Delta\tilde{s}_{\mathrm{tot}}$, with a slope in general different from the one for small $\Delta\tilde{s}_{\mathrm{tot}}$. We emphasize that this reasoning does not prove the linearity of f in the limit of large $\Delta\tilde{s}_{\mathrm{tot}}$, rather it provides an argument why such a behavior can be considered as typical. In summary, we expect a linear function both for small and for large entropy production for any time t. This reasoning leaves the possibility for a nonlinear regime for intermediate t.

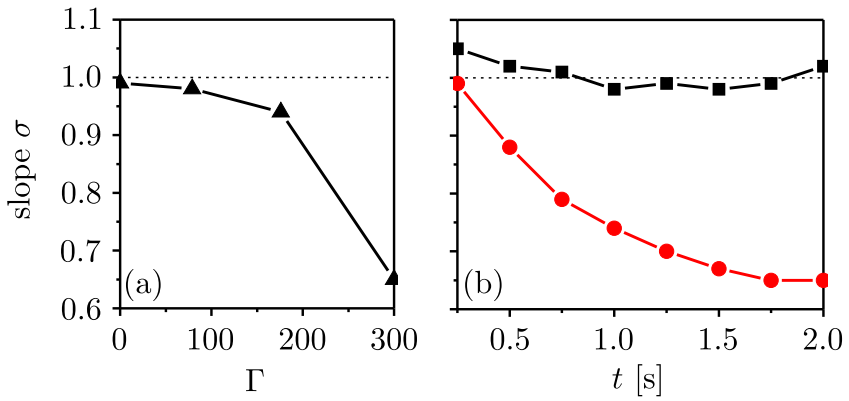

Figure 4.4.: (a) Slope σ vs. coupling constant Γ for $t = 1.75$ s. (b) Slope σ for different trajectory lengths t for $\Gamma = 0$ (black squares) and $\Gamma = 300$ (red dots). The deviation of the black squares from $\sigma = 1$ is in the order of the statistical error.

4.4.3. Slope in dependence of the trajectory length

For parameter set I in Table 4.1, we observe approximately linear relations of the form of Eq. (4.19) for all accessible coupling strengths and trajectory lengths. Still, the slope varies as a function of both parameters, see Figs. 4.4. The dependence of σ on Γ is a manifestation of the transition from an uncoupled to a coupled state. Considering the dependence of σ on t in the uncoupled case, we expectedly find the FT confirmed for arbitrary t, see black squares in Fig. 4.4(b). Increasing the coupling constant to $\Gamma = 300$, the slope deviates from one with its value depending on t. An intriguing feature is that in the limit of short trajectories, the slope approaches one and hence fulfills the FT in this limit. We observe a similar behavior for the nonlinear f shown in Fig. 4.3(b). Here, the nonlinear f for finite t becomes a linear function with slope one in the short-time limit. In the following, we show that this behavior is a generic feature of the apparent entropy production.

Slope in the short-time limit

The origin of the FT for the apparent entropy production approaching the exact FT in the short-time limit is that for very short trajectories $\Delta\tilde{s}_{\mathrm{tot}}$ becomes equivalent to the total entropy production of an effective one-particle system which trivially obeys the FT. This equivalence comes to light in a short-time expansion of $\Delta\tilde{s}_{\mathrm{tot}}$. For such an expansion, it is crucial to appreciate the stochastic nature of the underlying dynamics. Therefore, we write the dynamics in terms of the Îto process [11]

$$\mathrm{d}x_i(t) = (2D_0)^{1/2}\mathrm{d}w_i(t) + \mu_0 F_i(\mathbf{x})\mathrm{d}t \tag{4.21}$$

with the Wiener process $w_i(t) \equiv \int_0^t \mathrm{d}w(t)$ starting at $w_i(0) = 0$. The Wiener process is defined by the differential increments $\mathrm{d}w_i(t)$ which follow a Gaussian distribution with zero mean and variance $\mathrm{d}t$ at any time t. In particular, we have

$$\langle \mathrm{d}w_i(t)\mathrm{d}w_j(t)\rangle = \delta_{ij}\,\mathrm{d}t. \tag{4.22}$$

Regarding the short-time limit, an important consequence of this relation is that $\mathrm{d}w_i^2(t)$ [not $\mathrm{d}w(t)$] is of the order $\mathrm{d}t$, i. e., $\mathrm{d}w_i^2 = \mathcal{O}(\mathrm{d}t)$ [11].

The apparent entropy production for the ith accessible degree of freedom is given by the Riemann-Stieltjes integral [116]

$$\Delta\tilde{s}_{\mathrm{tot}} = \int_0^t \tilde{\nu}_i^{\mathrm{s}}(x_i(t))\mathrm{d}x_i(t) = \int_0^t \tilde{\nu}_i^{\mathrm{s}}(x_i(t))\circ\mathrm{d}x_i(t) + \frac{1}{2}\int_0^t \partial_{x_i}\tilde{\nu}_i^{\mathrm{s}}(x_i(t))\mathrm{d}t. \tag{4.23}$$

In the last step, we express the Stratonovich integral as the sum of an Îto integral denoted by $\circ$ and an additional deterministic drift term. The short-time expansion of the latter is straightforward while the expansion of the Îto integral is somewhat more subtle due to the short-time behavior of $w(t)$, see Eq. (4.22). With Eq. (4.21) we obtain

$$\begin{aligned}\Delta\tilde{s}_{\mathrm{tot}} = &\underbrace{\tilde{\nu}_i^{\mathrm{s}}(x_i^0)w_i(t)}_{\mathcal{O}\left(t^{1/2}\right)} \\ &+ \underbrace{\left.\frac{\partial\tilde{\nu}_i^{\mathrm{s}}}{\partial x_i}\right|_{x_i=x_i^0} w_i^2(t) + \left(\tilde{\nu}_i^{\mathrm{s}}(x_i^0)\mu_0 F_i(\mathbf{x}^0) + \frac{1}{2}\left.\frac{\partial\tilde{\nu}_i^{\mathrm{s}}}{\partial x_i}\right|_{x_i=x_i^0}\right)t}_{\mathcal{O}(t)} + \mathcal{O}\left(t^{3/2}\right),\end{aligned} \tag{4.24}$$

where $x_i^0 \equiv x_i(0)$, $\mathbf{x}^0 \equiv \mathbf{x}(0)$, and $w_i(t) \equiv \int_0^t dw_i(\tau)$. Analogously, the short-time expansion of the total entropy production in a system consisting of only one degree of freedom i reads

$$\begin{aligned}\Delta s_{\mathrm{tot}} = &\underbrace{\nu_i^{\mathrm{s}}(x_i^0)w_i(t)}_{\mathcal{O}\left(t^{1/2}\right)} \\ &+ \underbrace{\left.\frac{\partial\nu^{\mathrm{s}}}{\partial x_i}\right|_{x_i=x_i^0} w_i^2(t) + \left(\nu_i^{\mathrm{s}}(x_i^0)\mu_0 F_i(x_i^0) + \frac{1}{2}\left.\frac{\partial\nu_i^{\mathrm{s}}}{\partial x_i}\right|_{x_i=x_i^0}\right)t}_{\mathcal{O}(t)} + \mathcal{O}\left(t^{3/2}\right).\end{aligned} \tag{4.25}$$

Comparing Eqs. (4.24) and (4.25) up to $\mathcal{O}\left(t^{1/2}\right)$, we find that the apparent entropy production is equivalent to the total entropy production of an effective one-particle

system subject to a Markovian dynamics with mean local velocity $\tilde{\nu}_i^s$. This system trivially fulfills the FT. Already for $\mathcal{O}(t)$, not all contributions can be attributed to the same dynamics anymore. More specifically, the forces $F_i(\mathbf{x}^0)$ and the apparent mean local velocity $\tilde{\nu}_i^s(x_i^0)$ are not compatible in this sense. Hence, the FT must hold in the short-time limit, and deviations can occur already in first order in time consistent with the experimental observation shown in Fig. 4.4(b). There, we find deviations of from $\sigma = 1$ around $t = 0$ in first order of t.

4.5. Conclusion and outlook

In this chapter, we have discussed the influence of a hidden degree of freedom on the entropy production for a paradigmatic two-particle system. In particular, we have scrutinized the apparent entropy one would infer from the trajectory of only one of the particles. Surprisingly, this apparent entropy production still obeys an approximate FT-like symmetry in many cases, albeit with a slope different from one. Consequently, in any experiment in which hidden degrees of freedom cannot be ruled out a priori, an observed linear behavior in an FT-like relation cannot be used to extract information by implicitly assuming $\sigma = 1$. Moreover, we have discussed why such an approximate FT-like symmetry is typical. First, in the limit of very short trajectories, we showed that an FT-like symmetry with the correct slope must hold. Second, for large entropy productions a simple argument restricts an increase in $f(\Delta\tilde{s}_{\mathrm{tot}})$ to $\mathcal{O}(\Delta\tilde{s}_{\mathrm{tot}}^2)$. Combined with the antisymmetry of $f(\Delta\tilde{s}_{\mathrm{tot}})$ a linear asymptote seems natural. Also, for small $\Delta\tilde{s}_{\mathrm{tot}}$, the antisymmetry of $f(\Delta\tilde{s}_{\mathrm{tot}})$ ensures that deviations from linearity can only be found in third order of $\Delta\tilde{s}_{\mathrm{tot}}$ or higher.

For a deeper understanding analytic expressions would be desirable. At least in the large-deviation limit such expressions can be obtained for harmonic systems [131, 132]. Investigating, e. g., a harmonic dumbbell bound to the origin at one end by a harmonic potential driven to nonequilibrium by a linear shear flow could sharpen the asymptotic argument for large entropy productions. Moreover, one could exchange the linear shear flow by a different source of driving and investigate the influence of the type of NESS. A further prospect is the investigation of nonstationary fluctuation theorems such as the Crooks fluctuation theorem [70] as analytic asymptotic expressions for work distributions are within reach too [133]. An analytically tractable system does also provide a means to study the influence of a hidden slow degree of freedom on other relations such as the fluctuation-dissipation theorem.

Finally, it would be interesting to search for quantities fulfilling exact fluctuation relations even if only a reduced set of degrees of freedom is accessible. Recently, a first step in this direction has been taken by Kawaguchi and Nakayama [134], who

proved an integral fluctuation theorem for a type of a hidden entropy production in a Markovian system.

5. Fluctuation-dissipation theorem in a sheared colloidal suspension

5.1. Introduction

The main virtue of equilibrium statistical mechanics is that even highly complex systems, consisting of a large number of interacting degrees of freedom, can be described by a small set of thermodynamic variables such as temperature or pressure. Once we abandon the restriction to thermal equilibrium, these quantities loose their validity. Therefore, an extension of such concepts to nonequilibrium systems would be highly desirable in order to develop a general and comprehensive treatment of systems far from equilibrium. In particular, much work has been dedicated to the search for simple quantities characterizing nonequilibrium systems in the spirit of a temperature [17, 87].

The measurement of a physically significant effective temperature in nonequilibrium should yield a unique value independent of the type of thermometer employed. From a microscopic point of view, a thermometer works by equilibrating the average energy of its own degrees of freedom with that of the fluctuations in the system. In order to probe the thermal fluctuations, the thermometer needs to be coupled to the system, constituting a small perturbation in the process [135]. While the reaction of the system to this perturbation is described by a linear response function, the system's fluctuations are quantified by correlation functions. To which temperature the thermometer relaxes is determined by the ratio of these correlation and response functions, i. e., by the so-called fluctuation-dissipation ratio (FDR). In equilibrium, the fluctuation-dissipation theorem (FDT) ensures that the FDR equals the thermal energy for any time scale and any choice of corresponding correlation and response functions. Hence, every thermometer relaxes to the same, unique equilibrium temperature.

Since even in a NESS one can define and measure correlation and response functions [136–139], it is tempting to introduce an effective temperature for stationary nonequilibrium through such an FDR. However, it has recently been shown that for Markovian systems in NESSs coupled to a heat bath of well-defined temperature

T the FDT should be interpreted in terms of an additive correlation rather than in the form of a multiplicative factor as implied by such an effective temperature concept [18–21, 140–142]. Nevertheless, for the purpose of a simple description, we might still be interested in defining an approximate temperature through the FDR. This strategy was originally proposed in the context of aging mean-field spin systems [17, 87] and has subsequently been applied to various other systems [88–90]. In particular, in a sheared colloidal suspension or fluid the Einstein relation between the diffusion coefficient of a tagged particle and its mobility is broken and was used to define an effective temperature [24, 27, 143–146].

In the following, we will briefly introduce the FDT in equilibrium and show how it can be extended to NESSs along the lines of Ref. [20]. We will examine the FDR and its usefulness as an effective temperature for a sheared colloidal suspension by following the trajectory of a tagged particle, i. e., a randomly chosen particle out of many identical, interacting particles. Motivated by the physical picture of an effective confinement in dense systems, we also consider a single trapped colloidal particle in shear flow [147]. In particular, we discuss the FDT in a "hybrid" form in which we relate response and correlations through the kinetic temperature in the spirit of an effective temperature, but with an additive correction term still present. For the trapped particle, expressions can be obtained analytically while, for the tagged particle, we derive a similar FDT exploiting a time scale separation due to the effective confinement. In both cases, we show that the correction term indeed becomes negligible for strong confinement [26]. Finally, we investigate the implications of this result for the mobility and the diffusion coefficient of the tagged particle in the suspension. Specifically, we find an approximate Einstein relation in the regime in which the correction term is negligible [27].

5.2. FDT in equilibrium

If we apply a time-dependent external perturbation to an equilibrium system, the mean value of an arbitrary observable A will change in general. In particular, for a sufficiently small perturbation, the average of A at time t is given by the expansion

$$\langle A(t)\rangle_{\mathrm{eq}}^{h} = \langle A\rangle_{\mathrm{eq}} + \int_{-\infty}^{t} R_{A,h}^{\mathrm{eq}}(t-t')h(t')\mathrm{d}t' + \mathcal{O}\big(h^2\big)\,, \tag{5.1}$$

where we distinguish the ensemble average in equilibrium $\langle\cdot\rangle_{\mathrm{eq}}$ and in a system perturbed by h in the linear response regime around equilibrium $\langle\cdot\rangle_{\mathrm{eq}}^{h}$. The linear response at time t to a perturbation at an earlier time $t' \leq t$ is defined by the

functional derivative

$$R^{\mathrm{eq}}_{A,h}(t-t') \equiv \left.\frac{\delta \langle A(t)\rangle^{h}_{\mathrm{eq}}}{\delta h(t')}\right|_{h=0} . \tag{5.2}$$

This response function is related to the equilibrium correlation function

$$C^{\mathrm{eq}}_{A,h}(t-t') \equiv \langle A(t) B^{\mathrm{eq}}(t')\rangle_{\mathrm{eq}} \tag{5.3}$$

by the fluctuation-dissipation theorem

$$T R^{\mathrm{eq}}_{A,h}(\tau) = C^{\mathrm{eq}}_{A,h}(\tau) \quad \text{for} \quad \tau \geq 0, \tag{5.4}$$

see, e. g., Refs. [81, 148]. Note that in any stationary state both the response and the correlation functions are translationally invariant in time and thus only dependent on the time difference $\tau \equiv t - t'$. The second observable in the correlation function (5.3) is conjugated to the perturbation h in the sense that

$$B^{\mathrm{eq}} \equiv -\partial_t [\partial_h U]_{h=0}, \tag{5.5}$$

i. e., B^{eq} is equivalent to the negative time-derivative of the change in the internal energy U for a variation in the perturbation h. The FDT (5.4) implies that the equilibrium fluctuation-dissipation ratio,

$$X^{\mathrm{eq}}_{A,h}(\tau) \equiv \frac{C^{\mathrm{eq}}_{A,h}(\tau)}{R^{\mathrm{eq}}_{A,h}(\tau)} = T, \tag{5.6}$$

is equivalent to the temperature, regardless of the time difference $\tau \geq 0$ and the choice of A or h.

The physical picture behind the FDT is condensed in Onsager's regression hypothesis which states that "as far as the average behavior is concerned, it does not matter whether a state was the result of a spontaneous fluctuation or of an imposed constraint" [149]. For a Gaussian process this hypothesis is equivalent to the Markovian assumption, which becomes obvious by restating it in the following way: "The system does not remember how it got to the given state." [149]

For practical purposes, the relevance of the FDT is twofold. On the one hand, one can obtain the linear response of a system to a perturbation simply by observing equilibrium fluctuations, i. e., without the need to actually apply a perturbation. On the other hand, one can gain information about microscopic fluctuations already from macroscopic linear response coefficients.

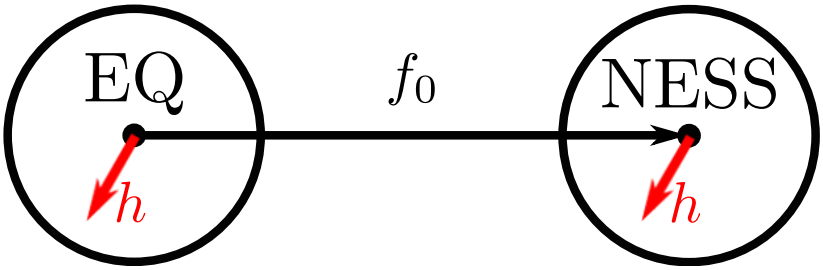

Figure 5.1.: Schematic sketch of the linear response regime of a system in equilibrium and a system driven into a NESS by f_0. The red arrows depict small perturbations applied in the stationary states.

5.3. Extended FDT in a NESS

The FDT, in the form of Eq. (5.4), is valid only in the proximity of equilibrium. Upon leaving the linear response regime, this relation breaks down. Still, analogous to equilibrium, a linear response regime around a NESS can be defined as well, see Fig. 5.1. Likewise, the evaluation of correlation functions in a NESS is unproblematic. Therefore, we can generalize Eqs. (5.2) and (5.3) to

$$R_{A,h}(t-t') \equiv \left.\frac{\delta \langle A(t)\rangle^h}{\delta h(t')}\right|_{h=0}, \quad \text{for} \quad t \geq t', \tag{5.7}$$

and

$$C_{A,h}(t-t') \equiv \langle A(t)B(t')\rangle\,, \tag{5.8}$$

respectively, where we have replaced the equilibrium ensemble averages with ensemble averages in an arbitrary steady state. Using stochastic thermodynamics, the extension of the FDT to NESSs takes the form [20]

$$TR_{A,h}(t-t') = \left\langle A(t)B^{\mathrm{NESS}}(t')\right\rangle, \quad \text{for} \quad t \geq t', \tag{5.9}$$

with the conjugate quantity

$$B^{\mathrm{NESS}} \equiv -T\partial_h \dot{s}, \tag{5.10}$$

in which the role of the internal energy is now played by the stochastic entropy. The connection to the equilibrium FDT is easily seen for systems relaxing to an equilibrium state with the pdf

$$\Psi_h(x) = \exp\left\{-[U(x,h) - \mathcal{F}(h)]/T\right\} \tag{5.11}$$

even for small nonvanishing perturbations h with the perturbation-dependent free energy of the system. Since, in contrast to the internal energy, the free energy $\mathcal{F}$ of the system does not depend on the configuration x, the free energy is constant along any trajectory. Hence, its time derivative is zero. Using the definition of the stochastic entropy (4.1), the conjugate quantity (5.10) reduces to the equilibrium result [20]

$$B^{\mathrm{NESS}} \overset{\mathrm{eq}}{=} \partial_t \partial_h [U(x,h) - \mathcal{F}(h)] = \partial_t \partial_h U(x,h) = B^{\mathrm{eq}}. \tag{5.12}$$

The general structure of the FDT in NESSs becomes most transparent, when we split the entropy production of the system into the total and the medium entropy production,

$$\begin{aligned} R_{A,h}(t-t') = \langle A(t)[\partial_h \dot{s}_{\mathrm{med}}]_{h=0}(t')\rangle - \langle A(t)[\partial_h \dot{s}_{\mathrm{tot}}]_{h=0}(t')\rangle \\ \equiv C_{A,h}(t-t') - I_{A,h}(t-t'), \end{aligned} \tag{5.13}$$

see Eq. (4.5). The FDT is now of an additive form involving two terms, the first of which, C, can be shown to correspond to the equilibrium form of the FDT evaluated in a NESS [20]. The second term is the time dependent excess function I caused by the total entropy production. This term vanishes along with $\dot{s}_{\mathrm{tot}}$ if we approach equilibrium. With this additive form in mind, there is no reason why the equivalent of the equilibrium FDR (5.6) evaluated in the NESS,

$$X_{A,h}(\tau) \equiv \frac{C_{A,h}(\tau)}{R_{A,h}(\tau)}, \tag{5.14}$$

should be time independent. Yet, in the next sections, we will see that there are conditions under which this FDR becomes approximately constant.

5.4. Effective confinement as the origin of a time-independent FDR

In the following, we will examine the FDR in a NESS for a single particle moving in a viscous liquid at temperature T. For the remainder of this chapter, we employ dimensionless units and measure lengths in units of the particle diameter a, energy in units of T, and time in units of the diffusive time scale $\tau_{\mathrm{D}} \equiv a^2/D_0$. In these units, the reduced mass of the particle m relates the momentum relaxation time to the diffusive time scale. The motion of the particle is described by the Langevin equations $\dot{\mathbf{r}} = \mathbf{v}$ and

$$m\dot{\mathbf{v}} = -\boldsymbol{\nabla} U + \mathbf{f} - [\mathbf{v} - \mathbf{u}(\mathbf{r})] + \boldsymbol{\xi}, \tag{5.15}$$

cf. Eq. (2.1), with stochastic forces of zero mean and correlations given by Eq. (2.2). The particle is subject to an externally imposed shear flow $\mathbf{u}(\mathbf{r}) = \dot{\gamma} y \mathbf{e}_x$ pointing in x direction with its magnitude increasing linearly with the y coordinate. In this set of units, the strain rate $\dot{\gamma}$ is equivalent to the Péclet number relating the time scales of convection and diffusion. We leave the potential U arbitrary, for now, but will pick two specific realizations in the following subsections. The small, externally applied forces $\mathbf{f}(t) \equiv (f_1(t), f_2(t), f_3(t))^{\mathrm{T}}$ with $f_i(t) = 0$ for $t < 0$ give rise to an evolution of the mean velocity according to

$$\langle \mathbf{v}(t) \rangle^{\mathbf{f}} = \int_0^t \mathsf{R}(t - t') \mathbf{f}(t') \mathrm{d}t' + \mathcal{O}\big(\mathbf{f}^2\big) \,, \tag{5.16}$$

where R is the response matrix with the components

$$R_{ij}(t - t') \equiv \left. \frac{\delta \langle v_i(t) \rangle^{\mathbf{f}}}{\delta f_j(t')} \right|_{\mathbf{f}=0} . \tag{5.17}$$

Here and for the remainder of this chapter, we implicitly assume $A \equiv \mathbf{v}$ and $h \equiv \mathbf{f}$ for the choice of observable and perturbation. In equilibrium, the response matrix is equal to the velocity autocorrelation matrix C with the components

$$C_{ij}(t - t') \equiv \langle v_i(t) v_j(t') \rangle \,. \tag{5.18}$$

We denote the corresponding FDR for the diagonal components as

$$X_i(\tau) \equiv \frac{C_{ii}(\tau)}{R_{ii}(\tau)}, \tag{5.19}$$

cf. Eq. (5.14). For $X_i(0)$, we can obtain an analytical result by performing a short-time expansion of Eq. (5.16) leading to

$$\langle \mathbf{v} \rangle^{\mathbf{f}} \approx \mathsf{R}(0) \mathbf{f}(0) \Delta t. \tag{5.20}$$

In the short-time limit, we get from the Langevin equation (5.15)

$$m \langle \dot{\mathbf{v}} \rangle^{\mathbf{f}} \approx m \langle \mathbf{v} \rangle^{\mathbf{f}} / \Delta t = \mathbf{f}(0). \tag{5.21}$$

Besides the zero mean of the stochastic forces, we have exploited that the velocities of the particles fluctuate symmetrically around the local solvent velocity and therefore $\langle \mathbf{v} - \mathbf{u}(\mathbf{r}) \rangle = 0$. Moreover, we have used that the conservative force vanishes on average, $\langle -\boldsymbol{\nabla} U \rangle = 0$. This assertion holds for any isotropic system and is still valid in linear shear flow which preserves the inversion symmetry about the origin. Hence, Eqs. (5.20) and (5.21) imply

$$R_{ij}(0) = \delta_{ij}/m, \tag{5.22}$$

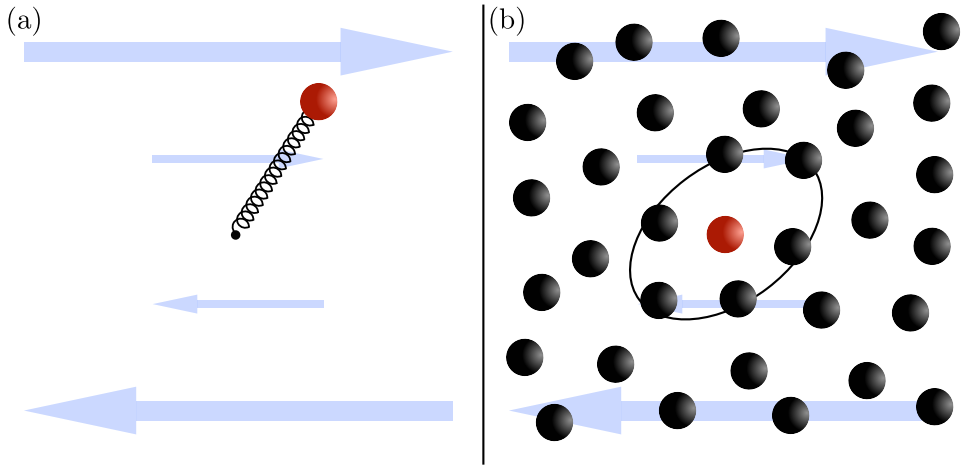

Figure 5.2.: Sketch of the systems studied: (a) Single particle bound to the origin by a harmonic potential depicted as a spring. (b) Tagged particle (red) in a dense colloidal suspension. The line marks the shape of the shell of its nearest neighbors. Both systems are driven into a NESS by a linear shear flow.

and consequently

$$X_i(0) = m\left\langle v_i^2 \right\rangle \equiv \theta_i. \tag{5.23}$$

The right-hand side is the kinetic temperature θ_i quantifying the velocity fluctuations of component i. In the following, we study for two systems, see Fig. 5.2, whether, and under which conditions, Eq. (5.23) extends to $t > 0$, i. e., whether $X_i(t) \approx \theta_i$.

5.4.1. Trapped particle in shear flow

The first model we investigate in this context is a single particle trapped in the harmonic potential

$$U(r) = \frac{1}{2}kr^2 \tag{5.24}$$

with the potential strength k and the displacement from the origin $r \equiv |\mathbf{r}|$. As the restoring force is linear, the z component in Eq. (5.15) decouples and remains in equilibrium independent of the driving, i. e., $X_z(t) = \theta_z = 1$. We will therefore focus on the x-y plane in this part.

Analytical results

For a harmonic potential, the equations of motion (5.15) comprise a system of first order differential equations. The solution for the velocity reads

$$\mathbf{v}(t) = \mathsf{G}^{vr}(t)\mathbf{r}_0 + \mathsf{G}^{vv}(t)\mathbf{v}_0 + \frac{1}{m}\int_0^t \mathsf{G}^{vv}(t-t')\boldsymbol{\xi}(t')\mathrm{d}t' \tag{5.25}$$

with the initial position $\mathbf{r}_0 \equiv \mathbf{r}(0)$ and velocity $\mathbf{v}_0 \equiv \mathbf{v}(0)$. The complete set of Green's functions $\mathsf{G}(t)$ and a brief derivation are given in Appendix D. Both the velocity autocorrelation function (VACF) and the response function can be obtained from Eq. (5.25). For the VACF, we find

$$\mathsf{C}(t) = \left\langle \mathbf{v}(t)\mathbf{v}_0^{\mathrm{T}} \right\rangle = \mathsf{G}^{vr}(t)\left\langle \mathbf{r}_0\mathbf{v}_0^{\mathrm{T}} \right\rangle + \mathsf{G}^{vv}(t)\left\langle \mathbf{v}_0\mathbf{v}_0^{\mathrm{T}} \right\rangle, \tag{5.26}$$

while the response function is trivially related to the Green's function by

$$\mathsf{R}(t-t') = \frac{1}{2}\left\langle \mathbf{v}(t)\boldsymbol{\xi}^{\mathrm{T}}(t') \right\rangle = \frac{1}{m}\mathsf{G}^{vv}(t-t'), \tag{5.27}$$

where we have used Eq. (C.5) and the noise correlations Eq. (2.2). The moments involved in Eq. (5.26) are connected to the Green's functions by Chandrasekhar's theorem [96] and are given by

$$\left\langle \mathbf{r}_0\mathbf{v}_0^{\mathrm{T}} \right\rangle = \frac{1}{2k}\begin{pmatrix} 0 & -\dot\gamma \\ \dot\gamma & 0 \end{pmatrix} \tag{5.28}$$

$$\left\langle \mathbf{v}_0\mathbf{v}_0^{\mathrm{T}} \right\rangle = \frac{1}{m}\mathbb{1} + \frac{1}{2k}\begin{pmatrix} \dot\gamma^2 & 0 \\ 0 & 0 \end{pmatrix}, \tag{5.29}$$

see Appendix D. Hence, the kinetic temperatures perpendicular to the shear flow are $\theta_y = \theta_z = 1$, see Eq. (5.23), whereas

$$\theta_x = 1 + \alpha_x\dot\gamma^2 \geq 1 \tag{5.30}$$

with $\alpha_x \equiv m/(2k)$. As changing the sign of the strain rate cannot change the kinetic temperature, we expect θ_x to depend only on even powers of $\dot\gamma$. The property that no powers larger than two appear in θ_x is due to the linearity of the interaction forces and does not extend to nonlinear systems.

FDT

With the explicit expressions for $\mathsf{C}(t)$ and $\mathsf{R}(t)$, we can compute the FDR for any component. For $C_{yy}(t)$, i. e., for the diagonal component perpendicular to the flow field the first term on the right-hand side of Eq. (5.26) vanishes. Hence, we have

$C_{yy}(t) = G^{vv}_{yy}(t) \langle v_y^2 \rangle = m \langle v_y^2 \rangle R_{yy}(t) = R_{yy}(t)$ and therefore $X_y = \theta_y = 1$ for any time t. By contrast, in the direction parallel to the shear flow, we obtain

$$C_{xx}(t) = \theta_x R_{xx}(t) + \langle y v_x \rangle G^{vr}_{xy}(t), \tag{5.31}$$

i. e., the velocity correlations are expressed through the response times the kinetic temperature plus a correction term arising from the off-diagonal components of the Green's function and the moments. This correlation function is represented in a hybrid form including parts of both the additive structure of an FDT in a NESS, cf. Eq. (5.9), and a constant multiplicative factor from an effective temperature approach. Separating the dependence on strain rate, the correction term can be rewritten as

$$\langle y v_x \rangle G^{vr}_{xy}(t) \equiv \dot{\gamma}^2 \beta_x I_x(t), \tag{5.32}$$

where $\beta_x \equiv \max |\langle y v_x \rangle G^{vr}_{xy}(t)/\dot{\gamma}^2|$ captures the magnitude of the correction term and $I_x(t)$ accounts for the shape of its time dependence with $\max |I_x(t)| = 1$. As demonstrated in Fig. 5.3(a), increasing the trap strength k strongly decreases β_x, i. e., the additive correction becomes less and less important until finally, the response and correlation functions are related by the constant kinetic temperature θ_x. Yet, an application of this approximately time-independent FDR, $X_x(t) \approx \theta_x$, in an effective temperature approach becomes interesting only if θ_x simultaneously deviates from one, i. e., from the equilibrium value. From Eq. (5.30), we see that the latter is true for $k \ll m\dot{\gamma}^2$. In the oscillatory regime, i. e., for $k \gtrsim 1/m$, we find that $k \gg \max\{\dot{\gamma}^2, m\dot{\gamma}^2\}$ must hold for an approximately time independent FDR, for details see Appendix E. This general behavior is sketched for $m \lesssim 1$ in Fig. 5.3(b), where in the upper left region the FDR is approximately constant, and in the lower right region the kinetic temperature is significantly larger than one, $\theta_x \gg 1$. For low masses, these regions are separated by a gap (shaded area), i. e., the FDR cannot be both constant and larger than one simultaneously. For increasing masses, the regions come closer. For $m \gtrsim 1$, the gap finally vanishes and, in the vicinity of the borderline, a constant FDR deviating from one can be realized.

In Fig. 5.4, we plot the scaled response and correlation functions for the three cases we have just discussed. First, in the left panel, Fig. 5.4(a), we show the response and correlation function for parameters with a kinetic temperature deviating significantly from one, however, with an obviously time-dependent FDR. Second, in the right panel, Fig. 5.4(c), we show the case of an almost perfectly time-independent FDR, but with a kinetic temperature barely deviating from the equilibrium value. Finally, in the central panel, Fig. 5.4(b), we demonstrate that there is indeed a regime of intermediate trap strength $k \sim m\dot{\gamma}^2$ with an increased effective temperature, where nevertheless $X_x(t) \approx \theta_x$ holds to a very good degree.

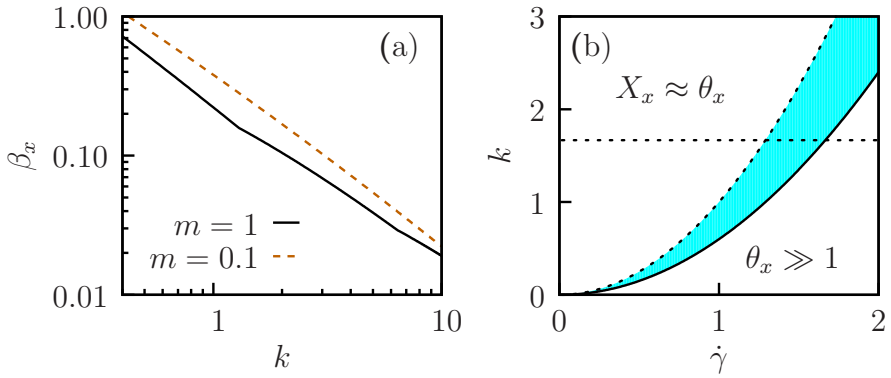

Figure 5.3.: (a) Magnitude of the correction term β_x, as a function of k for two different masses. (b) Sketch of the different regimes of the FDT for $m = 0.6$. The dashed lines $\dot{\gamma}^2$ and $1/m$ limit the region where the FDR is approximately time independent, i. e., $X_x \approx \theta_x$. Below the solid line $m\dot{\gamma}^2$, the kinetic temperature is much larger than unity. While for the chosen m there is a gap (shaded area), with increasing m both regimes can be realized in the vicinity of the solid line.

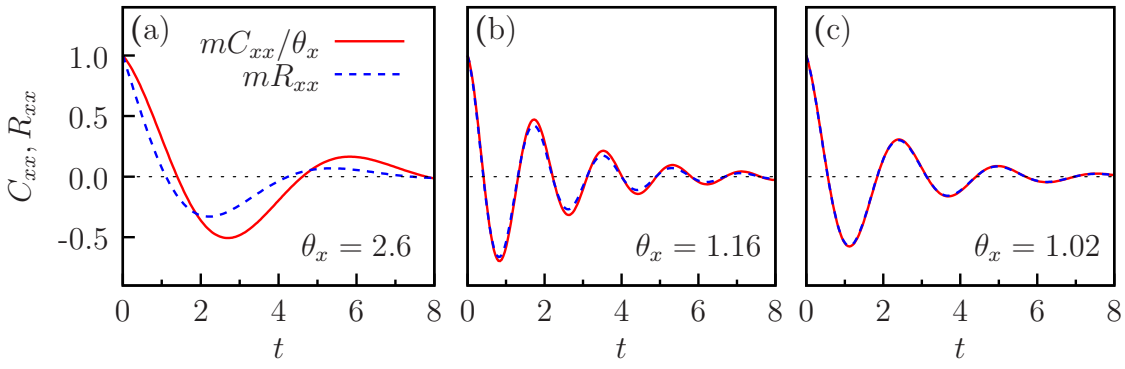

Figure 5.4.: Scaled velocity autocorrelation functions $C_{xx}(t)/\theta_x$ and corresponding response functions $R_{xx}(t)$ vs. time t for strain rate $\dot{\gamma} = 2.0$ and the following remaining parameters (a) $m = 1$, $k = 1.25$; (b) $m = 1$, $k = 12.5$; (c) $m = 0.25$, $k = 25$.

5.4.2. Tagged particle in a suspension

Now, we turn to a much more complex system. Specifically, we consider the FDR for a suspension composed of N particles without hydrodynamic interactions in which we follow a single particle. Without loss of generality, we tag the particle with index $k = 1$ with the corresponding position $\mathbf{r}_1$ and velocity $\mathbf{v}_1$. The interaction between the particles is defined through a pairwise interaction with the potential $u(r)$ leading to the total potential energy

$$U = \sum_{i<j} u(|\mathbf{r}_i - \mathbf{r}_j|). \tag{5.33}$$

The linear shear flow implies different solvent velocities for different regions in the suspension leading to the well-known Taylor dispersion [150]. This varying solvent velocity strongly affects the velocity autocorrelation and response functions. For the system discussed above, this issue was irrelevant as the particle was confined to a small volume around the origin. Here, the particle coordinates are not bounded and we deal with this problem by introducing the relative velocities with respect to the local shear flow

$$\tilde{\mathbf{v}}_i \equiv \mathbf{v}_i - \mathbf{u}(\mathbf{r}_i) \tag{5.34}$$

instead of the absolute velocity $\mathbf{v}_i$ as the observable entering the response $\mathsf{R}(t)$ and correlation functions $\mathsf{C}(t)$.

Time scale separation

In a fairly dense suspension, the tagged particle is in general surrounded by a "cage" of neighbors. Within such a cage, there is typically a local potential minimum, say at $\mathbf{r}_0$, and we expect the tagged particle to be close to $\mathbf{r}_0$ very often. Linearizing the total interaction force acting on the tagged particle around $\mathbf{r}_0$ leads to

$$-\boldsymbol{\nabla}_1 U \approx -\mathsf{k}(t)[\mathbf{r}_1(t) - \mathbf{r}_0(t)], \quad k_{ij} \equiv \frac{\partial^2 U}{\partial r_i \partial r_j}. \tag{5.35}$$

Now, we assume a time scale separation between the motion of the local potential-energy minimum $\mathbf{r}_0$ and the vibrational motion of the tagged particle around $\mathbf{r}_0$. The underlying physical picture is that of particles vibrating in an effective "cage" formed by surrounding particles and that local reorganization, or "cage breaks", occur on a time scale much longer than the vibrational motion. Assuming that $\mathbf{r}_0(t)$ is approximately constant, we can solve the resulting linear equations of motion analogously to the case of the trapped particle leading to formally identical results for the correlation function and the response function, see Eq. (5.26) and

Eq. (5.27), respectively. In principle, the Green's functions can be calculated also for a time-dependent k, but we will not need their explicit forms here. A crucial difference to the trapped particle is that this system is homogeneous and thus translationally invariant. Consequently, the first term in Eq. (5.26) vanishes. This point becomes obvious by considering the projected stationary pdf

$$\bar{\Psi}^{\mathrm{s}}(\mathbf{r}_1, \tilde{\mathbf{v}}_1) \equiv \int \mathrm{d}\mathbf{r}_2 \cdots \int \mathrm{d}\mathbf{r}_N \int \mathrm{d}\tilde{\mathbf{v}}_2 \cdots \int \mathrm{d}\tilde{\mathbf{v}}_N \Psi^{\mathrm{s}}(\mathbf{R}, \tilde{\mathbf{V}}) \tag{5.36}$$

with $\mathbf{R} \equiv \{\mathbf{r}_1, \ldots, \mathbf{r}_N\}$ and $\tilde{\mathbf{V}} \equiv \{\tilde{\mathbf{v}}_1, \ldots, \tilde{\mathbf{v}}_N\}$. Due to the homogeneity of the suspension, $\bar{\Psi}^{\mathrm{s}}$ cannot depend on the position $\mathbf{r}_1$ and therefore $\left\langle \mathbf{r}_1 \tilde{\mathbf{v}}_1^{\mathrm{T}} \right\rangle \sim \langle \tilde{\mathbf{v}}_1 \rangle = 0$ vanishes. Hence, we obtain

$$C_{ii}(t) = \theta_i R_{ii}(t) + m \sum_{j \neq i} \left\langle \tilde{v}_1^i \tilde{v}_1^j \right\rangle R_{ij}(t), \tag{5.37}$$

with $\tilde{\mathbf{v}}_1 \equiv (\tilde{v}_1^i)$. Also for a tagged particle in a suspension, we find a hybrid form of the FDT with the kinetic temperature connecting response and correlation function plus an additive correction term. The shape of the correction term, however, differs from the one in Eq. (5.31) due to the different symmetry properties. Here, the deviation stems from the off-diagonal components of the response functions instead of the Green's function coupling velocity and position. Note that this result holds not only for dense suspensions but is also valid in the dilute limit as, in general, a weak interaction can be linearized.

Langevin dynamics simulation

In order to study Eq. (5.37) for a specific system, we perform Langevin dynamics simulations. In a cubic simulation box of volume V, $N = 1728$ colloidal particles interact through the purely repulsive Yukawa pair potential

$$u(r) = \begin{cases} \epsilon \frac{e^{-\kappa(r-1)}}{r} & (r \geqslant 1) \\ \infty & (r < 1), \end{cases} \tag{5.38}$$

where ϵ is the interaction energy at contact and κ^{-1} is the screening length. The magnitude of κ is influenced mainly by the ion concentration in the solvent and interpolates between Coulombic (low κ, low ion concentration) and hard-sphere interactions (large κ, high ion concentration). We choose $\epsilon = 8.0$ and $\kappa = 5.0$ in order to obtain a broad range of densities for which the liquid phase is stable [151]. Since we are interested in the bulk behavior of the liquid, we impose Lees-Edwards boundary conditions [152]. We integrate the equations of motion by a stochastic velocity Verlet algorithm [152] with a time step of 5×10^{-4}, for details refer to

Appendix F. In order to implement the hard-core repulsion and prevent the particles from overlapping, we employ a simple algorithm which detects collisions and computes the computes the appropriate positions and velocities after the impact according to momentum and energy conservation, see Appendix F.

In the following, we study the correlation and response functions, $\mathsf{C}(t)$ and $\mathsf{R}(t)$, respectively, in NESSs for different volume fractions $\phi \equiv \pi N/(6V)$ and strain rates $\dot{\gamma}$. We prepare these states by initializing the particle positions on a regular lattice at low density. Then, we equilibrate the system and slowly increase the density by scaling down both the particle coordinates and the edge length of the simulation box. Once we have reached the final density, we slowly ramp up $\dot{\gamma}$ until the system reaches the desired strain rate. Finally, we simulate another 1000 time steps to relax the system into the steady state. This procedure is conducted separately for every independent run. In these NESSs, we record the trajectories for 200 randomly chosen particles in four independent runs. From this data, we can easily infer the VACF. The conventional way to determine response functions in such a simulation would be to apply a step perturbation of the force to the tagged particles and record their subsequent velocity relaxation. After many repetitions, one would obtain the response function as the time derivative of the mean velocity divided by the perturbation force. Here, we avoid this time consuming procedure by using the variant

$$\mathsf{R}(t-t') = \frac{1}{2}\left\langle \tilde{\mathbf{v}}_1(t)\boldsymbol{\xi}_1^{\mathrm{T}}(t')\right\rangle \tag{5.39}$$

of Eq. (C.5) holding also for the case of the tagged particle in an interacting suspension. Since in a Langevin dynamics simulation the stochastic forces are readily accessible, we merely need to record these forces for the tagged particles and can infer the response functions from steady-state correlations, i. e., without the need to actually perturb the system.

Effective confinement

In order to visualize the average environment of the tagged particle, we determine the stationary pair distribution function

$$\frac{(N-1)N}{V^2} g(\mathbf{r}_1,\mathbf{r}_2) \equiv \int \mathrm{d}\mathbf{r}_3 \cdots \int \mathrm{d}\mathbf{r}_N \int \mathrm{d}\tilde{\mathbf{V}} \Psi^{\mathrm{s}}(\mathbf{R},\tilde{\mathbf{V}}). \tag{5.40}$$

This function is proportional to the joint probability of finding a particle at position $\mathbf{r}_1$ given that there is another particle at $\mathbf{r}_2$ simultaneously. Because of the homogeneity of the suspension, g depends only on the relative coordinate $\mathbf{r}_{12} \equiv \mathbf{r}_1 - \mathbf{r}_2$. In the unsheared case, the suspension is also isotropic and g depends only on the absolute value of the displacement, whereas, in the sheared case, g is distorted

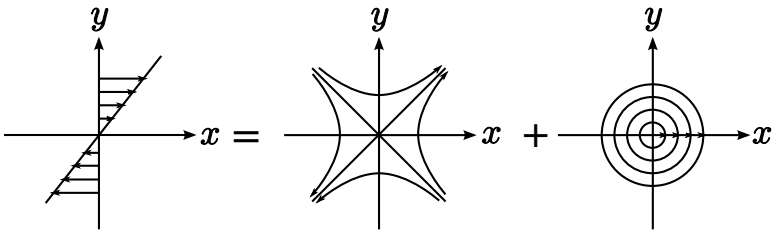

Figure 5.5.: A linear flow of the form $\mathbf{u}(\mathbf{r}) = \dot{\gamma} y \mathbf{e}_x$ can be decomposed in equal parts into a purely elongational $\mathbf{u}_{\mathrm{el}} \equiv \dot{\gamma}(y\mathbf{e}_x + x\mathbf{e}_y)/2$ and a purely rotational flow field $\mathbf{u}_{\mathrm{rot}} \equiv \dot{\gamma}(y\mathbf{e}_x - x\mathbf{e}_y)/2$.

mainly due to the elongational part of the flow field, see Fig. 5.5. Specifically, the neighbors are found on average more frequently in the compressional zones and less frequently in the extensional zones around the particle [153], see Fig. 5.6(a). Regardless of the flow field, there is a shell structure of neighbors around the tagged particle resulting from the fixed density. These shells manifest themselves in peaks along the radial direction of $g(\mathbf{r})$, see, e. g., Ref. [9]. With increasing density, these peaks become much more pronounced, see Fig. 5.6(a).

In Fig. 5.6(b), the response functions $mR_{xx}(t)$ are shown along with the scaled VACFs $C_{xx}(t)/\theta_x$ for volume fractions $\phi = 0.1$ and 0.4 for a range of strain rates. Even for times $t > 0$, these functions coincide which implies that the additive correction term in Eq. (5.37) is negligible. We observe the same behavior for the diagonal components in y and z direction. In order to understand this point, we need to discuss the off-diagonal components of the response functions and the moments for the corresponding velocity components. In Fig. 5.6(c), we show the off-diagonal response functions $R_{xy}(t)$ and $R_{yx}(t)$, i. e., the response of the mean relative velocity of the tagged particle in x and y direction when it is pulled in y and x direction, respectively. For every other off-diagonal combination, i. e., xz, yz, zx, and zy, the responses are too small to be detected in this simulation. The same is true for the corresponding off-diagonal moments $\langle \tilde{v}_1^x \tilde{v}_1^z \rangle \simeq 0$ and $\langle \tilde{v}_1^y \tilde{v}_1^z \rangle \simeq 0$. Defining the off-diagonal kinetic "temperature"

$$\theta_{xy} \equiv m \langle \tilde{v}_1^x \tilde{v}_1^y \rangle = \theta_{yx}, \tag{5.41}$$

we see that the dominant contribution to the additive correction term in Eq. (5.37) is $\theta_{xy} R_{xy}(t)$ for $C_{xx}(t)$ and $\theta_{xy} R_{yx}(t)$ for $C_{yy}(t)$. The correction for the zz component contains only off-diagonal terms of very small magnitude. In analogy to the trapped particle [cf. Eq. (5.32)], we separate the strain rate dependence from the correction terms,

$$\theta_{xy} R_{xy}(t) \approx \dot{\gamma}^2 \beta_x I_x(t), \quad \theta_{xy} R_{yx}(t) \approx \dot{\gamma}^2 \beta_y I_y(t), \tag{5.42}$$

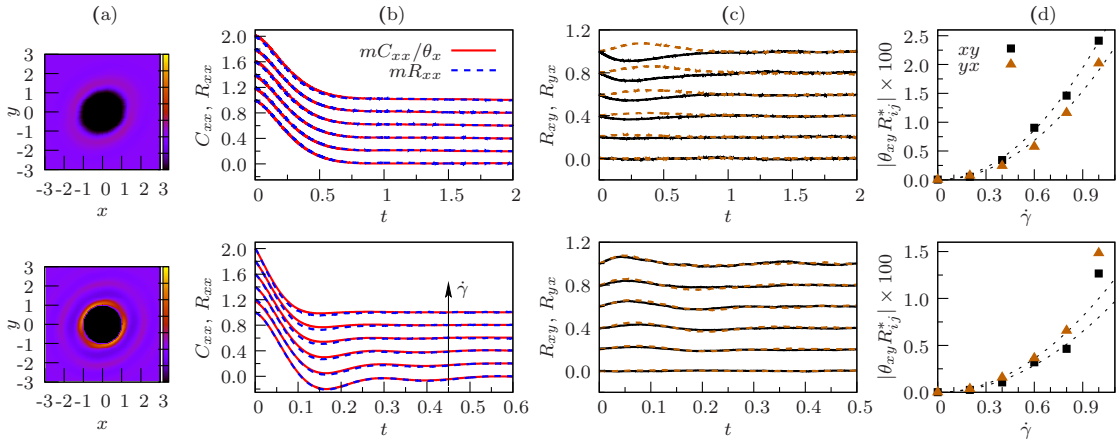

Figure 5.6.: Different results for a tagged particle with mass $m = 1$ in a sheared suspension at volume fractions $\phi = 0.1$ (top row) and $\phi = 0.4$ (bottom row). (a) Cross section of the pair distribution function in the x-y plane for strain rate $\dot\gamma = 1.0$. (b) Scaled velocity autocorrelation functions $C_{xx}(t)/\theta_x$ and response functions $mR_{xx}(t)$ for the strain rates $\dot\gamma = 0.0$, 0.2, 0.4, 0.6, 0.8, and 1.0 (from bottom to top). The curves are shifted for better visibility. (c) Off-diagonal response functions $R_{xy}(t)$ (solid lines) and $R_{yx}(t)$ (dashed lines) for the same strain rates and offsets. (d) Magnitude of the correction term $|\theta_{xy}R^*_{ij}|$ with the maximum R^*_{ij} of the off-diagonal response function shown in dependence of the strain rate. The dashed lines show quadratic fits.

where again $\max|I_i(t)| = 1$ and the coefficients β_i quantify the magnitude of the shear-reduced correction. Here, the quadratic dependence on the strain rate is not an exact result but an expansion to the lowest nonvanishing order in $\dot\gamma$. In Fig. 5.6(d), we show $|\theta_{xy}R^*_{ij}|$ as a function of the strain rate, where $R^*_{ij} = \max|R_{ij}(t)|$ is the maximal absolute value of the corresponding response function. For $\phi = 0.1$, the data follows the predicted quadratic dependence on $\dot\gamma$, while for $\phi = 0.4$ higher order terms become important above $\dot\gamma \simeq 0.8$.

In Fig. 5.7, we plot the diagonal components of the kinetic temperatures for the three spatial directions as a function of the strain rate. While there is a clear difference between the motion parallel to the flow (θ_x) and the motion perpendicular to the flow ($\theta_y \simeq \theta_z$) for $\phi = 0.1$, this distinction diminishes at higher densities. Moreover, all kinetic temperatures can be fitted by a quadratic function of the form of Eq. (5.30) with coefficients α_i for the three directions. The increase in the magnitude of the velocity fluctuations can be explained by collisions with neighbors caused by the flow gradient. This effect is more pronounced at higher densities and higher strain rates.

Fig. 5.7(c) shows the fitted coefficients α_i and β_x as functions of ϕ. The coeffi-

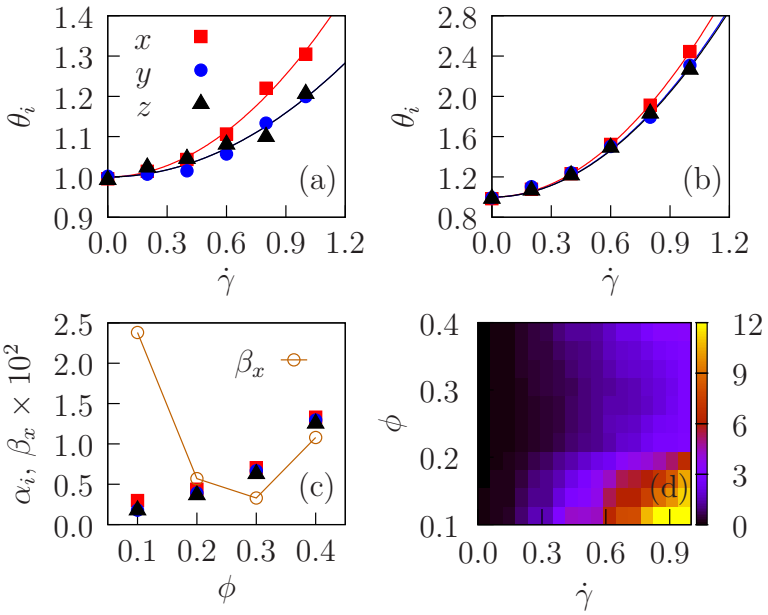

Figure 5.7.: (a),(b) Kinetic temperatures θ_i (symbols) and their quadratic fits (lines) in dependence of the strain rate $\dot{\gamma}$ for mass $m = 1$ for (a) $\phi = 0.1$ and (b) $\phi = 0.4$. (c) Coefficients α_i and $\beta_x \times 10^2$ as a function of the volume fraction ϕ. (d) Relative magnitude of the correction term compared to the kinetic temperature, $|\theta_{xy} R^*_{xy}|/\theta_x \times 10^3$ as a function of the strain rate and the density. Colors are linearly interpolated.

cient β_x decreases strongly for growing ϕ before it turns up again at $\phi = 0.4$. In order to judge the impact of the correction term on the quality of the FDR, it is helpful to visualize the ratio of the magnitudes of the correction term $|\theta_{xy} R^*_{xy}|$ and the corresponding kinetic temperature θ_x, see Fig. 5.7(d). We find that $|\theta_{xy} R^*_{xy}|/\theta_x < 0.02$ over the entire parameter range and $X_i(t) \approx \theta_i$ is thus fulfilled to a very good degree. However, we see that for large strain rates and low densities this ratio grows by an order of magnitude. Also for the highest density, the corrections to a time-independent FDR grow, albeit not as strongly as in the low density limit.

Deviations

In order to understand the corrections to the approximately time-independent FDR at high and low densities, we need to focus on the off-diagonal components of the response matrix. According to Eq. (5.37), we should be able to detect deviations under conditions where at least one off-diagonal component plays a significant role. Such conditions can be found when approaching the dilute limit,

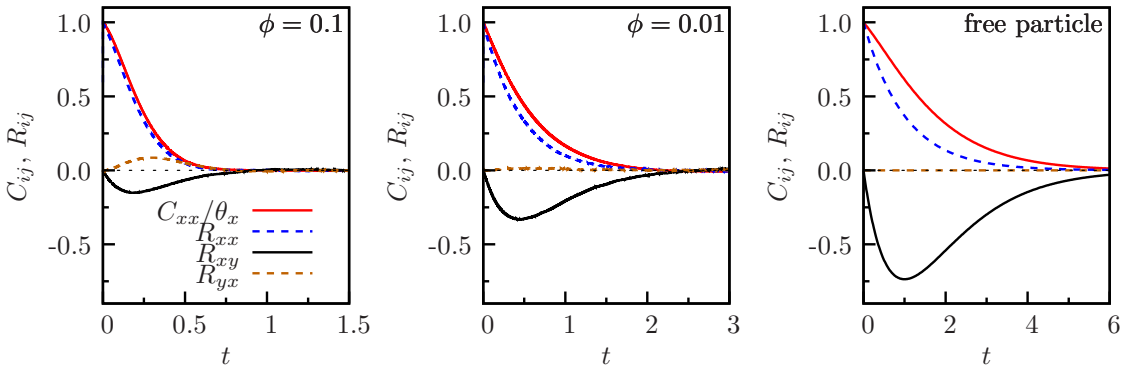

Figure 5.8.: Correlation and response functions at $\dot{\gamma} = 2.0$ for densities approaching the dilute limit (from left to right). The right panel shows analytical results for the dilute limit, i. e., for a free particle.

see Fig. 5.8. This point becomes clear when we consider the response of the x component of the relative velocity of a tagged particle pulled in, say, positive y direction. In a dilute suspension, the particle follows the force in y direction almost unobstructed by other particles. Moving upwards, i. e., in the positive y direction, it enters a region where the solvent flows faster. The relative velocity is thus negative until the particle has adapted its motion to the surrounding flow field, see sketch in Fig. 5.9(a). Hence, we observe a pronounced negative bulge in $R_{xy}(t)$. In a more dense suspension, the upwards-directed motion quickly decays due to collisions with neighboring particles, see Fig. 5.9(b). Relative velocities resulting from a velocity change in the surrounding solvent are thus negligible and the negative bulge is much smaller, see Fig. 5.8. Therefore, a large correction term at low densities becomes much smaller with increasing ϕ. In this sense, the strong confinement of a tagged particle leads to an equivalence of the FDR and the kinetic temperature.

Increasing the density further, we find that the magnitude of the off-diagonal corrections become larger again. This behavior results from the shear-induced distortion in the distribution of neighboring particles, cf. Fig. 5.6(a), and the resulting asymmetry in collisions with these neighbors. In contrast to the first mechanism, this process affects both the xy and the yx component of the response matrix. Specifically, pulling the particle upwards in the y direction, the distorted distribution of neighbors makes collisions with particles from the left more likely than with particles from the right, see also Fig. 5.9(b) for a schematic sketch. Likewise, if we pull the particle in x direction, there is a larger probability for impacts from below than from above. The asymmetric frequency of impacts causes, on average, an acceleration in the positive x or y direction for a perturbation force in the positive y or x direction, respectively. This acceleration manifests itself

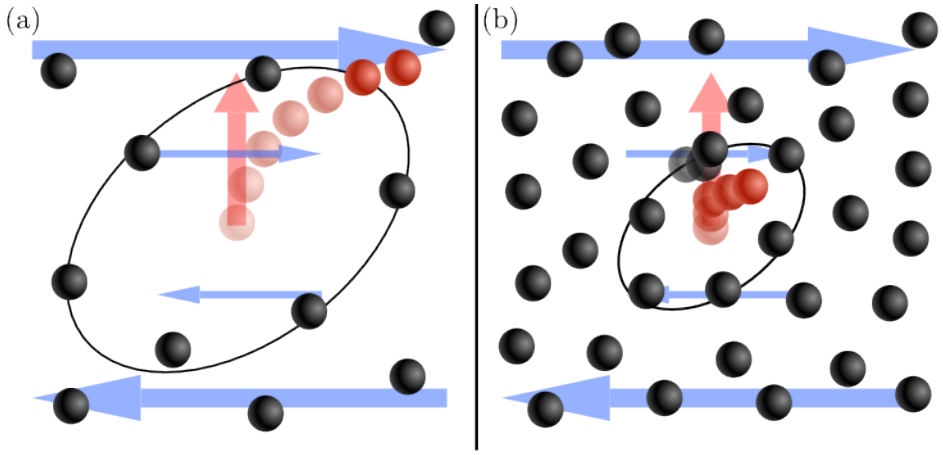

Figure 5.9.: Sketch of the time evolution after a force perturbation in the y direction (arrow) determining the shape of the $R_{xy}(t)$ response function. At low densities (a), the tagged particle is following the force almost freely. As for larger y the flow field velocity is also larger it is at first moving slower than the surrounding solvent due to inertia. At high densities (b), collisions with neighboring particles are more likely. Because of the shear-distorted distribution of neighbors, collisions push the tagged particle on average in the direction of the flow.

in a positive bulge in the off-diagonal response functions. With growing density, particle collisions become more frequent and this effect increasingly relevant. In Fig. 5.10, we can follow the xy component of the response matrix turn from its shape in the dilute regime into its form in the collision regime. For $\phi = 0.1$, the xy component of R shows a pronounced negative bulge. Hence, the dilute mechanism dominates for this density. For the highest density, we observe instead a positive bulge, which is characteristic for the collision effect. For intermediate densities, the response function is almost flat, as the two effects cancel each other out.

To summarize the behavior, the function $R_{xy}(t)$ is large at low densities, shrinking with increasing density. It becomes almost flat for intermediate densities and grows again for high ϕ, explaining the minimum of β_x at intermediate densities, see Fig. 5.7(c).

Overdamped limit

We have discussed and derived our results for systems with underdamped stochastic dynamics. In practice, inertial effects in colloidal systems are mostly negligible and the overdamped limit is perfectly sufficient. In order to discuss how these results approach the limit without inertia, we show the coefficients β_i and the kinetic temperature θ_x as functions of the reduced mass m. As expected, for small

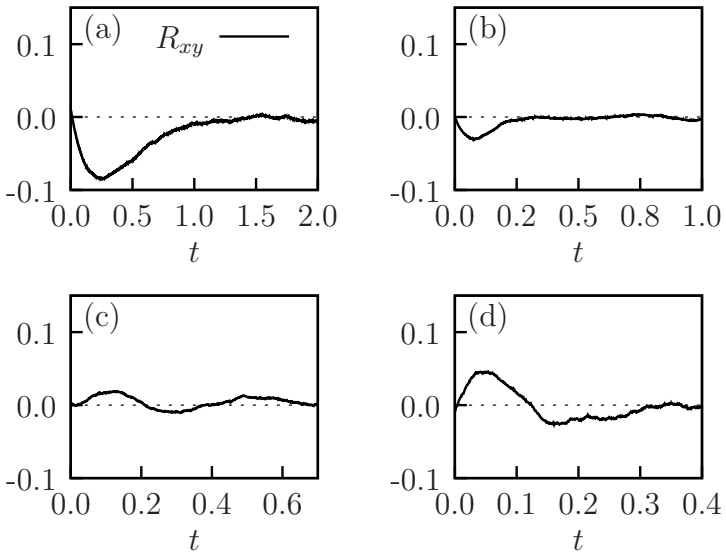

Figure 5.10.: Off-diagonal component $R_{xy}(t)$ for strain rate $\dot{\gamma} = 1.0$ for volume fractions (a) $\phi = 0.1$, (b) $\phi = 0.2$, (c) $\phi = 0.3$, and (d) $\phi = 0.4$. For low densities, the response function shows a pronounced negative bulge. Increasing the density, this negative bulge becomes very small for intermediate densities and turns into a positive one for the highest density.

masses, the kinetic temperature approaches unity, $\theta_i \approx 1$. Moreover, the additive correction term is no longer negligible as β_x and β_y grow strongly. We thus recover the FDT in the form of Eq. (5.13), in which only the bath temperature enters and the equilibrium form of the FDT is augmented by an additive excess correlation function.

5.5. Mobility and diffusivity in shear flow

An important property of the fluctuation-dissipation theorem for practical purposes is its close relation to transport coefficients. In particular, the velocity-force FDT discussed in detail in the preceding sections implies the Einstein relation

$$\mathsf{D} = T\mu \tag{5.43}$$

connecting the mobility μ and the diffusion coefficient D. Specifically, this relation follows from the equilibrium FDT, $\mathsf{C}(t) = T\mathsf{R}(t)$, by an integration over time, as the mobility and the diffusion coefficient,

$$D_{ij} \equiv \int_0^\infty C_{ij}(t)\mathrm{d}t \tag{5.44}$$

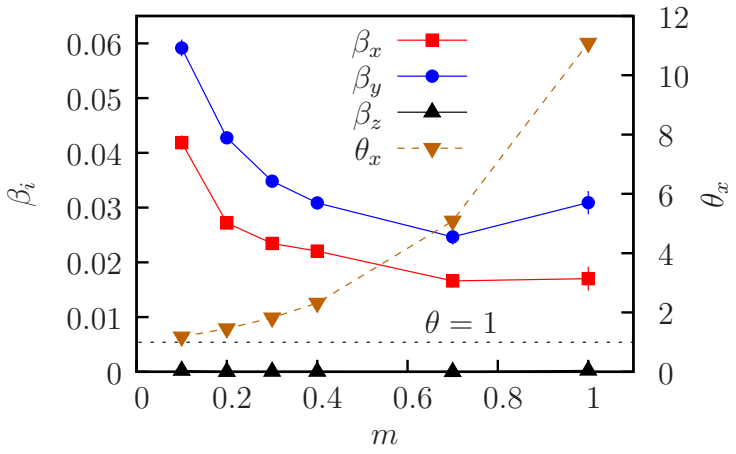

Figure 5.11.: Coefficients β_i (solid lines, left axis) and kinetic temperature θ_x as functions of the reduced particle mass m for volume fraction $\phi = 0.4$ and strain rate $\dot{\gamma} = 2.0$.

and

$$\mu_{ij} \equiv \frac{\partial \langle \tilde{v}_1^i \rangle}{\partial f_j} = \int_0^\infty R_{ij}(t)\mathrm{d}t, \tag{5.45}$$

respectively, are simply time-integrated versions of the velocity-force response function and the VACF. Obviously, along with the equilibrium FDT also the Einstein relation looses its validity in a NESS. However, if an effective temperature can be found relating response and correlation function in a time-independent manner, such a factor will recover the Einstein relation in a NESS as well.

Diffusion, characterizing the transport of a tagged particle through a homogeneous suspension, has been studied extensively in computer simulations [24, 25, 153–156], experiments [157, 158], and analytically [143, 159, 160]. The mobility, describing the velocity change in response to a small force, is much harder to determine both experimentally and numerically and has been addressed somewhat less prominently and mostly in analytic calculations [143, 161]. In the following, we will first focus on the diffusivity determined via Eq. (5.44) from the VACFs discussed in the preceding section. Then, we discuss the mobility coefficient obtainable from the velocity-force response functions using Eq. (5.45) and finally their connection via an approximate Einstein relation.

From our data, we find that the yy and zz component of the diffusion matrix are numerically identical. We thus distinguish only the diffusivity perpendicular to the flow field $D_\perp \equiv D_{yy} = D_{zz}$ from the diffusivity in the direction of the flow $D_\parallel \equiv D_{xx}$. In Fig. 5.12, we show $D_\parallel$ and $D_\perp$ as functions of the strain rate for different volume fractions. We find that diffusivity increases strongly with $\dot{\gamma}$.

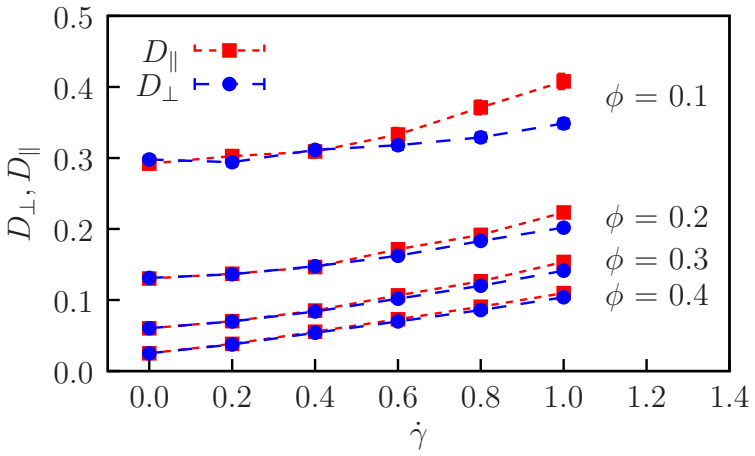

Figure 5.12.: Diffusion coefficients parallel $D_\parallel$ and perpendicular $D_\perp$ to the flow field as functions of the strain rate $\dot{\gamma}$ for $\phi = 0.1$, 0.2, 0.3, and 0.4.

This property results from the motion parallel to the shear gradient direction (y direction), which leads to larger fluctuations in the relative velocity and allows the particle to explore the phase space faster. While at low density diffusion is strongly anisotropic, specifically, $D_\parallel > D_\perp$, this difference vanishes for larger ϕ. This growing isotropy is closely related to the mechanisms depicted in Fig. 5.9. For low densities, fluctuations in y direction lead the particle into regions of different flow velocity in x direction and thus, on average, to larger fluctuations of v_x. For higher densities, the enhancement of fluctuations is still induced in the same way, i. e., in x direction. However, frequent collisions rapidly balance the increased mean-squared velocity among the three degrees of freedom. Moreover, we find that large densities heavily suppress the diffusivity of tagged particles. As an illustration, we note that, in the unsheared case, the diffusivity decreases from $D_\parallel = D_\perp = 1$ for a free particle to $D_\parallel = D_\perp \simeq 0.025$ for a tagged particle in a suspension at volume fraction to $\phi = 0.4$. Beside the enhancement of fluctuations, shear flow facilitates transport by steadily changing the positions of particles in relation to each other thus helping them to break out of temporary cages formed by neighbors. Hence, diffusivity increases more strongly with growing strain rate for larger densities.

For the mobility, we observe a similar behavior. With increasing density, the mobility of the tagged particle decreases rapidly, see Fig. 5.13(a). Similar to the diffusivity, also the mobility is enhanced by the shear flow. This effect is not detectable for low densities but clearly visible for larger ϕ, see Fig. 5.13(b). Note that in Fig. 5.13, we do not distinguish between the x, y, and z direction as they coincide in the range of our numerical accuracy, $\mu \equiv \mu_{xx} = \mu_{yy} = \mu_{zz}$.

The form of the dependence of the mobility on the strain rate appears surprising

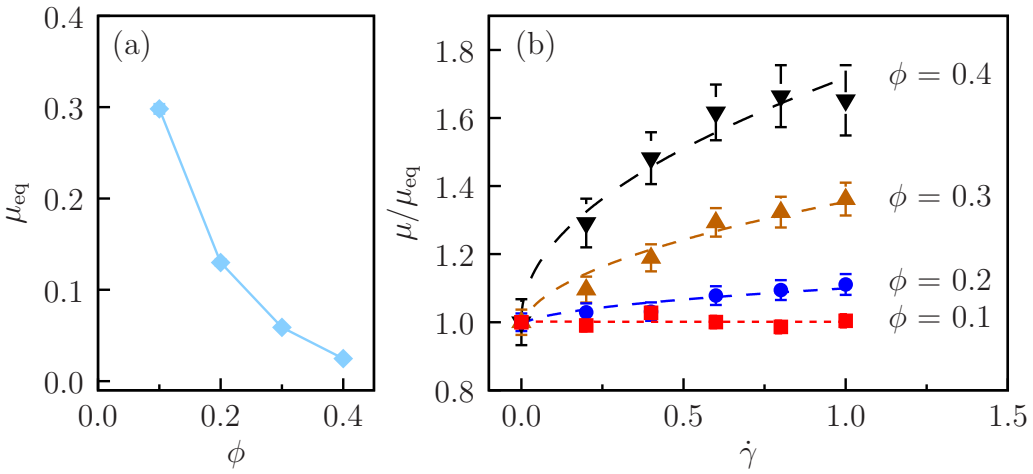

Figure 5.13.: (a) Mobility in the unsheared case μ_{eq} as a function of the volume fraction ϕ. (b) Reduced mobilities μ/μ_{eq} in dependence of the strain rate $\dot{\gamma}$ for different volume fractions. The lines are fits to Eq. (5.49).

at first glance. As μ must be invariant with respect to a sign change in $\dot{\gamma}$, one would expect an expansion to start with a term proportional to $\dot{\gamma}^2$, which apparently is not the case, see Fig. 5.13(b). In order to explain the shape of $\mu(\dot{\gamma})$, we compute the mean velocity of a tagged particle pulled through the suspension by a constant (small) force $\mathbf{f}$. For the steady-state velocity, the acceleration term in Eq. (5.15) is irrelevant. Also the stochastic forces do not contribute on average. Therefore, we obtain for the relative velocity for the tagged particle

$$\langle \tilde{\mathbf{v}}_1 \rangle = -\langle \boldsymbol{\nabla}_1 U \rangle + \mathbf{f} = -N^3/V \int g(\mathbf{r};\dot{\gamma},\mathbf{f}) \boldsymbol{\nabla} u(\mathbf{r}) \mathrm{d}\mathbf{r} + \mathbf{f}, \tag{5.46}$$

where, in the second step, we exploited that the potential U is a sum of identical pair potentials, see Eq. (5.33). The effect of the shear flow enters only through the pair distribution function g, which depends additionally on the density and the perturbation force. We can expand g into a regular Taylor series for small forces

$$g(\mathbf{r};\dot{\gamma},\mathbf{f}) \approx g(\mathbf{r};\dot{\gamma},0) + \sum_i \partial_{f_i} g(\mathbf{r};\dot{\gamma},\mathbf{f})|_{\mathbf{f}=0} f_i. \tag{5.47}$$

The dependence on $\dot{\gamma}$, however, must be handled with somewhat more care as the structure of the suspension is singularly perturbed by the shear flow [49, 96, 162]. The essential point causing this singularity is that no matter how small a strain rate we choose, we can never consider the contribution of the shear flow as small on all length scales. In the Fokker-Planck equation (2.15), and thus also in the pair correlation function, $\mathbf{u}(\mathbf{r}) = \dot{\gamma} y \mathbf{e}_x$ will always become dominant for large y. Such a

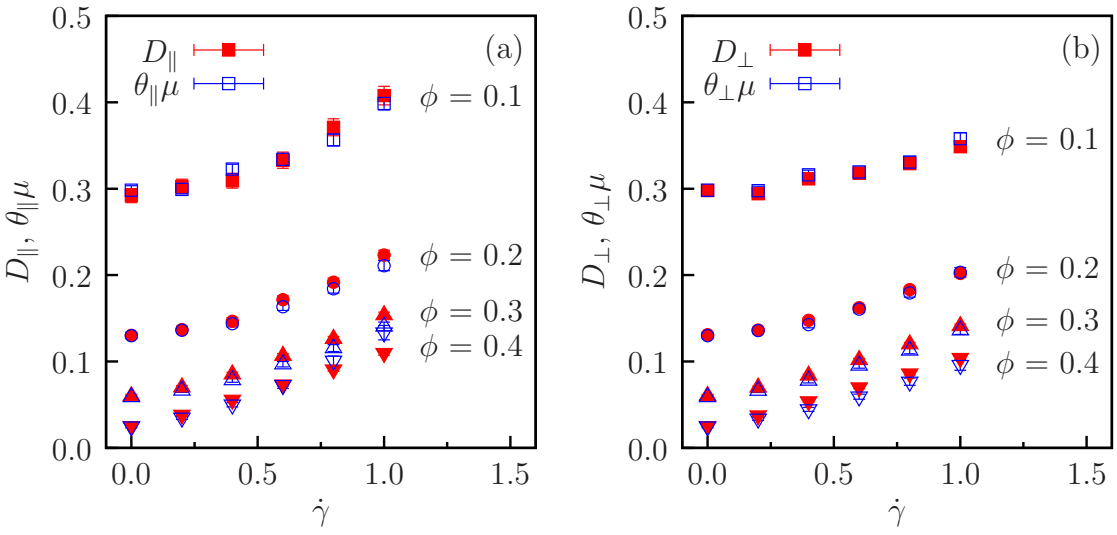

Figure 5.14.: Test of the Einstein relation $D_{ii} = \theta_i\mu_{ii}$ for components (a) parallel and (b) perpendicular to the flow field. We find a very good agreement for all considered densities. Only for the highest strain rates at $\phi = 0.4$ in the parallel case, we observe a deviation.

problem can be treated by employing the so-called *boundary layer theory* [96,163]. Van de Ven and Mason [162] showed that such a treatment leads to an expansion of the pair correlation function in powers of $\dot\gamma^{1/2}$ for a weak linear shear flow,

$$g(\mathbf{r};\dot\gamma,\mathbf{f}) \approx g^{(0)}(\mathbf{r};0,\mathbf{f}) + g^{(1)}(\mathbf{r};0,\mathbf{f})\dot\gamma^{1/2}. \tag{5.48}$$

Hence, using Eqs. (5.47) and (5.48), we obtain for the components of the mobility in the lowest order

$$\mu_{ij} \equiv \left.\frac{\partial\langle\tilde v_1^i\rangle}{\partial f_j}\right|_{\mathbf{f}=0} = \delta_{ij} - \left[N^3/V\int \partial_{f_j} g^{(1)}(\mathbf{r};0,\mathbf{f})\big|_{\mathbf{f}=0}\,\partial_i u(\mathbf{r})\mathrm{d}\mathbf{r}\right]\dot\gamma^{1/2}. \tag{5.49}$$

The expansion coefficients for different ϕ can, in principle, be obtained from the knowledge of the perturbed pair distribution function. Here, we determine them by fitting the mobility, see Fig. 5.13(b). The fits show a good agreement even though we have only used an expansion to the lowest order.

Finally, we use the approximate effective temperatures discussed in the preceding section to write down a generalized Einstein relation

$$D_{ii} = \theta_i\mu \tag{5.50}$$

for the diagonal components of the diffusion matrix. In Fig. 5.14, we test this relation by comparing the diffusivities D_{ii} to $\theta_i\mu$ for different strain rates and

densities. For θ_i, we employ the same quadratic expansion we already used in Figs. 5.7(a) and (b). We find a very good agreement for all parameters except for the largest density at $\dot{\gamma} \simeq 1.0$. There, we observe deviations in the components parallel to the flow field.

5.6. Conclusion and outlook

In this chapter, we have studied the fluctuation-dissipation theorem for a single colloidal particle subject to shear flow both in a harmonic trap and in an interacting colloidal suspension. In general, the FDT in such NESSs is given by the equilibrium form and an additive correction closely related to entropy production. Hence, the FDR is in general time dependent. For the case of an interacting colloidal suspension, we have found that this time dependence vanishes approximately. We have explained this result by deriving the FDR in a hybrid form containing both an additive and a multiplicative contribution. Under strong confinement, the additive contribution becomes negligible and the FDR is given by the kinetic temperature. Moreover, we have explored the limits of this behavior and investigated its implications on the Einstein relation in a colloidal suspension. Note that these findings are different from the effective temperatures found in glassy systems. There, effective temperatures were investigated for large time scales [24,25], while the systems were close to equilibrium at short times. Here, we considered the initial decay of response and correlation functions, i. e., we worked at short time scales but still far from equilibrium.

A prospect for future research is to check, whether the approximate effective temperature found in this chapter can be measured with a thermometer. Such a device could, e. g., consist of a probe particle immersed in the suspension with a mass M different from the other particles [24]. For this probe particle, one would then measure the kinetic temperature. For $M = m$, obviously the effective temperature of the probe particle is the same as the one of the colloidal particles in the suspension. However, varying M, this thermometer should respond on different time scales. Consequently, one might find different kinetic temperatures on longer time scales, as the present considerations do not necessarily extend into the tails of the response and correlation functions.

Another point concerns the dependence of the results on the type of observable and perturbation. An interesting choice accessible in Langevin dynamics simulations [140] is the response of the shear stress to a linear perturbation in the flow field. This pair of observable and perturbation would be fundamentally different from the present one, since the FDT would include the response of a collective observable to a collective perturbation in which no particle plays an eminent role. Moreover, in order to probe the FDR at longer time scales, one could investigate

density-density correlations in the regime of the structural relaxation time [164].

Finally, it should be tested to what extent the results depend on the type of the driving. Intriguing systems to approach this question include a tagged particle dragged through a dense suspension at a constant force or suspensions of self-propelled particles.

6. Shear-induced crystallization in a colloidal suspension

6.1. Introduction

In this final chapter, we focus on a somewhat different topic: the freezing transition of a disordered colloidal suspension into a crystalline solid. This phase transition is typically first-order and proceeds via a nucleation and growth mechanism [48]. In order to form a nucleus of the energetically favorable solid bulk, an energetically expensive interface must be created leading to a free-energy barrier. Before crystallization can start, this barrier needs to be overcome by a spontaneous fluctuation. Avoiding nucleation, the density of a suspension can be increased even beyond the thermodynamic freezing density[1] without solidification. Such a metastable state is then called *supersaturated*.

In contrast to atomistic systems, investigating the freezing transition of such a mesoscopic system has the advantage that the crystallization process is experimentally accessible. Both the spatial and temporal evolution can be monitored directly via light scattering [165–167] or in real space via confocal microscopy [39, 168], see also Ref. [169] for a review. Although the underlying dynamics for atomic and colloidal systems are similar, there is an essential difference. In colloidal suspensions, the crystallizing particles are immersed in a solvent adding friction and thermal fluctuations to the dynamics. Moreover, a flow field imposed on the solvent can influence the crystallization mechanism. Subjecting a colloidal suspension, e. g., to simple shear flow, the nucleation and growth kinetics can deviate significantly from those in the unsheared case [170, 171]. Even a dynamical coexistence of liquid and solid phases have been observed [172, 173]. Previous reports on the effects of shear flow on the crystallization rate are not conclusive. On the one hand, shear-enhanced crystallization has been reported for experiments [28–32] and numerical simulations [33, 34]. On the other hand, a suppression of nucleation

[1] In the limit of perfect hard spheres, the crystallization process is driven exclusively by entropy [9]. Consequently, density is the only relevant parameter in the phase diagram as it determines the accessibility of the phase-space regions. If we add a repulsive interaction to the hard shell, the phase diagram will depend on temperature as well. Yet, density will still be the dominant parameter.

has been observed experimentally [35] and numerically [36, 37]. Others report on an optimal strain rate for crystallization in supersaturated hard-sphere-like suspensions [38, 39] and protein solutions [40]. Optimal strain rates were also found in two dimensions for numerical simulations of Yukawa-type [41], Ising [42], and depletion-driven attractive [41] systems, as well as in a three-dimensional model glass [43].

In this chapter, we investigate this issue for a strongly supersaturated, charge-stabilized colloidal suspension in three dimensions [44] by means of a Langevin dynamics simulation. We observe that crystallization still proceeds via nucleation and growth as small clusters appear and disappear until one of them reaches a critical size. The subsequent growth process is dominated by a single large cluster. We find that the time for this cluster to reach a specific size which is larger than the critical size but still smaller than the total number of particles in the system becomes minimal at a finite strain rate. Note that the strain rates we apply in the process are so low that shear-induced layering plays no role [28, 156]. In order to scrutinize the underlying mechanisms causing this optimal strain rate, we introduce a discrete state model to describe the transitions between different structures in the environment of single colloidal particles. We identify two counteracting shear-dependent effects which become important at different stages during the evolution of the crystal. At the nucleation state, the formation of small crystalline clusters is hindered by the shear flow. We show that the origin of this behavior is the shear-induced disruption of a loose structure in the fluid. In unsheared liquids, such a pre-structured liquid has recently been shown to play a crucial role in the formation of the critical nucleus [174–177]. At the growth stage, the flow field facilitates the development of crystalline clusters. For this point, we give a tentative explanation relating the enhanced growth rate to convection. In this simple approach, we are able to derive the functional form of the cluster growth rate which we infer from our data. Finally, we discuss how shear flow affects the composition and transition in the solid. We find that it stabilizes a body-centered cubic structure and discuss how this might contribute to a faster growth as well.

6.2. Classical nucleation theory

Before we discuss the influence of shear flow on the crystallization process, we will briefly review the essential features of the CNT [93, 94] along the lines of Ref. [95]. In the process, we discuss how simple expressions for the free-energy barrier can be obtained within this approach.

In general, a liquid will crystallize if the chemical potential in the bulk of the solid phase is lower than that in the bulk of the fluid. In the process of creating the energetically favorable crystalline bulk, an energetically expensive interface must

be formed. Hence, to estimate the free-energy barrier $\Delta\mathcal{F}$ that must be overcome to initiate crystallization, we need to relate the free energy gained from the created crystalline bulk to the free-energy cost for the creation of the liquid-solid interface. For a spherical cluster of radius R containing n particles, we obtain [95]

$$\Delta\mathcal{F} = \frac{4\pi}{3}\frac{R^3}{V_\mathrm{p}}\Delta\mu + 4\pi R^2\gamma_\mathrm{s}, \tag{6.1}$$

where γ_s is the surface tension, i. e., the free-energy cost per unit area for an interface between the liquid and the solid, $\Delta\mu \equiv \mu_\mathrm{sol} - \mu_\mathrm{fl}$ is the difference in chemical potential between the liquid and the solid bulk, and

$$V_\mathrm{p} \equiv \frac{4\pi}{3}\frac{R^3}{n} \tag{6.2}$$

is the average volume accessible to one particle within the cluster. Using this volume [Eq. (6.2)], we represent the free-energy difference as a function of n

$$\Delta\mathcal{F} = n\Delta\mu + (36\pi V_\mathrm{p}^2)^{1/3} n^{2/3}\gamma_\mathrm{s}. \tag{6.3}$$

For $\gamma_\mathrm{s} > 0$ and $\Delta\mu < 0$, the free energy for a cluster of size n increases for small n, goes through a maximum at the critical cluster size

$$n^* \equiv -\frac{32}{3}\pi V_\mathrm{p}^2 \left(\frac{\gamma_\mathrm{s}}{\Delta\mu}\right)^3, \tag{6.4}$$

and decreases monotonously for large n, see Fig. 6.1. Hence, the liquid is metastable and crystallization must be initiated by a fluctuation forming a critical nucleus. In order to create such a critical cluster, the system needs to overcome the free-energy barrier

$$\Delta\mathcal{F}^* \equiv \max(\Delta\mathcal{F}) = \frac{16\pi}{3}\frac{\gamma_\mathrm{s}^3 V_\mathrm{p}^2}{\Delta\mu^2}. \tag{6.5}$$

The probability p^* for the formation of a critical nucleus is given by [178]

$$p^* \propto \exp\left(-\Delta\mathcal{F}^*/T\right), \tag{6.6}$$

i. e., it decreases exponentially with the height of the free-energy barrier. Hence, the nucleation process depends heavily on both the chemical potential difference $\Delta\mu$ and the surface tension γ_s. Conditions affecting either of these quantities can thus have a great impact on the time scale on which crystallization occurs. Influences such as interactions with confining walls [179–181] or impurities [182] can affect the surface tension and change the probability for nucleation significantly.

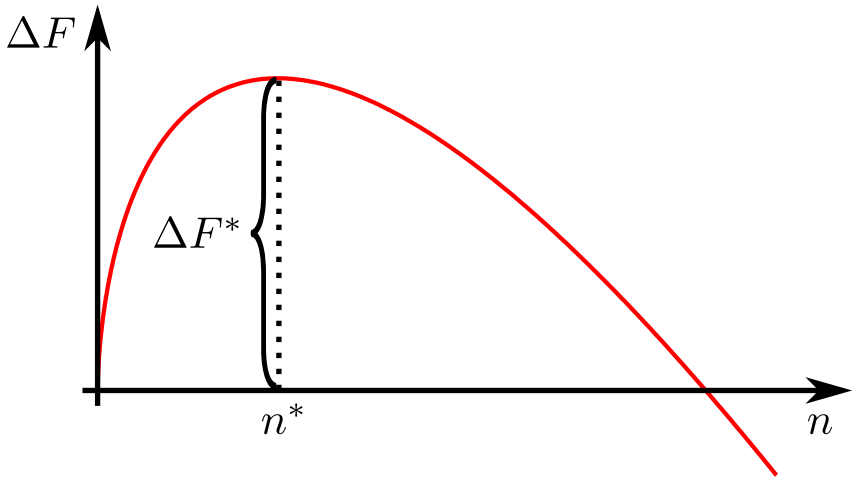

Figure 6.1.: Sketch of the free energy for the creation of a cluster of size n. The free-energy landscape goes through a maximum of height $\Delta\mathcal{F}^*$ at the critical cluster size n^*.

Impurities can act as catalysts for the nucleation process [182], but they can also increase the nucleation barrier, as observed, e. g., in polydisperse systems [183]. Therefore, one distinguishes two types of processes. If impurities, walls, etc., can be excluded, the nucleation process is denoted as *homogeneous* and as *heterogeneous* otherwise. In the following, we will exclusively consider homogeneous nucleation.

Although, on a fundamental level, CNT yields some insight into the crystallization process, it is still too simple to be considered general and comprehensive. One issue is, for instance, that the nucleus is modeled as a spherical droplet, which may be a valid approximation if the critical nucleus is large but breaks down for small clusters for which the surface structure cannot be considered as smooth anymore. Also, the chemical potential in a small cluster is not necessarily equivalent to the chemical potential in the solid bulk. A last but in the context of sheared systems crucial point is that CNT cannot be applied under nonequilibrium conditions because then the free energy is no longer a well-defined quantity.

6.3. Methods

6.3.1. System and simulation details

In order to investigate the crystallization process, we consider a monodisperse colloidal suspension consisting of $N = 4860$ particles in a nearly cubic simulation box[2] of constant volume V with volume fraction $\phi \equiv \pi N/(6V)$. Just as in the preceding chapter, we measure length, energy, and time in units of the particle diameter a, the thermal energy T, and the diffusive time scale $\tau_{\mathrm{D}} \equiv a^2/D_0$, respectively. We simulate the underdamped dynamics given by $\dot{\mathbf{r}}_i = \mathbf{v}_i$ and

$$m\dot{\mathbf{v}}_i = -\boldsymbol{\nabla}_i U - [\mathbf{v}_i - \mathbf{u}(\mathbf{r}_i)] + \boldsymbol{\xi}_i, \tag{6.7}$$

with the stochastic forces $\boldsymbol{\xi}_i$ of zero mean and correlations as defined in Eq. (2.2) and the potential

$$U = \sum_{j<j} u(|\mathbf{r}_i - \mathbf{r}_j|) \tag{6.8}$$

by employing the Langevin dynamics simulation described in Section 5.4.2 and Appendix F. Again, the particles of mass $m = 1$ interact via a repulsive Yukawa pair-potential including hard-sphere exclusion [see Eq. (5.38)]. In this case, we use the inverse screening length $\kappa = 8.0$ and the energy at contact $\epsilon = 10.0$. For this set of parameters, the freezing volume fraction is $\phi^* \simeq 0.38$. We are interested in the influence of a weak but steady shear flow $\mathbf{u}(\mathbf{r}) = \dot{\gamma} y \mathbf{e}_x$ with strain rate $\dot{\gamma}$ on the crystallization dynamics in the bulk of colloidal suspensions under highly supersaturated conditions ($\phi = 0.45$ and 0.52). Therefore, we again employ periodic Lees-Edwards boundary conditions [152].

Initial configurations for different runs are generated by equilibrating the system at low densities ($\phi = 0.2$). Subsequently, the volume fraction is increased stepwise by rescaling both the simulation box and the particle coordinates until the final volume fraction is reached. This procedure is done in 200 compression steps where we propagate the system for 100 time steps with $\Delta t = 0.0005$ after each compression. Once we reach the final volume fraction, we switch on the shear flow with strain rate $\dot{\gamma}$.

For a numerical treatment, molecular or Langevin dynamics simulations appear ideally suited to track the temporal development of crystalline nuclei since particle trajectories are easily accessible. However, if the nucleation process is hampered by a large free-energy barrier, the formation of a critical nucleus becomes a rare event. Depending on the height of the barrier, sampling such events ranges from difficult

[2] Dimensions of the box are (in units of the particle diameter a): $L_x = 16.876$, $L_y = 16.535$, and $L_z = 17.538$ for $\phi = 0.52$ and $L_x = 17.709$, $L_y = 17.351$, and $L_z = 18.404$ for $\phi = 0.45$.

to prohibitive unless specifically tailored methods are employed. Such methods include *transition path sampling* [184, 185], *forward flux sampling* [186, 187], and *umbrella sampling* [188, 189].

In this case, the high supersaturation in the system shifts the probability for nucleation into a regime accessible to straightforward sampling. Thus, we are able to investigate crystallization in the suspension by simple Langevin dynamics without resorting to importance sampling schemes.

6.3.2. Structure analysis

In order to describe the crystallization process quantitatively, we need a way to distinguish between liquid and solid structures. For a three-dimensional hard-core Yukawa system, the phase diagram of the equilibrium bulk structure includes, beside the liquid phase, the two crystalline structures *body-centered cubic* (bcc) and *face-centered cubic* (fcc) [48, 190, 191]. The fcc lattice is a dense sphere packing which deviates from a *hexagonal close packed* structure merely in the stacking sequence of their hexagonal planes. Hence, their free-energy difference is expected to be rather low [192] and hcp structures are likely to occur along with fcc structures, as it has been observed in microgravity experiments for hard-sphere colloids [193]. For the parameters studied here, the bulk equilibrium structure is fcc. However, in the spirit of the Ostwald step rule [194], intermediate structures may be of a different type. E. g., small nuclei have been found to be predominantly bcc structured in a Lennard-Jones liquid [195]. Hence, in our analysis, we will not only discern fcc from the liquid state but also include hcp and bcc structures.

We determine the symmetry of the local environment of a single particle by employing different variants of the well-known Steinhardt order parameters [196]. The basic idea is to construct quantities sensitive to rotational symmetries of connecting vectors $\mathbf{r}_{kj} \equiv \mathbf{r}_k - \mathbf{r}_j$ between the central, say the kth, particle and its set of neighbors $N_\mathrm{b}(k)$ with size $|N_\mathrm{b}(k)|$. Here, we consider all particles as neighbors that are located within a range of $R_\mathrm{b} = 1.4$ for $\phi = 0.52$ and $R_\mathrm{b} = 1.47$ for $\phi = 0.45$, which ensures that only first-shell neighbors are taken into account. Note that the range of this shell and thus also R_b vary with the density.

The central ingredient to the computation of the Steinhardt order parameters are the complex vectors $\mathbf{q}_l$ with components

$$q_{lm}(k) \equiv \frac{1}{|N_\mathrm{b}(k)|} \sum_{j \in N_\mathrm{b}(k)} Y_{lm}(\mathbf{r}_{kj}), \tag{6.9}$$

where Y_{lm} are spherical harmonics and the integers obey $l > 0$, $|m| \leq l$. Contrary to these vectors, a proper order parameter should be both real and independent of the choice of the coordinate system. In the following, we will therefore discuss different real and rotationally invariant combinations of the q_{lm}.

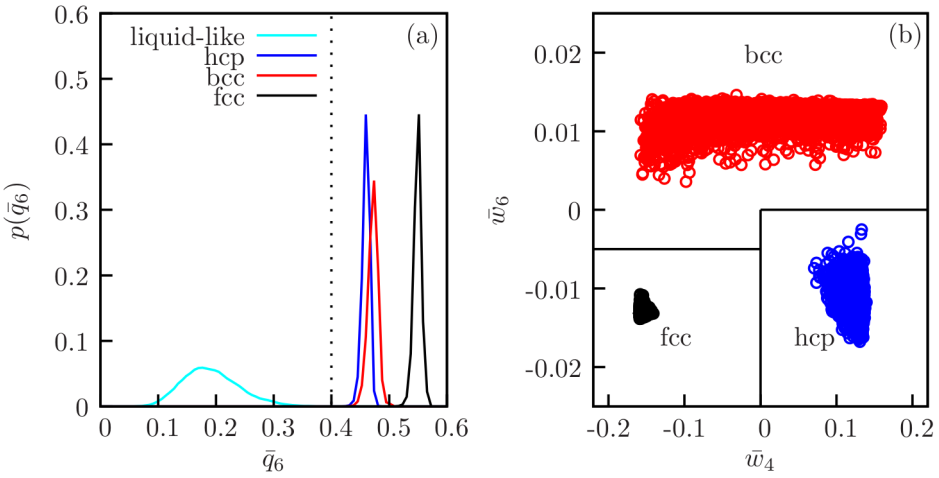

Figure 6.2.: (a) Histograms of $\bar{q}_6$ for a pure liquid and the three lattice structures hcp, bcc, and fcc. The $\bar{q}_6$ distributions of the three crystalline structures and the liquid are well separated. We choose $\bar{q}_6 = 0.4$ as the borderline (dashed line). (b) Scatter plot of $\bar{w}_4$-$\bar{w}_6$ trajectories for perfect hcp, bcc, and fcc crystals subject to thermal fluctuations. The $\bar{w}_4$-$\bar{w}_6$ plane is divided into the indicated regions which are used to determine the crystal structure of solid particles.

In the first step, we distinguish fluid particles from solid particles characterized by a disordered and an ordered environment, respectively. For this purpose, we make use of a recently introduced variant of the Steinhardt order parameters that averages over the second-neighbor shell [197],

$$\bar{q}_l(k) \equiv \sqrt{\frac{4\pi}{2l+1} \sum_{m=-l}^{l} |\bar{q}_{lm}(k)|}, \tag{6.10}$$

where

$$\bar{q}_{lm}(k) \equiv \frac{1}{|N'_{\mathrm{b}}(k)|} \sum_{j \in N'_{\mathrm{b}}(k)} q_{lm}(j) \tag{6.11}$$

and $N'_{\mathrm{b}}(k)$ is the set of neighboring particles including the kth particle itself. Averaging the order parameter this way sharpens the distinction between different structures at the expense of spatial resolution. For $l = 6$, the probability distributions of $\bar{q}_6$ for fluid and solid particles are well separated, providing a reliable means to discriminate these two basic structure types from each other, see Fig 6.2(a). We regard a particle as fluid if $\bar{q}_6 < 0.4$ and as solid otherwise.

Having determined these two particle sets, we further split the fluid particles into two subsets: liquid (liq) and pre-structured (pre). While liquid particles have

a truly disordered environment, we identify particles as pre-structured which have an environment that does not qualify as solid but where nevertheless some "bonds" between particles have formed. To substantiate the concept of a bond, we consider the normalized scalar product

$$S_{kj}^{(l)} \equiv \frac{\sum_{m=-l}^{l} q_{lm}(k) q_{lm}^*(j)}{\left(\sum_{m=-l}^{l} q_{lm}(k) q_{lm}^*(k) \right)^{1/2} \left(\sum_{m=-l}^{l} q_{lm}(j) q_{lm}^*(j) \right)^{1/2}}, \tag{6.12}$$

with q^* the complex conjugate of q. This product defines a measure for the strength of the correlation between the surrounding structures of the kth and the jth particle. We regard two neighboring particles as "bonded" if $S_{kj}^{(6)} > 0.5$ [198]. The number of bonds n_{bonds} represents a good indicator for how structured the vicinity of a particle is. Also in the liquid, particles will have a few bonds. If the number of bonds with neighboring particles is at least 8 (but still $\bar{q}_6 < 0.4$), we denote particle as pre-structured.

Finally, by employing another type of averaged order parameters [197]

$$\bar{w}_l(k) \equiv \frac{\sum_{m_1+m_2+m_3=0} \begin{pmatrix} l & l & l \\ m_1 & m_2 & m_3 \end{pmatrix} \bar{q}_{lm_1}(k) \bar{q}_{lm_2}(k) \bar{q}_{lm_3}(k)}{\left(\sum_{m=-l}^{l} |\bar{q}_{lm}(k)|^2 \right)^{3/2}}, \tag{6.13}$$

we are able to discern the different crystalline structures within the solid particles. The term in brackets is the Wigner-3-j symbol, which is related to Clebsch-Gordan coefficients. The sum runs over all combinations of m_1, m_2 and m_3 with $m_1 + m_2 + m_3 = 0$. In the following, it is sensible to work with $l = 6$ and $l = 4$ which can be seen as follows. Both fcc and hcp lattices contain planes of hexagonal symmetry. Additionally, both fcc and bcc structures are cubic lattices and thus contain fourfold symmetries. Indeed, using the two parameters $\bar{w}_4$ and $\bar{w}_6$, we obtain a good separation between the distributions in the $\bar{w}_4\bar{w}_6$ plane, see scatter plot in Fig. 6.2(b). The $\bar{w}_4$ distribution is widely separated for hcp and fcc structures, while $\bar{w}_6$ separates bcc from hcp and fcc. Hence, a solid particle is classified as fcc if $\bar{w}_4 \leq 0$ and $\bar{w}_6 \leq -0.005$ (lower left region), as hcp if $\bar{w}_4 > 0$ and $\bar{w}_6 \leq 0$ (lower right region), and as bcc otherwise (upper region). The complete decision process is summarized in Fig. 6.3.

6.3.3. Discrete state model

By using the above analysis, we categorize the structure of single particles according to their local environment. For a given configuration of particle positions at

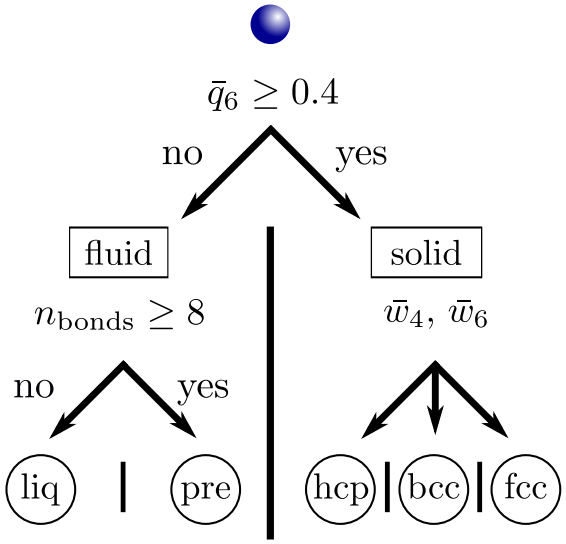

Figure 6.3.: Decision tree for the structure assignment to a single particle. First, the value of $\bar{q}_6$ classifies the particle as solid or fluid. Then, a fluid particles is denoted as pre-structured if it possesses 8 or more bonds with neighboring particles. A solid particle is assigned one of the three crystalline structures hcp, bcc, and fcc, according to the classification shown in Fig. 6.2(b).

time t, we define an indicator function $h_k(t)$ for every particle k which takes on one of the five values: liq, pre, hcp, bcc, or fcc. The population (fraction of all particles) in structure type i is

$$c_i(t) \equiv \frac{1}{N} \sum_{k=1}^{N} \delta_{i,h_k(t)}. \tag{6.14}$$

As the suspension evolves also the structural environment of the particles changes. We quantify these changes in the fluxes

$$f_{i \to j}(t) \equiv \sum_{k=1}^{N} \delta_{i,h_k(t)} \delta_{j,h_k(t+\delta t)} \tag{6.15}$$

counting the number of particles changing from structure i to structure j within a time interval $[t, t+\delta t]$, where we set $\delta t = 100\Delta t$ if not indicated otherwise.

Both the fluxes and the population trajectories are heavily fluctuating, time-dependent quantities. Therefore, a systematic discussion requires an appropriate averaging procedure. Since we start in a metastable configuration, the fluxes and populations do not only fluctuate but do also evolve systematically in time as a consequence of the overall progress in the crystallization process. In order to

provide a meaningful average, we need to choose an appropriate order parameter indicating the state of the advancement in the crystallization process. In the following, we use the size of the largest cluster n as an order parameter, where we define clusters as sets of solid particles that are mutually connected by bonds (in the sense defined above, i. e., $S_{kj}^{(6)} > 0.5$). Using this order parameter, we define the average composition at fixed n

$$\bar{c}_i(n) \equiv \left\langle c_i(t)\delta_{n,n(t))} \right\rangle / Z_n, \tag{6.16}$$

where in this chapter the average $\langle\cdot\rangle$ is understood as an average over time and over different realizations of the crystallization process, i. e., over different simulation runs, with the normalization constant $Z_n \equiv \left\langle \delta_{n,n(t)} \right\rangle$. Moreover, we define the 5×5 transfer matrix T with components

$$T_{i\to j}(n) \equiv \left\langle \frac{f_{i\to j}(t)}{N c_i(t)} \delta_{n,n(t)} \right\rangle \Bigg/ Z_n \tag{6.17}$$

and normalization $\sum_j T_{i\to j} = 1$. The component $T_{i\to j}(n)$ describes the average fraction of particles in state i that convert to state j within the time interval δt. We sort the eigenvalues $\lambda^{(i)}$ of T in decreasing order, $\lambda^{(0)} > \lambda^{(1)} > \cdots > \lambda^{(4)}$, with $\lambda^{(0)} = 1$. The components of the corresponding right-hand-side eigenvectors fulfill

$$\sum_i w_i^{(0)} = 1, \quad \sum_i w_i^{(\alpha)} = 0 \quad (\alpha \geq 1). \tag{6.18}$$

The product $\mathsf{T}(n(t))\mathbf{c}(t) = \mathbf{c}(t+\delta t)$ propagates the population at time t to the average population a time δt later, where $\mathbf{c}(t) \equiv (c_i(t))$. Applying the transfer matrix repeatedly describes an effective Markovian dynamics at fixed cluster size. Under this dynamics, the average population after an elapsed time τ becomes

$$\mathbf{c}(\tau) = \mathbf{w}^{(0)} + \sum_{\alpha=1}^{4} \zeta_\alpha \mathbf{w}^{(\alpha)} e^{-\tau/\tau_\alpha} \tag{6.19}$$

with time scales $\tau_\alpha(n) \equiv -\delta t / \ln \lambda_\alpha(n)$ and coefficients $\zeta_\alpha \equiv \mathbf{w}^{(\alpha)} \cdot \mathbf{c}(0)$. Hence, for $\tau \gg \tau_1$, the system approaches a (quasi)-stationary average population given by $\mathbf{w}^{(0)}$, where the relaxation time is determined by the largest eigenvalue unequal to one τ_1.

For a freely evolving suspension, the size of the largest cluster is of course not constrained to a fixed n. However, if there is a time-scale separation between the transitions described by $\mathsf{T}(n)$ and the change in n, the system relaxes into the quasi-stationary state before the size of the largest cluster grows any further.

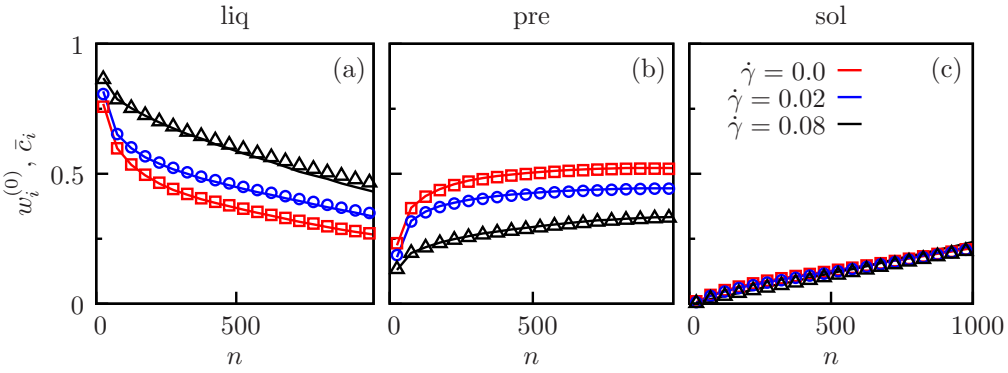

Figure 6.4.: Quasi-stationary populations in the (a) liquid, (b) pre-structured, and (c) solid state as functions of n (lines) and the corresponding average populations $\bar{\mathbf{c}}$ (symbols) actually found in the simulations.

Then, the actual average populations of local structures measured in the simulations should be equal to the stationary eigenvector: $\bar{\mathbf{c}}(n) \approx \mathbf{w}^{(0)}(n)$. Fig. 6.4 shows average composition actually observed in the suspension (symbols) and the corresponding components of the quasi-stationary eigenvector $\mathbf{w}^{(0)}$ (lines) for the liquid, the pre-structured, and the combined solid state, where $\bar c_{\mathrm{sol}} \equiv \bar c_{\mathrm{hcp}} + \bar c_{\mathrm{bcc}} + \bar c_{\mathrm{fcc}}$ and $w^{(0)}_{\mathrm{sol}} \equiv w^{(0)}_{\mathrm{hcp}} + w^{(0)}_{\mathrm{bcc}} + w^{(0)}_{\mathrm{fcc}}$. Deviations are small but increase with both increasing strain rate and cluster size up to maximal 7% at $n = 1000$. This demonstrates that the growth of the cluster is a slow process and that the lag time δt is sufficient to sample the fast dynamics described by $\mathsf{T}(n)$.

6.4. Crystallization process

6.4.1. Crystallization rate

We first examine the cumulative effect of shear flow on the speed of the crystallization process by recording the time it takes a supersaturated suspension to become solid. According to the protocol described above, we start in a supersaturated suspension and apply shear flow. Once the largest cluster has reached a size of 800, we record the elapsed time τ^*. For every combination of strain rate and density, we determine τ^* for 500 independent runs. Of course, we do not observe the same value for τ^* in every run but rather a characteristic distribution $p(\tau^*)$ for each parameter set. Figs. 6.5(a)-(c) show the normalized histograms for τ^* obtained from our simulations for $\phi = 0.52$ and strain rates $\dot\gamma = 0.0$, $\dot\gamma = 0.02$, and $\dot\gamma = 0.08$. For $\dot\gamma = 0.0$ and $\dot\gamma = 0.08$, the histograms are comparably wide. In particular, the ratio $\sigma_{\tau^*}/\langle\tau^*\rangle$ of the standard deviation σ_{τ^*} and the average value $\langle\tau^*\rangle$ over

all runs is 0.45 and 0.70 for $\dot{\gamma} = 0.0$ and $\dot{\gamma} = 0.08$, respectively. By contrast, for $\dot{\gamma} = 0.02$, the distribution is much sharper and concentrated around low τ^* with $\sigma_{\tau^*} / \langle \tau^* \rangle \simeq 0.20$.

Fig. 6.5(d) shows the mean value of the crystallization duration $\langle \tau^* \rangle$ as a function of $\dot{\gamma}$ for $\phi = 0.52$ and 0.45. We find a nonmonotonous dependence of $\langle \tau^* \rangle$ on $\dot{\gamma}$ for both densities. For small strain rates, $\langle \tau^* \rangle$ decreases and reaches a flat minimum for $\dot{\gamma} \simeq 0.02$ for $\phi = 0.52$ and a somewhat sharper minimum at $\dot{\gamma} \simeq 0.01$ for $\phi = 0.45$. A further increase of the strain rate leads to rapidly growing $\langle \tau^* \rangle$. At $\dot{\gamma} = 0.1$ and $\dot{\gamma} = 0.05$ for $\phi = 0.52$ and $\phi = 0.45$, respectively, already a significant part (more than 10%) of the 500 runs did not crystallize within 2×10^6 time steps. Hence, the overall effect of shear flow on the crystallization process is an acceleration for small strain rates followed by a strong increase in $\langle \tau^* \rangle$ at higher $\dot{\gamma}$.

Comparing the behavior of $\langle \tau^* \rangle$ for the two densities, we find that the decrease in the average crystallization duration is much stronger for the higher density for which it drops almost by a factor of 3, whereas for the lower density it decreases only by somewhat more than 20%. Furthermore, for $\phi = 0.45$, the steep increase of $\langle \tau^* \rangle$ starts already at lower $\dot{\gamma}$. Hence, compared to $\phi = 0.52$, the range of $\dot{\gamma}$ in which the strain rate accelerates the crystallization process narrows significantly.

Following the evolution of the size of the largest cluster n in time for typical runs at different strain rates, we find qualitative differences in the way the cluster grows, see Fig. 6.5(e). Without shear flow, the system starts crystallizing very quickly, whereas n grows only slowly. By contrast, in the high-shear case, the system stays at a low n for some time before the crystallization process initiates. Afterwards, n increases rapidly. Close to the optimal strain rate, we find features of both limiting cases. On one side, crystallization starts almost as early as in the unsheared case. On the other side, it grows faster later on.

6.4.2. Shear flow suppresses nucleation

Growth rate

In order to investigate the crystalline growth more systematically, a pertinent quantity to study is the growth rate of the largest cluster

$$\nu(n) \equiv \left\langle \frac{n(t+\delta t) - n(t)}{\delta t} \delta_{n,n(t)} \right\rangle \Big/ Z_n \tag{6.20}$$

averaged at fixed n, i. e., at a specific stage in the development of the largest cluster. In Fig. 6.6, we show this quantity for $n \leq 50$. For $\dot{\gamma} = 0.02$, the average growth rate is only marginally smaller than the one in the unsheared case. By contrast, for $\dot{\gamma} = 0.08$ the growth is strongly suppressed in a broad range $10 \lesssim n \lesssim 40$. One

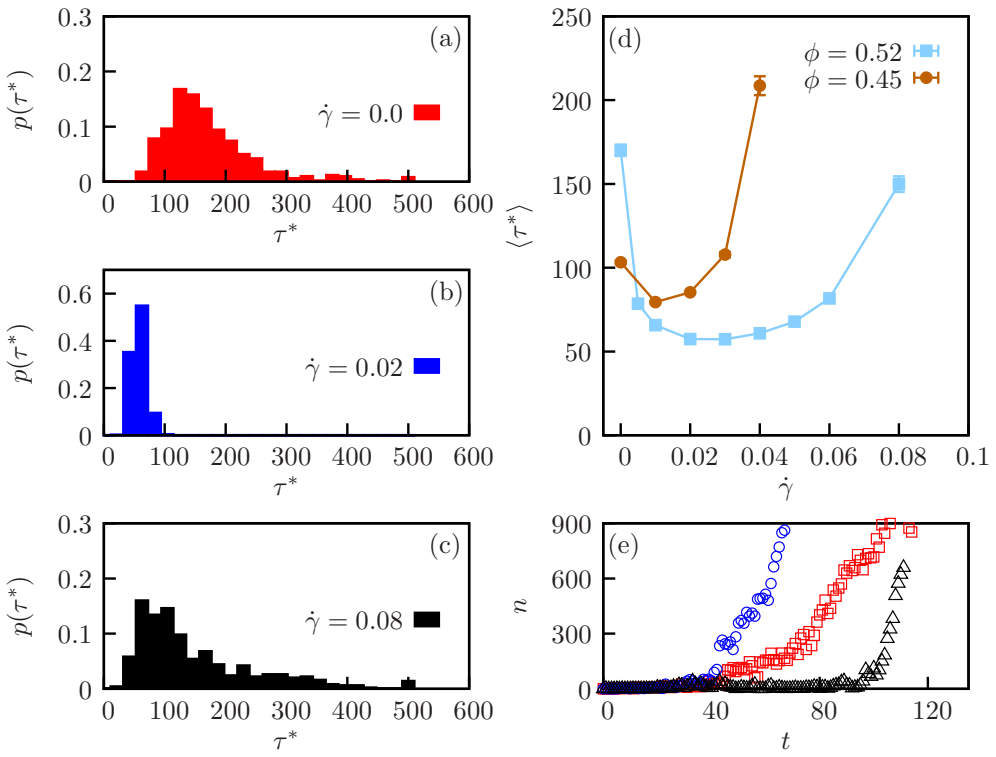

Figure 6.5.: (a)-(c) Histograms for the duration of the crystallization process at $\phi = 0.52$ for $\dot{\gamma} = 0.0$, 0.02, and 0.08. (d) Average value for the duration of the crystallization process $\langle \tau^* \rangle$ as a function of the strain rate with the standard error for the estimation of the mean value $\langle \tau^* \rangle$ of the distribution of τ^*. (e) Temporal development of n for typical runs at $\phi = 0.52$ for $\dot{\gamma} = 0.0$, 0.02, and 0.08.

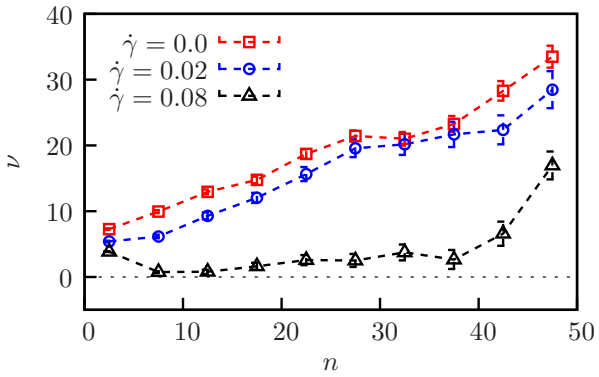

Figure 6.6.: Average growth rate of the size of the largest cluster as a function of n for different strain rates at $\phi = 0.52$. For large $\dot{\gamma}$, the growth rate of the largest cluster is strongly suppressed in an interval $10 \lesssim n \lesssim 40$.

might speculate that this shear-induced suppression of crystalline growth at small n results from the destruction of small clusters through the shear flow. However, even the largest of the applied strain rates ($\dot{\gamma} = 0.08$) is still very small. Therefore, it is doubtful whether the resulting weak shearing forces are sufficiently strong to destroy even small clusters. Yet, for the development of a loose structure in the fluid, even weak shearing forces might be decisive. In the following, we thus start the investigating this issue on the level of the development of a loose structure in the fluid.

Pre-structured liquid

A crystalline cluster is not likely to occur in the middle of an entirely random distribution of particles, whereas, in a region of the fluid which has already acquired a loosely ordered state, fluctuations transforming parts of this pre-structured liquid into a crystal are much more probable. For this system, this scenario applies as well. The fraction of pre-structured particles transferring to a solid state in a time interval δt is on the order of a few percent, $T_{\mathrm{pre}\to\mathrm{sol}} \simeq 3\%$, while the corresponding transfer from the liquid to the solid state is more than three orders of magnitude smaller, $T_{\mathrm{liq}\to\mathrm{sol}} < 10^{-5}$. In order to study the effect of shear flow on the structure of the fluid, we record the transfer matrix component $T_{\mathrm{liq}\to\mathrm{pre}}$. Likewise, we compute the corresponding backward component $T_{\mathrm{pre}\to\mathrm{liq}}$, see Fig. 6.7. Note that $T_{\mathrm{liq}\to\mathrm{pre}} < T_{\mathrm{pre}\to\mathrm{liq}}$ does not imply a net particle current from the pre-structured to the liquid state, as the transfer matrix component $T_{i\to j}$ describes the *fraction* of particles in state i transferring on average to j. In addition to the $T_{i\to j}$, the net current of particles depends as well on the population in these states. At this early stage in the crystallization process, there are significantly more liquid

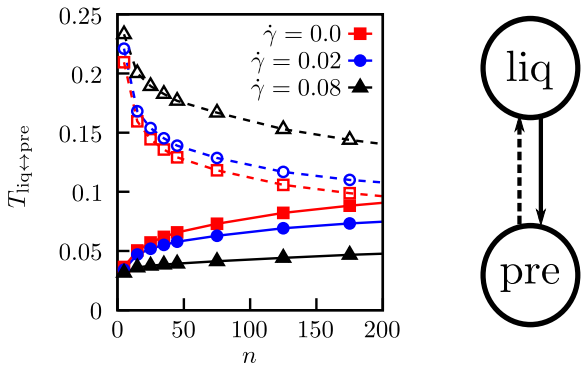

Figure 6.7.: Transfer matrix components for transitions from the liquid to the pre-structured state (solid lines) and the corresponding backwards transitions (dashed).

than pre-structured particles in the suspension and the net current is directed from liq to pre. Regarding the effect of the shear flow on the transfer matrix components, we find that it has a strong influence on the development of structure in the liquid. The establishment of bonds is inhibited, as can be seen from the reduced values for $T_{\mathrm{liq}\to\mathrm{pre}}$. Moreover, structure in the fluid is destroyed, resulting in an enhanced value for $T_{\mathrm{pre}\to\mathrm{liq}}$. Consequently, compared to the unsheared case, we find a much smaller fraction of pre-structured particles $\bar{c}_{\mathrm{pre}}$ in the suspension for $\dot{\gamma} = 0.08$, see Fig. 6.4(b). In other words, shear flow prevents the liquid from developing a loose structure.

Fig. 6.8 shows snapshots of the suspension at different stages in the evolution of the largest cluster for low and high $\dot{\gamma}$. In both cases, the crystallization is dominated by a single cluster. Note that the crystalline clusters are composed of different local structures (large spheres in blue, gray, and red), but there seems to be no tendency for a certain type to form a core or surface. Moreover, the clusters are surrounded by pre-structured particles (small green spheres). Although most prominent in the vicinity of solid clusters, these loosely structured regions can be found throughout the suspension. In the strongly sheared case, we observe considerably less pre-structured particles than in the unsheared suspension indicating the shear-induced disruption of a loosely structured fluid.

From pre-structured to crystalline

Once a loosely ordered but still fluid environment is formed, the pre-structured liquid has yet to transform into a crystalline cluster. Hence, the next step is to focus on the influence of shear flow on the second part of the transition from liquid to crystal. We trace the transitions between the pre-structured liquid and

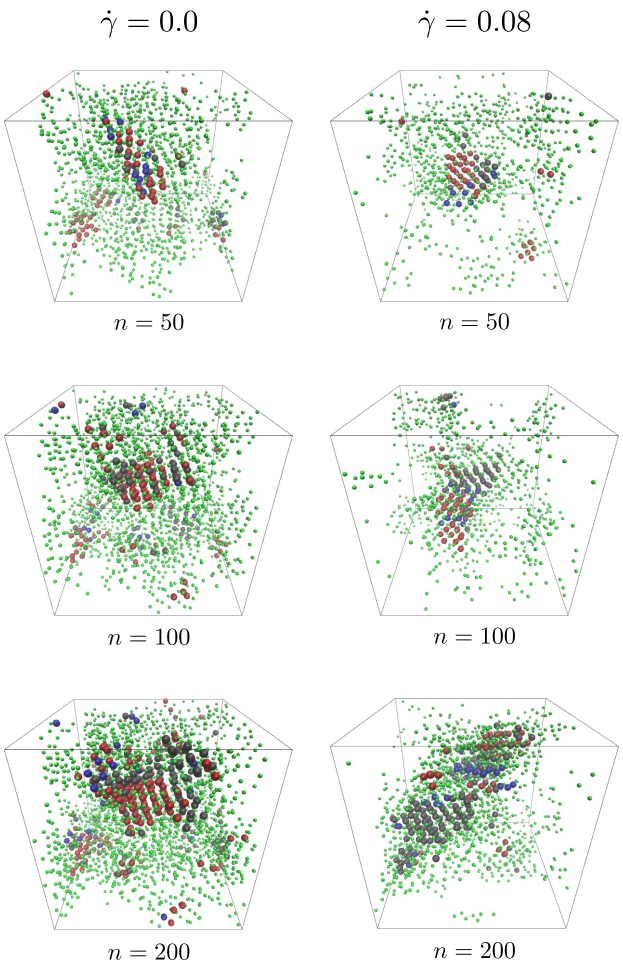

Figure 6.8.: Snapshots of the suspension during the crystallization process for $\dot{\gamma} = 0.0$ (left column) and $\dot{\gamma} = 0.08$ (right column) at three different sizes of the largest cluster n. The large spheres are solid particles with hcp (blue), bcc (gray), and fcc-structured (red) environments. Pre-structured particles are shown as small sphere (green), whereas liquid particles are not shown for clarity.

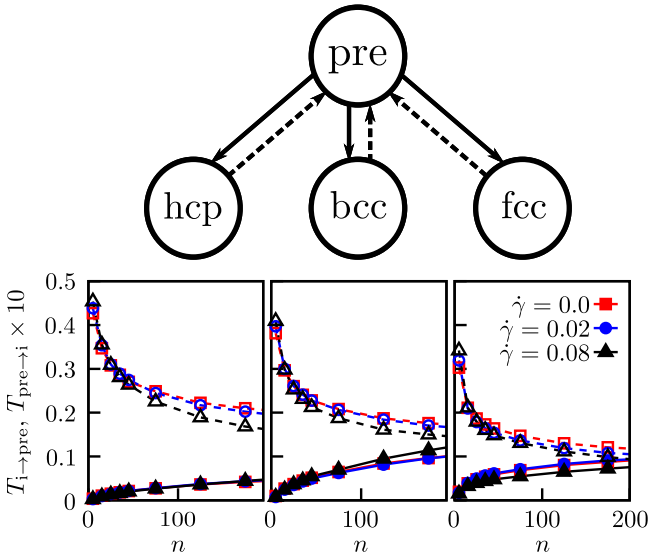

Figure 6.9.: Transfer matrix components for transitions from the pre-structured state to hcp, bcc, and fcc (from left to right, solid lines) scaled by a factor 10 and their corresponding backwards rates (dashed lines) for $\dot\gamma = 0.0$, 0.02, and 0.08. The magnitude of the rates is comparable for the three structures and they are barely affected by the flow field.

the crystalline structures hcp, bcc, and fcc and show the corresponding transfer components $T_{j\to i}$ in Fig. 6.9. Here, the influence of the shear flow is much smaller than for the transitions between liquid and pre-structured. The rates from the crystalline states to the pre-structured one describe the destruction of crystalline clusters. They are not increased by the shear flow but even somewhat reduced. The rates ending in the crystalline states are barely affected by the shearing as well. Hence, even the largest strain rate applied ($\dot\gamma = 0.08$) is not strong enough to destroy or shrink crystalline clusters once they have formed. Thus, the main effect of shear flow on the creation of crystalline clusters is the suppression of the development of a loosely structured environment and not the destruction of existing clusters.

6.4.3. Shear flow enhances growth of clusters

Growth rate

Complementary to Fig. 6.6, we show the growth rate [see Eq. (6.20)] of the largest cluster now for a wider range of cluster sizes $0 \le n \le 1000$, see Fig. 6.10(a). Note that for the larger clusters considered here, we need to increase the time interval over which the change in n is evaluated to $\delta t = 5000\Delta t$ in order to separate the

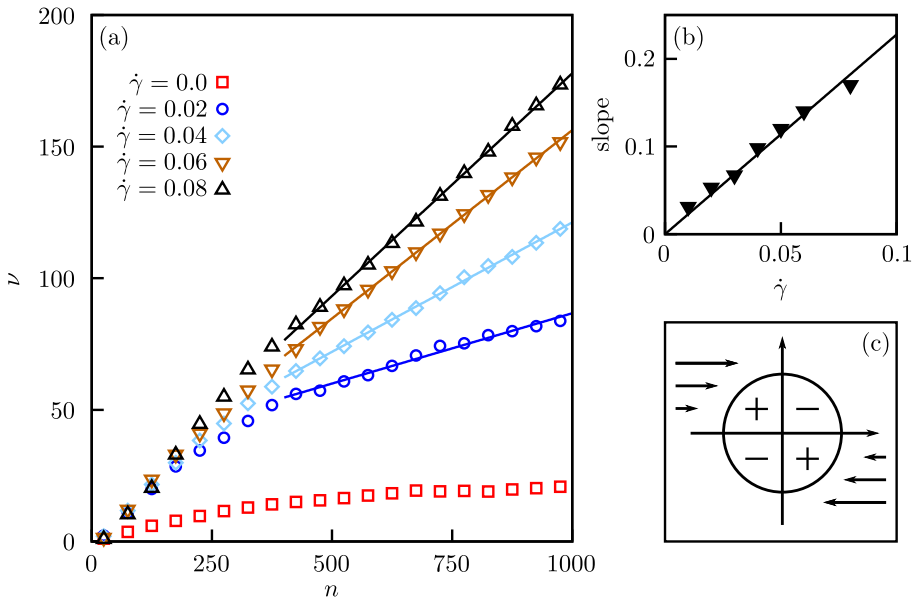

Figure 6.10.: (a) Average growth rate of the largest cluster at fixed n for different strain rates for $\phi = 0.52$. The solid lines are linear fits to the data for $n \geq 400$. (b) Slope of the linear fit functions plotted against the strain rate $\dot\gamma$. The solid line is a linear fit to the slopes crossing the origin. (c) Sketch of the current of liquid particles arriving at the surface of a sphere. Only in the regions marked with "+" liquid particles enter this surface, whereas in regions marked with "-" the particle current is negative.

growth trend from fluctuations. Switching on the flow field enhances the growth rates significantly. For $n \gtrsim 400$, the growth rate is dominated by a linear increase in n. The slope of this linear contribution itself grows proportional to the strain rate, see Fig. 6.10(b). The dominant contribution of the shear flow to the growth rate can thus be condensed in the simple form

$$\nu(n) = B\dot\gamma n, \tag{6.21}$$

where the proportionality constant B is obtained from least-square fits to the data. We find $B = 2.28\pm0.10$ and $B = 2.75\pm0.16$ for $\phi = 0.52$ and $\phi = 0.45$, respectively. This strongly shear-dependent growth rate expresses the rapid crystalline growth in the sheared suspensions as shown in Fig. 6.5(e) on a more systematic level.

Tentative explanation

A growth rate linear in n might arise from convection, which can be understood as follows. We assume that particles in the vicinity of a crystalline nucleus are

more likely to crystallize. Liquid particles move on average with the the local solvent velocity $\dot{\gamma} y \mathbf{e}$, whereas particles in a crystalline cluster move on average with the mean velocity of the cluster. Therefore, particularly in the uppermost and lowermost part of the cluster in y direction, the surrounding liquid particles move at different velocities. In other words, shear flow enhances the number of particles passing through the vicinity of the cluster, see Fig. 6.10(c). We model the surface of this vicinity $\mathcal{S}$ as a sphere of radius R. The shear-induced particle current entering this sphere reads

$$\frac{1}{2}\int_{\mathcal{S}} \rho_l \dot{\gamma} |y \mathbf{e}_x \cdot \mathrm{d}\mathbf{S}| = \frac{4}{3}\rho_l R^3 \dot{\gamma} \propto n\dot{\gamma}, \tag{6.22}$$

with the the number density in the liquid $\rho_l \equiv \pi\phi/6$. The particle current is thus proportional to both the size of the cluster and the strain rate $\dot{\gamma}$. Hence, we obtain Eq. (6.21) with a free parameter B accounting for deviations from the spherical shapes of the clusters and the probability with which particles attach to the cluster.

6.4.4. Restructuring in the solid

A crystalline cluster does not necessarily form in the most stable configuration right at the beginning. Ostwald's step rule [194], which is, strictly speaking, not a universal rule but rather a tendency for nucleation pathways, suggests that crystalline clusters form preferentially in the structure which is closest to the liquid phase in their free energy [195]. Moreover, especially for small clusters, the properties of the surface still play an important role. How the most stable structure looks like can therefore depend on both the shape and the size of the cluster. External influences such as the linear shear flow can affect inter alia these properties and thus also the most likely composition.

Figs. 6.11(a)-(c) show the components of the transfer matrix for the transitions between solid structures. The most prominent effect of the shear flow is that the rates for transitions ending in the bcc configuration are significantly enhanced. Other transitions respond rather weakly to an increased strain rate. The rates towards an hcp structure grow slightly with $\dot{\gamma}$ and for the optimal strain rate $\dot{\gamma} = 0.02$ the likelihood for a transition from bcc to fcc is increased somewhat.

Fig. 6.11(d) shows the average fraction of the three solid structures of all solid particles in the suspension as a function of the largest cluster size n. The largest part of the solid particles belongs to the fcc structure which is the most stable configuration in equilibrium. In consistency with the shear dependence of the transition rates, the fraction of fcc particles is slightly enhanced at the expense of bcc particles for $\dot{\gamma} = 0.02$, while the fraction of hcp particles barely changes. Increasing the strain rate to $\dot{\gamma} = 0.08$, the bcc structure becomes dominant and

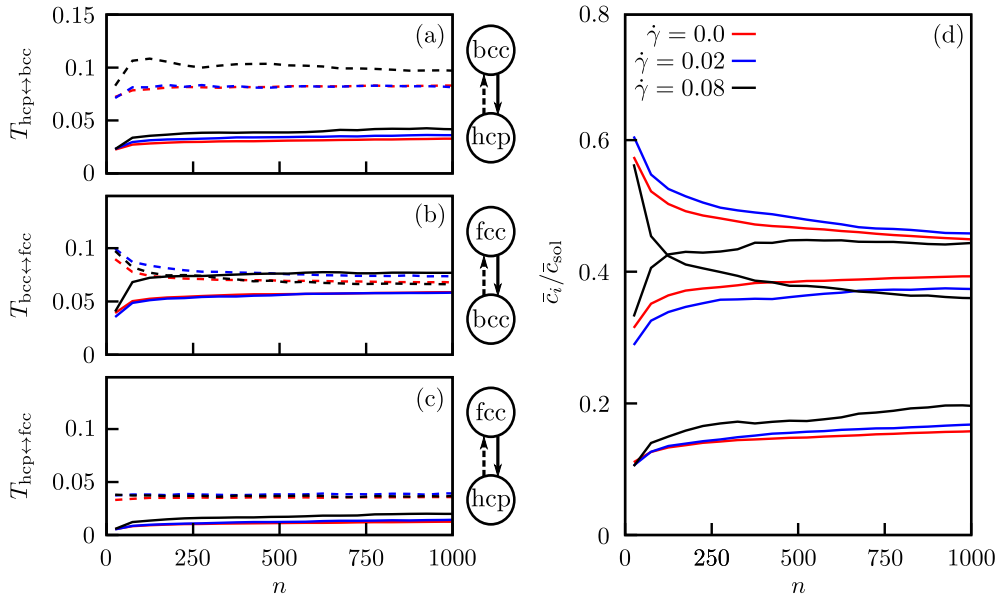

Figure 6.11.: (a)-(c) Transfer matrix components for the transitions between the three solid structures. (a) hcp and bcc, (b) bcc and fcc, and (c) hcp and fcc. (d) Fraction of the solid population $\bar{c}_i/\bar{c}_{\mathrm{sol}}$ in hcp, bcc, and fcc measured in the simulations.

the fraction of fcc particles decreases accordingly, see also Fig. 6.8. If, in the spirit of Ostwald's step rule, bcc is most easily formed from the liquid, then crystalline clusters can grow the faster the more bcc they contain. Since larger strain rates stabilize bcc compared to fcc and hcp, this point might contribute as well to the enhanced cluster growth for these strain rates.

6.5. Conclusion and outlook

In this chapter, we have used Langevin dynamics simulations to investigate the influence of a weak but steady shear flow on the time it takes a highly supersaturated, charge-stabilized colloidal suspension to crystallize. We find an optimal strain rate for which this time exhibits a minimum. We explain this behavior as a consequence of two counteracting, shear-dependent effects influencing the crystallization at different stages in the solidification process. At the nucleation stage, shear flow hampers the formation of small clusters, whereas at the growth stage the shearing enhances the development of the crystal.

In order to investigate these effects in more detail, we employed a discrete state model. With this model, we discussed the transitions between the five relevant

structural configurations in the environment of a single particle. We separated the state space into two fluid states, comprising an entirely liquid configuration and a pre-structured state, and the three crystalline configurations, hcp, bcc, and fcc. In order to obtain meaningful averages respecting the momentary state in the progress of the crystallization, we used the size of the largest cluster n as an order parameter. We averaged the population in the five states and transition rates between them at fixed n. From the latter, we constructed a transfer matrix from which we were able to infer a quasi-stationary state towards which the suspension relaxes. The actual average configuration and the quasi-stationary state coincided to a very good degree implying a time scale separation between the fast transitions between different state and the overall progress of the crystallization.

Analyzing the transition rates, we found that in this system nucleation proceeds via the pre-structured state. Even a weak shear flow, which was not strong enough to destroy existing clusters, disrupted the formation of such a loose ordering in the liquid. Consequently, the probability for the formation of a critical nucleus was significantly lowered. At the growth stage, the flow field accelerated the crystallization process. The functional form of the shear dependence could be explained by a simple convective mechanism. Moreover, the strain rate stabilized the bcc structure compared to hcp and fcc allowing for larger bcc domains in the crystal. If, in the spirit of Ostwald's step rule, bcc is most easily formed, this structural change might contribute to a faster growth as well.

Our data show that the depth of the minimum for the duration of the crystallization process is less pronounced for the smaller volume fraction which entails the question whether there is a lower bound on the density for which this minimum vanishes. How the existence and depth of this minimum depend on the supersaturation remains a topic for future investigation. Another prospect concerns the relative orientation of crystalline planes in the clusters and the direction of the shear flow. According to Butler and Harrowell [36] crystalline planes in clusters should orient parallel to the shear flow, i. e., perpendicular to the shear gradient direction. Yet, for the weak strain rates and the high supersaturation studied here, differently oriented planes do occur. However, "properly" oriented clusters might still be more probable or have larger growth rates. It could also be worthwhile investigating the effect of shearing on cluster breakup and coalescence for this system [42]. There, typical length scales are on the order of cluster diameters instead of particle diameters and thus velocity differences caused by the flow field should play a very prominent role. Furthermore, an essential point for the duration of crystallization processes is the time a system spends in metastable configurations which it must leave before further growth can set in [199]. One could speculate that shearing forces might help the system to overcome such local minima thus providing another mechanism accelerating the solidification process. Therefore, it would

be interesting to study how shear flow affects the sojourn times of a crystallizing system in metastable configurations. Moreover, in order to compare simulation data to experiments, it is necessary to explore the role of hydrodynamics on the crystallization process [200].

A. Mobility tensor for two hydrodynamically interacting spheres

In this section, we compute the mobility tensor for two hydrodynamically interacting, nonrotating spheres in creeping flow along the lines of Ref. [114]. We start by computing the flow field around a single sphere. For creeping flow, the Navier-Stokes equations reduce to the linear Stokes equations

$$\eta \boldsymbol{\nabla}^2 \mathbf{v}(\mathbf{r}) - \boldsymbol{\nabla} p(\mathbf{r}) + \mathbf{f}(\mathbf{r}) = 0 \tag{A.1}$$

$$\boldsymbol{\nabla} \cdot \mathbf{v}(\mathbf{r}) = 0 \tag{A.2}$$

for the fluid velocity $\mathbf{v}(\mathbf{r})$ at position $\mathbf{r}$, the pressure field $p(\mathbf{r})$, and the body force $\mathbf{f}(\mathbf{r})$. Solving this set of equations for a point force $\mathbf{f}(\mathbf{r}) = \mathbf{f}_0\, \delta(\mathbf{r})$ yields the so-called Oseen tensor or Stokeslet

$$\mathsf{G}(\mathbf{r}) = \frac{1}{8\pi\eta r}\left(\mathbb{1} + \frac{\mathbf{r}\mathbf{r}^{\mathrm{T}}}{r^2}\right) \tag{A.3}$$

with $r \equiv |\mathbf{r}|$. The pressure field is given by

$$p(\mathbf{r}) = -\boldsymbol{\nabla} \cdot \left(\frac{\mathbf{f}_0}{4\pi r}\right). \tag{A.4}$$

With the body forces $\mathbf{f}(\mathbf{r})$ on the surface $\mathcal{S}$ of an arbitrary rigid structure in an unbounded medium, we describe the velocity of the surrounding fluid by the surface integral

$$\mathbf{v}(\mathbf{r}) = \int_{\mathcal{S}} \mathsf{G}(\mathbf{r} - \mathbf{r}')\mathbf{f}(\mathbf{r}')\mathrm{d}\mathcal{S}. \tag{A.5}$$

As this integral is generally not tractable analytically, one often resorts to a multipole expansion. Yet, for a sphere, symmetry allows for an exact result. We obtain [96]

$$\mathbf{v}(\mathbf{r}) = \left(1 + \frac{a^2}{24}\boldsymbol{\nabla}^2_{\mathbf{r}_0}\right) \mathsf{G}(\mathbf{r} - \mathbf{r}_0)\, \mathbf{F} \tag{A.6}$$

for a spherical particle of diameter a centered at $\mathbf{r}_0$ with the total force $\mathbf{F} = \int_{\mathcal{S}} \mathbf{f}(\mathbf{r}')\mathrm{d}\mathcal{S}$ exerted on the particle. By using no-slip boundary conditions and Eq.(A.6), we deduce the Stokes law for the velocity of a sphere dragged through the solvent by a force $\mathbf{F}$

$$\mathbf{v}^{\mathrm{S}} = \frac{1}{\pi a^2}\int_{\mathcal{S}} \mathbf{v}(\mathbf{r})\mathrm{d}\mathcal{S} = \frac{1}{3\pi\eta a}\mathbf{F}. \tag{A.7}$$

Let us now consider two such spherical particles in an unbounded fluid. To the ith and the jth particle, we apply the external forces $\mathbf{F}_i$ and $\mathbf{F}_j$, respectively. The velocity field accompanying the motion of particle i is then affected by the motion of particle j. In principle, the altered velocity field of particle i in turn modifies the velocity field of particle j and so forth. Assuming, however, that the particle distance is much larger than their diameter, i. e., $a/r_{ij} \ll 1$, we can neglect such higher order effects. The resulting velocity of particle i then reads

$$\mathbf{v}_i^{\mathrm{S}} = \frac{1}{3\pi\eta a}\mathbf{F}_i + \frac{1}{\pi a^2}\int_{\mathcal{S}_i} \mathbf{v}_j(\mathbf{r})\mathrm{d}\mathcal{S}_i. \tag{A.8}$$

The second term on the right-hand side is given by the velocity field of particle j on the surface of particle i, while the first term is simply the Stokes friction contribution. Introducing the mobility tensor μ_{ij}, we write [114]

$$\mathbf{v}_i^{\mathrm{S}} \equiv \sum_j \mu_{ij}\mathbf{F}_j \tag{A.9}$$

with

$$\mu_{ii} \equiv \frac{1}{3\pi\eta a}\mathbb{1} = \mu_0\mathbb{1}, \tag{A.10}$$

$$\begin{aligned}\mu_{ij} &\equiv \frac{1}{8\pi\eta a}\frac{a}{r_{ij}}\left(\mathbb{1} + \frac{\mathbf{r}_{ij}\mathbf{r}_{ij}^T}{r_{ij}^2}\right) + \frac{1}{12\pi\eta a}\left(\frac{a}{r_{ij}}\right)^3\left(\mathbb{1} - 3\frac{\mathbf{r}_{ij}\mathbf{r}_{ij}^T}{r_{ij}^2}\right)\\ &= \frac{3}{8}\mu_0\frac{a}{r_{ij}}\left(\mathbb{1} + \frac{\mathbf{r}_{ij}\mathbf{r}_{ij}^T}{r_{ij}^2}\right) + \frac{1}{4}\mu_0\left(\frac{a}{r_{ij}}\right)^3\left(\mathbb{1} - 3\frac{\mathbf{r}_{ij}\mathbf{r}_{ij}^T}{r_{ij}^2}\right) \quad \text{for} \quad i \neq j.\end{aligned} \tag{A.11}$$

This approximation for the mobility is also known as the Rotne-Prager tensor [113]. It can also be applied for colloidal suspensions consisting of many particles if the suspension is sufficiently dilute.

B. Multiplicative Noise

Dealing with Langevin equations involving a spatially inhomogeneous diffusion coefficient requires caution in the interpretation of integrals. Along the lines of Lau and Lubensky [102], we will illustrate and solve this problem for the Langevin equation,

$$\dot{x} = f(x) + g(x)\eta(t), \tag{B.1}$$

describing a particle at position x with an additional drift f and the normalized Gaussian white noise η with zero mean and correlations $\langle \eta(t)\eta(t')\rangle = \delta(t-t')$. A spatially varying diffusion coefficient $D(x)$ is introduced through the multiplicative factor $g(x) \equiv [2D(x)]^{1/2}$ modifying the magnitude of the normalized noise.

The difficulty in dealing with this multiplicative noise term boils down to the interpretation of the integral

$$\mathcal{I}(t, \Delta t) \equiv \int_t^{t+\Delta t} g(x(\tau))\eta(\tau)\mathrm{d}\tau. \tag{B.2}$$

If both g and η were continuous functions, the integral mean-value theorem would imply that any approximation

$$\mathcal{I}^\alpha(t, \Delta t) \equiv g(x^\alpha) \int_t^{t+\Delta t} \eta(\tau)\mathrm{d}\tau \tag{B.3}$$

with $x^\alpha \equiv (1-\alpha)x(t)+\alpha x(t+\Delta t)$ for $\alpha \in [0,1]$ would converge to the unique value $g(x(t))\eta(t)$ in the limit $\Delta t \to 0$. The noise η, however, is a stochastically fluctuating quantity and hence discontinuous in time. Therefore, the integral mean-value theorem does not hold. In fact, approximations of the form (B.3) converge to different values for different choices of α [10,11]. For any stochastic integral including multiplicative noise, it is therefore crucial to define the type of the underlying discretization, i. e., to define α. Typical choices are the Îto-convention ($\alpha = 0$) and the Stratonovich-convention ($\alpha = 1/2$) [10].

However, from a physical point of view, the dynamics is unique, which takes us to the core of the problem. There is only one choice for α for which Eq. (B.1) leads to the Boltzmann distribution in the long-time limit. In order to obtain the α dependence of the steady-state solution of Eq. (B.1), we derive the corresponding

Fokker-Planck equation from the Kramers-Moyal expansion, see Section 2.3. To this end, we compute the first and second moment for the displacement $\Delta x \equiv x(t+\Delta t) - x(t)$ in the time interval Δt and use Eqs. (2.12), (2.13), and (2.14). Integrating Eq. (B.1) yields

$$\begin{aligned}\Delta x \equiv x(t+\Delta t) - x(t) &= \int_t^{t+\Delta t} \{f[x(\tau)] + g[x(\tau)]\eta(\tau)\}\,\mathrm{d}\tau \\ &= f[x(t)+\alpha\Delta x]\Delta t + g[x(t)+\alpha\Delta x]\int_t^{t+\Delta t}\eta(\tau)\mathrm{d}\tau, \quad \text{(B.4)}\end{aligned}$$

from which we obtain

$$\langle \Delta x\rangle = f(x(t))\Delta t + \alpha g(x(t))\partial_x g(x(t))\Delta t, \quad \text{(B.5)}$$

$$\left\langle (\Delta x)^2\right\rangle = g(x(t))^2\Delta t, \quad \text{(B.6)}$$

up to first order in Δt, where we used that $\int_t^{t+\Delta t}\eta(\tau)\mathrm{d}\tau$ is statistically of the order $(\Delta t)^{1/2}$ [11]. The resulting Fokker-Planck equation is therefore

$$\begin{aligned}\partial_t\Psi(x,t) &= -\partial_x[f(x) + \alpha g(x)\partial_x g(x)]\Psi(x,t) + \partial_x^2 g(x)^2\Psi(x,t)/2 \quad \text{(B.7)}\\ &= -\partial_x[f(x) - (1-\alpha)\partial_x D(x)]\Psi(x,t) + \partial_x D(x)\partial_x\Psi(x,t). \quad \text{(B.8)}\end{aligned}$$

The long-time solution of this equation is the Boltzmann distribution $\Psi(x) \propto \exp\{-U(x)/T\}$ with the internal energy U if and only if

$$f(x) = f^{(0)}(x) + d^{(\alpha)}(x) \quad \text{(B.9)}$$

with the regular drift $f^{(0)}(x) \equiv -g(x)^2\partial_x U(x)/(2T) = -D(x)\partial_x U(x)/T$ and an additional spurious drift

$$d^{(\alpha)}(x) \equiv (1-\alpha)g(x)\partial_x g(x) = (1-\alpha)\partial_x D(x). \quad \text{(B.10)}$$

This result implies that, beside the usual conservative force the drift term f, Eq. (B.1) must include an additional α dependent drift term $d^{(\alpha)}$ if we require the long-time distribution to be the Boltzmann distribution. The spurious drift vanishes if either $D(x) = \text{const.}$, i. e., without multiplicative noise, or if we choose the isothermal convention $\alpha = 1$ [102]. Generalizing this result to N degrees of freedom, the spurious drift becomes

$$\mathbf{d}^{(\alpha)} = (1-2\alpha)\boldsymbol{\nabla}\cdot\mathsf{D}(x) + \alpha[\boldsymbol{\nabla}\cdot\mathsf{G}(x)]\mathsf{G}(x) \quad \text{(B.11)}$$

with the diffusion matrix $\mathsf{D}(x) \equiv \mathsf{G}^2(x)/2$, $\mathsf{G}^T(x) = \mathsf{G}(x)$ and with $x \equiv (x_1, \ldots, x_N)$ denoting the entire set of degrees of freedom.

C. Response and noise-correlation

We consider a system described by a set of n coupled Langevin equations

$$\dot{x}_i = g_i(\mathbf{x}) + \mu_0 h_i + \zeta_i \quad \text{for} \quad i \in \{0, \ldots, n\} \tag{C.1}$$

with arbitrary functions g_i depending on the entire configuration $\mathbf{x} \equiv (x_1, \ldots, x_n)$, small perturbation forces $\mathbf{h} \equiv (h_1, \ldots, h_n)$ and Gaussian white noise $\boldsymbol{\zeta} \equiv (\zeta_1, \ldots, \zeta_n)$. The stochastic path weight reads

$$P[\boldsymbol{\zeta}(t); \mathbf{h}(t)] = \mathcal{N} \exp\left\{ -\frac{1}{4D_0} \int \boldsymbol{\zeta}^2(t) \mathrm{d}t \right\} \tag{C.2}$$

reproducing the properties discussed in Section 2.2, i. e., zero mean and correlations as defined in Eq. (2.6).

The components of the linear response of an observable $\mathbf{A} \equiv (A_1, \ldots, A_n)$ to a small external perturbation $\mathbf{h}$ is defined as the functional derivative

$$R_{ij}(t, t') \equiv \left. \frac{\delta \langle A_i(t) \rangle_h}{\delta h_j(t')} \right|_{h=0} \tag{C.3}$$

of the average value of the observable $\langle A_i(t) \rangle_h$ in the perturbed system with respect to the perturbation at a different time t'. Causality requires $R_{ij}(t, t') \propto \theta(t - t')$, where $\theta(\tau) = 1$ for $\tau > 0$ and zero otherwise.

In the Langevin equation (C.1), a shift in the noise ζ_i is equivalent to a small perturbation h_i. For $t > t'$, we can therefore write

$$\begin{aligned} T R_{ij}(t, t') = \mu_0 T \frac{\delta \langle A_i(t) \rangle}{\delta \zeta_j(t')} &= \mu_0 T \left\langle \int \mathrm{d}\boldsymbol{\zeta} \frac{\delta A_i(t)}{\delta \zeta_j(t')} P[\boldsymbol{\zeta}(t)] \right\rangle \\ &= -\mu_0 T \left\langle \int \mathrm{d}\boldsymbol{\zeta} A_i(t) \frac{\delta P[\boldsymbol{\zeta}(t)]}{\delta \zeta_i(t')} \right\rangle = \langle A_i(t) \zeta_j(t') \rangle / 2, \end{aligned} \tag{C.4}$$

after partial integration in the third step and using both the Einstein relation and Eq. (C.2) [18, 100]. For underdamped dynamics, an analogous calculation yields

$$T R_{ij}(t, t') = \mu_0 \langle A_i(t) \xi_j(t') \rangle / 2. \tag{C.5}$$

D. Green's function for a trapped particle in shear flow

The set of coupled Langevin equations (5.15) for the harmonic potential Eq. (5.24) can be written in the compact form

$$\dot{\mathbf{x}} = \mathsf{A}\mathbf{x} + (0, 0, \xi_x, \xi_y)^{\mathrm{T}} \tag{D.1}$$

with $\mathbf{x} \equiv (x, y, v_x, v_y)^{\mathrm{T}}$ and

$$\mathsf{A} = \frac{1}{m} \begin{pmatrix} 0 & 0 & m & 0 \\ 0 & 0 & 0 & m \\ -k & \dot{\gamma} & -1 & 0 \\ 0 & -k & 0 & -1 \end{pmatrix}. \tag{D.2}$$

The Green's function for this stochastic differential equation is

$$\mathsf{G}(t) \equiv e^{\mathsf{A}t} = \begin{pmatrix} \mathsf{G}^{rr}(t) & \mathsf{G}^{rv}(t) \\ \mathsf{G}^{vr}(t) & \mathsf{G}^{vv}(t) \end{pmatrix}. \tag{D.3}$$

Explicitly, the four submatrices are given by

$$\mathsf{G}^{rr}(t) = e^{-t/(2m)} \left[\left(\cos\omega t + \frac{\sin\omega t}{2m\omega} \right) \mathbb{1} + \dot{\gamma} g_{rr}(t) \mathbb{1}_{xy} \right], \tag{D.4}$$

$$\mathsf{G}^{rv}(t) = e^{-t/(2m)} \left[\frac{\sin\omega t}{\omega} \mathbb{1} + \dot{\gamma} g_{rv}(t) \mathbb{1}_{xy} \right], \tag{D.5}$$

$$\mathsf{G}^{vr}(t) = e^{-t/(2m)} \left[-\left(\omega + \frac{1}{4m^2\omega} \right) \sin\omega t \mathbb{1} + \dot{\gamma} g_{vr}(t) \mathbb{1}_{xy} \right], \tag{D.6}$$

$$\mathsf{G}^{vv}(t) = e^{-t/(2m)} \left[\left(\cos\omega t - \frac{\sin\omega t}{2m\omega} \right) \mathbb{1} + \dot{\gamma} g_{vv}(t) \mathbb{1}_{xy} \right], \tag{D.7}$$

$$\tag{D.8}$$

with

$$\omega \equiv \frac{\sqrt{4km - 1}}{2m}, \quad \mathbb{1}_{xy} \equiv \begin{pmatrix} 0 & 1 \\ 0 & 0 \end{pmatrix} \tag{D.9}$$

and

$$g_{rr}(t) \equiv \frac{(2m\omega^2 t + 1)\sin\omega t - \omega t\cos\omega t}{4m^2\omega^3}, \tag{D.10}$$

$$g_{rv}(t) \equiv \frac{\sin\omega t - \omega t\cos\omega t}{2m\omega^3}, \tag{D.11}$$

$$g_{vr}(t) \equiv \frac{(4m^2\omega^2 - 1)\sin\omega t + (4m^2\omega^2 + 1)\omega t\cos\omega t}{8m^3\omega^3}, \tag{D.12}$$

$$g_{vv}(t) \equiv \frac{(2m\omega^2 t - 1)\sin\omega t + \omega t\cos\omega t}{4m^2\omega^3}. \tag{D.13}$$

The stationary distribution

$$\Psi(\mathbf{x}) = \frac{1}{(2\pi)^2\sqrt{\det\mathsf{M}}}\exp\left\{-\frac{1}{2}\mathbf{x}^{\mathrm{T}}\mathsf{M}^{-1}\mathbf{x}\right\} \tag{D.14}$$

is Gaussian with zero mean and thus determined by the symmetric covariance matrix

$$\mathsf{M} \equiv \begin{pmatrix} \langle\mathbf{r}\mathbf{r}^{\mathrm{T}}\rangle & \langle\mathbf{v}\mathbf{r}^{\mathrm{T}}\rangle \\ \langle\mathbf{v}\mathbf{r}^{\mathrm{T}}\rangle & \langle\mathbf{v}\mathbf{v}^{\mathrm{T}}\rangle \end{pmatrix}. \tag{D.15}$$

Using Chandrasekhar's theorem [96], we can compute M from the above Green's functions

$$\mathsf{M} = \frac{2}{m^2}\int_0^\infty \begin{pmatrix} \mathsf{G}^{rv}(t)\mathsf{G}^{rv\mathrm{T}}(t) & \mathsf{G}^{rv}(t)\mathsf{G}^{vv\mathrm{T}}(t) \\ \mathsf{G}^{vv}(t)\mathsf{G}^{rv\mathrm{T}}(t) & \mathsf{G}^{vv}(t)\mathsf{G}^{vv\mathrm{T}}(t) \end{pmatrix}\mathrm{d}t. \tag{D.16}$$

With $1 + 4(m\omega)^2 = 4km$, we obtain the stationary correlations

$$\langle\mathbf{r}\mathbf{r}^{\mathrm{T}}\rangle = \frac{1}{k}\mathbb{1} + \frac{1}{2k^2}\begin{pmatrix} \frac{1+km}{k}\dot\gamma^2 & \dot\gamma \\ \dot\gamma & 0 \end{pmatrix}, \tag{D.17}$$

$$\langle\mathbf{r}\mathbf{v}^{\mathrm{T}}\rangle = \langle\mathbf{v}\mathbf{r}^{\mathrm{T}}\rangle^{\mathrm{T}} = \frac{1}{2k}\begin{pmatrix} 0 & -\dot\gamma \\ \dot\gamma & 0 \end{pmatrix}, \tag{D.18}$$

$$\langle\mathbf{v}\mathbf{v}^{\mathrm{T}}\rangle = \frac{1}{m}\mathbb{1} + \frac{1}{2k}\begin{pmatrix} \dot\gamma^2 & 0 \\ 0 & 0 \end{pmatrix}. \tag{D.19}$$

E. Approximately time-independent FDR

We estimate the range of the parameters k and $\dot{\gamma}$ for which the FDR corresponding to the FDT in Eq. (5.31) becomes approximately independent of time. Since it is only the additive correction term in Eq. (5.31) that prevents this time-independence, we need to find the regime where its magnitude becomes small compared to the first part, i. e.,

$$\theta_x |R_{xx}(t)| = (\theta_x/m)|G^{vv}_{xx}(t)| \gg \langle y v_x \rangle \, |G^{vr}_{xy}(t)|. \tag{E.1}$$

We focus on the case $km \gtrsim 1$[1] for oscillatory motion of the trapped particle with frequency $\omega \approx \sqrt{k/m}$. Using the explicit expressions for the Green's functions given in Appendix D, the condition reduces to

$$\theta/m \gg \langle y v_x \rangle \, \dot{\gamma} |g_{vr}(t)|. \tag{E.2}$$

For short times, we have $\sin \omega t \approx \omega t$ and $\cos \omega t \approx 1$ the function $g_{vr}(t)$, see Eq. (D.12), is dominated by $1/m$. Hence, we find an approximately time-independent FDR if

$$1 + m\dot{\gamma}^2/(2k) \gg \dot{\gamma}^2/(2k), \tag{E.3}$$

where we have substituted Eq. (5.30) for θ_x and Eq. (D.18) for the moment. For large masses, $m \gg 1$, this condition is fulfilled if $k \gg m\dot{\gamma}^2$, while for $m \lesssim 1$, it requires $k \gg \dot{\gamma}^2$, where we drop all numerical factors. Hence, we have $k \gg \max\{\dot{\gamma}^2, m\dot{\gamma}^2\}$.

The kinetic temperature θ_x requires $k \gg m\dot{\gamma}^2$ to be much larger than the equilibrium value. We therefore find a gap between the two conditions for low masses, i. e., we can either have a time-independent FDR or a kinetic temperature larger than one. For increasing mass, this gap becomes smaller, and for $m \gtrsim 1$, the regimes are adjoint to each other, see Fig. E.1. Close to the borderline, we can find both properties realized simultaneously, i. e., an approximately constant FDR and $\theta_x > 1$.

[1] For $km \lesssim 1$, an analogous discussion is possible.

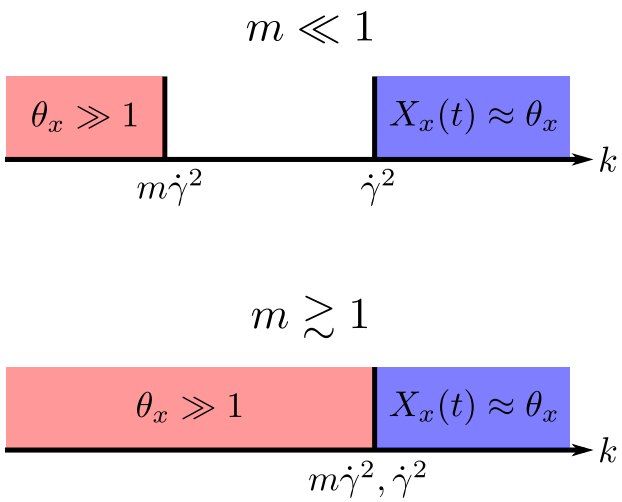

Figure E.1.: Sketch of the regimes in which the FDR is approximately constant (blue) and in which the kinetic temperature is much larger than one (red). For low masses, there is a gap between the two regimes, while for masses $m \gtrsim 1$ they are adjoint.

F. Simulation details

F.1. Stochastic velocity Verlet algorithm

We integrate the coupled set of Langevin equations,

$$\dot{\mathbf{r}}_i = \mathbf{v}_i, \tag{F.1}$$

$$m_i \dot{\mathbf{v}}_i = -\boldsymbol{\nabla}_i U - [\mathbf{v}_i - \mathbf{u}(\mathbf{r}_i)] + \boldsymbol{\xi}_i \equiv \tilde{\mathbf{F}}_i, \tag{F.2}$$

by employing a simple extension of the velocity Verlet scheme [152] similar to the BKK[1] integrator [201]. We start by initializing the particle positions on a regular lattice and setting all velocities to zero. Then, we compute the initial total force $\tilde{F}_i$ acting on each particle from the initial positions and velocities, see Fig. F.1. The stochastic contribution to the total forces is provided by a random-number generator creating normally distributed numbers with zero mean and variance $2/\Delta t$ with the time step $\Delta t = 5 \times 10^{-4}$. After the initialization, we propagate the velocities for half a time step

$$\mathbf{v}_i(t + \Delta t/2) = \mathbf{v}_i(t) + \tilde{\mathbf{F}}_i(t)/(2m_i)\Delta t \tag{F.3}$$

and use these velocities to compute the new set of positions

$$\mathbf{r}_i(t + \Delta t) = \mathbf{r}_i(t) + \mathbf{v}_i(t + \Delta t/2)\Delta t. \tag{F.4}$$

Then, we update the total forces using the momentary positions and velocities and complete the cycle by propagating the velocities for another half time step

$$\mathbf{v}_i(t + \Delta t) = \mathbf{v}_i(t + \Delta t/2) + \tilde{\mathbf{F}}_i(t + \Delta t)/(2m_i)\Delta t. \tag{F.5}$$

For an efficient computation of the pair interaction, we exploit the exponential decay of the potential: we neglect forces stemming from particles with a displacement larger than $\mathbf{r}_c = 2$ and use a Verlet list to efficiently keep track of the distances [189].

[1] named after Brünger, Brooks, and Karplus

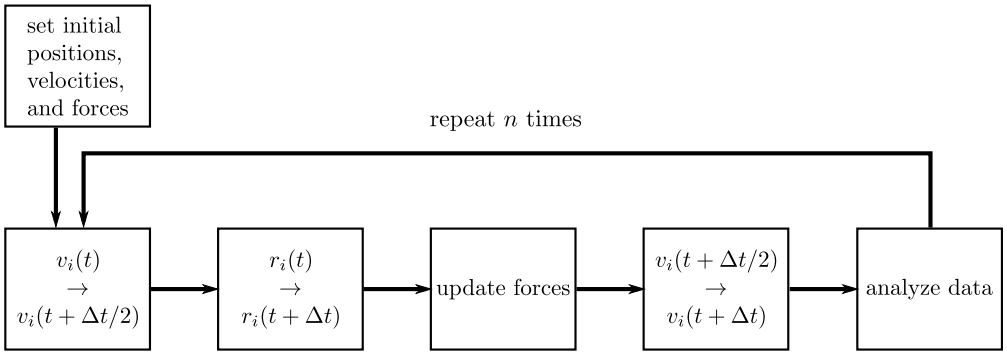

Figure F.1.: Schematic depiction of the employed stochastic velocity Verlet algorithm.

F.2. Implementation of the hard shell

The interaction between the colloidal particles comprises a weak repulsion and a hard core, see Eq. (5.38). However, a hard shell cannot be incorporated in a continuous interaction potential. Also, modeling the hard core by a very steep but continuous potential increase is difficult since requires very small time steps to keep the simulation stable. We evade this problem by employing the following simple algorithm, see Refs. [153, 202] and references therein.

We start by moving every particle ignoring their hard shells. After every particle has been moved, but before new forces are calculated, we detect all particle pairs with overlapping cores. For each overlapping particle pair, we move both particles backwards in time along their respective velocity vector up to the point where their collision took place. Knowing the positions and velocities at the impact, we can infer the correct coordinates at the end of the time step from momentum and energy conservation. We assign the respective correct position and velocity to both particles and repeat this procedure until there are no overlapping pairs left.

Bibliography

[1] F. Ritort. The nonequilibrium thermodynamics of small systems. *C. R. Physique*, 8:528–539, 2007.

[2] K. Sekimoto. Kinetic characterisation of heat bath and the energetics of thermal ratchet models. *J. Phys. Soc. Jpn.*, 66:1234–1237, 1997.

[3] U. Seifert. Entropy production along a stochastic trajectory and an integral fluctuation theorem. *Phys. Rev. Lett.*, 95:040602, 2005.

[4] A. Ashkin. Acceleration and trapping of particles by radiation pressure. *Phys. Rev. Lett.*, 24:156, 1970.

[5] A. Ashkin, J. M. Dziedzic, J. E. Bjorkholm, and S. Chu. Observation of a single-beam gradient force optical trap for dielectric particles. *Opt. Lett.*, 11:288, 1986.

[6] G. Binnig, C. F. Quate, and C. Gerber. Atomic force microscope. *Phys. Rev. Lett.*, 56:930, 1986.

[7] G. M. Wang, E. M. Sevick, E. Mittag, D. J. Searles, and D. J. Evans. Experimental demonstration of violations of the second law of thermodynamics for small systems and short time scales. *Phys. Rev. Lett.*, 89:050601, 2002.

[8] V. Blickle, T. Speck, L. Helden, U. Seifert, and C. Bechinger. Thermodynamics of a colloidal particle in a time-dependent nonharmonic potential. *Phys. Rev. Lett.*, 96:070603, 2006.

[9] R. J. Hunter. *Foundations of Colloid Science*. Oxford University Press, 2001.

[10] H. Risken. *The Fokker-Planck Equation*. Springer-Verlag, Berlin, 2nd edition, 1989.

[11] C. W. Gardiner. *Handbook of Stochastic Methods*. Springer-Verlag, Berlin, 3rd edition, 2004.

[12] N. G. van Kampen. *Stochastic Processes in Physics and Chemistry*. North-Holland, Amsterdam, 1981.

[13] M. Chaichian and A. Demichev. *Path integrals in physics. Volume I: Stochastic processes and quantum mechanics*. Institute of Physics publishing, Bristol and Philadelphia, 2001.

[14] T. Harada and S. Sasa. Energy dissipation and violation of the fluctuation-response relation in nonequilibrium Langevin systems. *Phys. Rev. E*, 73:026131, 2006.

[15] B. Lander, J. Mehl, V. Blickle, C. Bechinger, and U. Seifert. Noninvasive measurement of dissipation in colloidal systems. *Phys. Rev. E*, 86:030401(R), 2012.

[16] J. Mehl, B. Lander, C. Bechinger, V. Blickle, and U. Seifert. Role of hidden slow degrees of freedom in the fluctuation theorem. *Phys. Rev. Lett.*, 108:220601, 2012.

[17] L. F. Cugliandolo. The effective temperature. *J. Phys. A Math. Theor.*, 44:483001, 2011.

[18] T. Speck and U. Seifert. Restoring a fluctuation-dissipation theorem in a nonequilibrium steady state. *Europhys. Lett.*, 74:391, 2006.

[19] M. Baiesi, C. Maes, and B. Wynants. Fluctuations and response of nonequilibrium states. *Phys. Rev. Lett.*, 103:010602, 2009.

[20] U. Seifert and T. Speck. Fluctuation-dissipation theorem in nonequilibrium steady states. *EPL*, 89:10007, 2010.

[21] V. Blickle, T. Speck, C. Lutz, U. Seifert, and C. Bechinger. Einstein relation generalized to nonequilibrium. *Phys. Rev. Lett.*, 98:210601, 2007.

[22] J. R. Gomez-Solano, A. Petrosyan, S. Ciliberto, R. Chetrite, and K. Gawedzki. Experimental verification of a modified fluctuation-dissipation relation for a micron-sized particle in a nonequilibrium steady state. *Phys. Rev. Lett.*, 103:040601, 2009.

[23] J. Mehl, V. Blickle, U. Seifert, and C. Bechinger. Experimental accessibility of generalized fluctuation-dissipation relations for nonequilibrium steady states. *Phys. Rev. E*, 82:032401, 2010.

[24] L. Berthier and J.-L. Barrat. Nonequilibrium dynamics and fluctuation-dissipation relation in a sheared fluid. *J. Chem. Phys.*, 116:6228, 2002.

[25] L. Berthier and J.-L. Barrat. Shearing a glassy material: Numerical tests of nonequilibrium mode-coupling approaches and experimental proposals. *Phys. Rev. Lett.*, 89:095702, 2002.

[26] B. Lander, U. Seifert, and T. Speck. Effective confinement as origin of the equivalence of kinetic temperature and fluctuation-dissipation ratio in a dense shear driven suspension. *Phys. Rev. E*, 85:021103, 2012.

[27] B. Lander, U. Seifert, and T. Speck. Mobility and diffusion of a tagged particle in a driven colloidal suspension. *Europhys. Lett.*, 92(58001), 2010.

[28] B. J. Ackerson and P. N. Pusey. Shear-induced order in suspensions of hard spheres. *Phys. Rev. Lett.*, 61:1033–1036, 1988.

[29] Y. D. Yan, J. K. G. Dhont, C. Smits, and H. N. W. Lekkerkerker. Oscillatory-shear-induced order in nonaqueous dispersions of charged colloidal spheres. *Physica A*, 202:68, 1994.

[30] M. D. Haw, W. C. K. Poon, and P. N. Pusey. Direct observation of oscillatory-shear-induced order in colloidal suspensions. *Phys. Rev. E*, 57:6859–6864, 1998.

[31] R. M. Amos, J. G. Rarity, P. R. Tapster, T. J. Shepherd, and S. C. Kitson. Fabrication of large-area face-centered-cubic hard-sphere colloidal crystals by shear alignment. *Phys. Rev. E*, 61(3):2929–2935, 2000.

[32] P. Panine, T. Naranyan, J. Vermant, and J. Mewis. Structure and rheology during shear-induced crystallization of latex suspensions. *Phys. Rev. E*, 66:022401, 2002.

[33] A. V. Mokshin and J.-L. Barrat. Shear-induced crystallization of an amorphous system. *Phys. Rev. E*, 77:021505, 2008.

[34] A. Nikoubashman, G. Kahl, and C. N. Likos. Cluster crystal under shear. *Phys. Rev. Lett.*, 107:068302, 2011.

[35] T. Palberg, W. Mönch, J. Schwarz, and P. Leiderer. Grain size control in polycrystalline colloidal solids. *J. Chem. Phys.*, 102:5082, 1995.

[36] S. Butler and P. Harrowell. Kinetics of crystallization in a shearing colloidal suspension. *Phys. Rev. E*, 52:6, 1995.

[37] R. Blaak, S. Auer, D. Frenkel, and H. Löwen. Crystal nucleation of colloidal suspensions under shear. *Phys. Rev. Lett.*, 93(6), 2004.

[38] P. Holmqvist, M. P. Lettinga, J. Buitenhuis, and J. K. G. Dhont. Crystallization kinetics of colloidal spheres under stationary shear flow. *Langmuir*, 21:10976, 2005.

[39] Y. L. Wu, D. Derks, A. van Blaaderen, and A. Imhof. Melting and crystallization of colloidal hard-sphere suspensions under shear. *Proc. Natl. Acad. Sci. U.S.A.*, 106:10564, 2009.

[40] A. Penkova, W. Pan, F. Hodjaouglu, and P. G. Vekilov. Nucleation of protein crystals under the influence of solution shear flow. *Ann. N. Y. Acad. Sci.*, 1077:214, 2006.

[41] J. J. Cerdà, T. Sintes, C. Holm, C. M. Sorensen, and A. Chakrabarti. Shear effects on crystal nucleation in colloidal suspensions. *Phys. Rev. E*, 78:031403, 2008.

[42] R. J. Allen, C. Valeriani, S. Tanase-Nicola, P. R. ten Wolde, and D. Frenkel. Homogeneous nucleation under shear in a two-dimensional Ising model: Cluster growth, coalescence and breakup. *J. Chem. Phys.*, 129:134704, 2008.

[43] A. V. Mokshin and J.-L. Barrat. Crystal nucleation and cluster-growth kinetics in a model glass under shear. *Phys. Rev. E*, 82:021505, 2010.

[44] B. Lander, U. Seifert, and T. Speck. Crystallization in a sheared colloidal suspension. *J. Chem. Phys. (accepted).*

[45] C. Bustamante, J. Liphardt, and F. Ritort. The nonequilibrium thermodynamics of small systems. *Physics Today*, 58(7):43, 2005.

[46] V. Blickle and C. Bechinger. Realization of a micrometre-sized stochastic heat engine. *Nature Phys.*, 8:143, 2012.

[47] B. Kongtragool and S. Wongwises. A review of solar-powered Stirling engines and low temperature differential Stirling engines. *Renewable and Sustainable Energy Reviews*, 7(2):131 – 154, 2003.

[48] H. Löwen. Melting, freezing and colloidal suspensions. *Phys. Rep.*, 237:249, 1994.

[49] W. B. Russel, D. A. Saville, and W. R. Schowalter. *Colloidal Dispersions.* Cambridge University Press, 1995.

[50] A. Yethiraj and A. van Blaaderen. A colloidal model system with an interaction tunable from hard sphere to soft and dipolar. *Nature*, 421(6922):513–517, 2003.

[51] J. Mehl. *Getriebene kolloidale Teilchen*. PhD thesis, Universität Stuttgart, 2013.

[52] U. Seifert. Stochastic thermodynamics: Principles and perspectives. *Eur. Phys. J. B*, 64:423–431, 2008.

[53] U. Seifert. *Stochastic Thermodynamics*. Lecture Notes: Soft Matter, From Synthetic to Biological Materials, 2008.

[54] U. Seifert. Stochastic thermodynamics, fluctuation theorems, and molecular machines. *Rep. Prog. Phys.*, 75:126001, 2012.

[55] R. Yasuda, H. Noji, M. Yoshida, K. Kinosita Jr., and H. Itoh. Resolution of distinct rotational substeps by submillisedcond kinetic analysis of F_1-ATPase. *Nature*, 410:898, 2001.

[56] D. Andrieux and P. Gaspard. Fluctuation theorems and the nonequilibrium thermodynamics of molecular motors. *Phys. Rev. E*, 74:011906, 2006.

[57] P. Reimann. Brownian motors: noisy transport far from equilibrium. *Phys. Rep.*, 361:57, 2002.

[58] N. Tsuji, T. Oka, and H. Aoki. Nonequilibrium steady state of photoexcited correlated electrons in the presence of dissipation. *Phys. Rev. Lett.*, 103:047403, 2009.

[59] T. Nagatani. The physics of traffic jams. *Reports on Progress in Physics*, 65(9):1331, 2002.

[60] P. Jop, A. Petrosyan, and S. Ciliberto. Work and dissipation fluctuations near the stochastic resonance of a colloidal particle. *EPL*, 81(5):50005, 2008.

[61] S. Toyabe and E. Muneyuki. Nanosized free-energy transducer F_1-ATPase achieves 100% efficiency at finite time operation. *arXiv:1210.4017*, 2012.

[62] J. C. Crocker and D. G. Grier. Methods of digital video microscopy for colloidal studies. *Journal of Colloid and Interface Science*, 179(1):298 – 310, 1996.

[63] D. J. Evans, E. G. D. Cohen, and G. P. Morriss. Probability of second law violations in shearing steady states. *Phys. Rev. Lett.*, 71:2401, 1993.

[64] G. Gallavotti and E. G. D. Cohen. Dynamical ensembles in nonequilibrium statistical mechanics. *Phys. Rev. Lett.*, 74:2694, 1995.

[65] J. Kurchan. Fluctuation theorem for stochastic dynamics. *J. Phys. A: Math. Gen.*, 31:3719, 1998.

[66] J. L. Lebowitz and H. Spohn. A Gallavotti-Cohen-type symmetry in the large deviation functional for stochastic dynamics. *J. Stat. Phys.*, 95:333, 1999.

[67] T. Speck, V. Blickle, C. Bechinger, and U. Seifert. Distribution of entropy production for a colloidal particle in a nonequilibrium steady state. *EPL*, 79:30002, 2007.

[68] F. Douarche, S. Joubaud, N. B. Garnier, A. Petrosyan, and S. Ciliberto. Work fluctuation theorems for harmonic oscillators. *Phys. Rev. Lett.*, 97:140603, 2006.

[69] C. Jarzynski. Nonequilibrium equality for free energy differences. *Phys. Rev. Lett.*, 78:2690, 1997.

[70] G. E. Crooks. Entropy production fluctuation theorem and the nonequilibrium work relation for free energy differences. *Phys. Rev. E*, 60:2721, 1999.

[71] G. Hummer and A. Szabo. Free energy reconstruction from nonequilibrium single-molecule pulling experiments. *Proc. Natl. Acad. Sci. U.S.A.*, 98:3658, 2001.

[72] J. Liphardt, S. Dumont, S. B. Smith, I. Tinoco Jr, and C. Bustamante. Equilibrium information from nonequilibrium measurements in an experimental test of Jarzynski's equality. *Science*, 296:1832, 2002.

[73] D. Collin, F. Ritort, C. Jarzynski, S.B. Smith, I. Tinoco, and C. Bustamante. Verification of the Crooks fluctuation theorem and recovery of RNA folding free energies. *Nature*, 437:231, 2005.

[74] I. Junier, A. Mossa, M. Manosas, and F. Ritort. Recovery of free energy branches in single molecule experiments. *Phys. Rev. Lett.*, 102:070602, 2009.

[75] A. Alemany, M. Ribezzi, and F. Ritort. Recent progress in fluctuation theorems and free energy recovery. *AIP Proceedings conference*, 1332:96, 2011.

[76] K. Hayashi, H. Ueno, R. Iino, and H. Noji. Fluctuation theorem applied to F_1-ATPase. *Phys. Rev. Lett.*, 104:218103, 2010.

[77] H. Noji, R. Yasuda, M. Yoshida, and K. Kinosita. Direct observation of the rotation of F_1-ATPase. *Nature*, 386:299–302, 1997.

[78] R. Yasuda, H. Noji, K. Kinosita, and M. Yoshida. F_1-ATPase is a highly efficient molecular motor that rotates with discrete 120 degree steps. *Cell*, 93:1117, 1998.

[79] E. Zimmermann and U. Seifert. Efficiency of a molecular motor: A generic hybrid model applied to the F1-ATPase. *New J. Phys.*, 14:103023, 2012.

[80] G. Gallavotti. Chaotic hypothesis: Onsager reciprocity and fluctuation-dissipation theorem. *J. Stat. Phys.*, 84:899, 1996.

[81] R. Kubo, M. Toda, and N. Hashitsume. *Statistical Physics II.* Springer-Verlag, Berlin, 2nd edition, 1991.

[82] A. Einstein. Über die von der molekularkinetischen Theorie der Wärme geforderte Bewegung von in ruhenden Flüssigkeiten suspendierten Teilchen. *Ann. Phys.*, 17:549, 1905.

[83] H. Nyquist. Thermal agitation of electric charge in conductors. *Phys. Rev.*, 32:110, 1928.

[84] L. Onsager. Reciprocal relations in irreversible processes. I. *Phys. Rev.*, 37:405, 1931.

[85] L. Onsager. Reciprocal relations in irreversible processes. II. *Phys. Rev.*, 38:2265, 1931.

[86] H. B. Callen and T. A. Welton. Irreversibility and generalized noise. *Phys. Rep.*, 83(1):34–40, Jul 1951.

[87] L. F. Cugliandolo, J. Kurchan, and L. Peliti. Energy flow, partial equilibration, and effective temperatures in systems with slow dynamics. *Phys. Rev. E*, 55:3898, 1997.

[88] I. K. Ono, C. S. O'Hern, D. J. Durian, S. A. Langer, A. J. Liu, and S. R. Nagel. Effective temperatures of a driven system near jamming. *Phys. Rev. Lett.*, 89:095703, 2002.

[89] K. Hayashi and S. Sasa. Effective temperature in nonequilibrium steady states of Langevin systems with a tilted periodic potential. *Phys. Rev. E*, 69:066119, 2004.

[90] T. K. Haxton and A. J. Liu. Activated dynamics and effective temperature in a steady state sheared glass. *Phys. Rev. Lett.*, 99:195701, 2007.

[91] S. Fielding and P. Sollich. Observable dependence of fluctuation-dissipation relations and effective temperatures. *Phys. Rev. Lett.*, 88:050603, 2002.

[92] R. G. Larson. *The Structure and Rheology of Complex Fluids*. Oxford University Press, New York, 1999.

[93] R. Becker and W. Döring. Kinetische Behandlung der Keimbildung in übersättigten Dämpfen. *Ann. Phys.*, 416(8):719–752, 1935.

[94] J. Frenkel. *Kinetic theory of liquids*. Clarendon Pr., Oxford, 1947.

[95] S. P. Das. *Statistical Physics of Liquids at Freezing and Beyond*. Cambridge Univ. Press, 2011.

[96] J. K. G. Dhont. *An Introduction to Dynamics of Colloids*. Elsevier, Amsterdam, 1996.

[97] R. Brown. XXVII. A brief account of microscopical observations made in the months of June, July and August 1827, on the particles contained in the pollen of plants; and on the general existence of active molecules in organic and inorganic bodies. *Philosophical Magazine Series 2*, 4(21):161–173, 1828.

[98] M. von Smoluchowski. Zur kinetischen Theorie der Brownschen Molekularbewegung und der Suspensionen. *Ann. Phys.*, 326(14):756–780, 1906.

[99] J. Perrin. Mouvement brownien et réalité moléculaire. *Annales de Chimie et de Physique*, 18:5–104, 1909.

[100] P. Calabrese and A. Gambassi. Ageing properties of critical systems. *J. Phys. A: Math. Gen.*, 38:R133, 2005.

[101] K. Sekimoto. *Stochastic Energetics*. Springer-Verlag, Berlin, Heidelberg, 2010.

[102] A. W. C. Lau and T. C. Lubensky. State-dependent diffusion: Thermodynamic consistency and its path integral formulation. *Phys. Rev. E*, 76:011123, 2007.

[103] V. Y. Chernyak, M. Chertkov, and C. Jarzynski. Path-integral analysis of fluctuation theorems for general Langevin processes. *J. Stat. Mech.: Theor. Exp.*, page P08001, 2006.

[104] T. Harada and S. Sasa. Equality connecting energy dissipation with a violation of the fluctuation-response relation. *Phys. Rev. Lett.*, 95:130602, 2005.

[105] T. Speck, J. Mehl, and U. Seifert. Role of external flow and frame invariance in stochastic thermodynamics. *Phys. Rev. Lett.*, 100:178302, 2008.

[106] S. Toyabe, H.-R. Jiang, T. Nakamura, Y. Murayama, and M. Sano. Experimental test of a new equality: Measuring heat dissipation in an optically driven colloidal system. *Phys. Rev. E*, 75:011122, 2007.

[107] S. Toyabe, T. Okamoto, T. Watanabe-Nakayama, H. Taketani, S. Kudo, and E. Muneyuki. Nonequilibrium energetics of a single F_1-ATPase molecule. *Phys. Rev. Lett.*, 104:198103, 2010.

[108] H. Teramoto and S. Sasa. Microscopic description of the equality between violation of fluctuation-dissipation relation and energy dissipation. *Phys. Rev. E*, 72:060102, Dec 2005.

[109] J. M. Deutsch and O. Narayan. Energy dissipation and fluctuation response for particles in fluids. *Phys. Rev. E*, 74:026112, 2006.

[110] S. Toyabe and M. Sano. Energy dissipation of a Brownian particle in a viscoelastic fluid. *Phys. Rev. E*, 77:041403, 2008.

[111] K. Saito. Energy dissipation and fluctuation response in driven quantum Langevin dynamics. *EPL*, 83(5):50006, 2008.

[112] T. Harada. Macroscopic expression connecting the rate of energy dissipation with the violation of the fluctuation response relation. *Phys. Rev. E*, 79:030106, 2009.

[113] J. Rotne and S. Prager. Variational treatment of hydrodynamic interation in polymers. *J. Chem. Phys.*, 50:4831, 1969.

[114] M. Manghi, X. Schlagberger, Y.-W. Kim, and R. R. Netz. Hydrodynamic effects in driven soft matter. *Soft Matter*, 2:653, 2006.

[115] V. Blickle, T. Speck, U. Seifert, and C. Bechinger. Characterizing potentials by a generalized Boltzmann factor. *Phys. Rev. E*, 75:060101, 2007.

[116] P. E. Kloeden, E. Platen, and H. Schurz. *Numerical solution of SDE through computer experiments*. Springer-Verlag Berlin Heidelberg, 2003.

[117] L. Faucheux, G. Stolovitzky, and A. Libchaber. Periodic forcing of a Brownian particle. *Phys. Rev. E*, 51:5239, 1995.

[118] S. Ciliberto and C. Laroche. An experimental test of the Gallavotti-Cohen fluctuation theorem. *J. Phys. IV France*, 08:215–219, 1998.

[119] S. Ciliberto, N. Garnier, S. Hernandez, C. Lacpatia, J.-F. Pinton, and G. Ruiz Chavarria. Experimental test of the Gallavotti-Cohen fluctuation theorem in turbulent flows. *Physica A*, 340:240, 2004.

[120] K. Feitosa and N. Menon. Fluidized granular medium as an instance of the fluctuation theorem. *Phys. Rev. Lett.*, 92:164301, 2004.

[121] N. Kumar, S. Ramaswamy, and A. K. Sood. Symmetry properties of the large-deviation function of the velocity of a self-propelled polar particle. *Phys. Rev. Lett.*, 106:118001, 2011.

[122] S. Aumaitre, S. Fauve, S. McNamara, and P. Poggi. Power injected in dissipative systems and the fluctuation theorem. *Eur. Phys. J. B*, 19:449–460, 2001.

[123] C. Maes. On the origin and use of fluctuation relations for entropy. *Sém. Poincaré*, 2:29, 2003.

[124] C. Maes and K. Netocný. Time-reversal and entropy. *J. Stat. Phys.*, 110:269, 2003.

[125] T. Speck. The thermodynamics of small driven systems. *PhD Thesis*, 2007.

[126] S. Rahav and C. Jarzynski. Fluctuation relations and coarse-graining. *J. Stat. Mech.: Theor. Exp.*, page P09012, 2007.

[127] A. Puglisi, S. Pigolotti, L. Rondoni, and A. Vulpiani. Entropy production and coarse graining in Markov processes. *J. Stat. Mech.*, page P05015, 2010.

[128] M. Esposito. Stochastic thermodynamics under coarse-graining. *Phys. Rev. E*, 85:041125, 2012.

[129] R. Kawai, J. M. R. Parrondo, and C. van den Broeck. Dissipation: The phase-space perspective. *Phys. Rev. Lett.*, 98:080602, 2007.

[130] A. Puglisi, F. Cecconi, and A. Vulpiani. Models of fluidized granular materials: examples of non-equilibrium stationary states. *J. Phys. Cond. Mat.*, 17:S2715–S2730, 2005.

[131] A. Kundu, S. Sabhapandit, and A. Dhar. Application of importance sampling to the computation of large deviations in nonequilibrium processes. *Phys. Rev. E*, 83:031119, 2011.

[132] S. Sabhapandit. Heat and work fluctuations for a harmonic oscillator. *Phys. Rev. E*, 85:021108, 2012.

[133] A. Pal and S. Sabhapandit. Work fluctuations for a Brownian particle in a harmonic trap with fluctuating locations. *Phys. Rev. E*, 87:022138, 2013.

[134] K. Kawaguchi and Y. Nakayama. Fluctuation theorem for hidden entropy production. *arXiv: 1209.6333*, 2012.

[135] J. Kurchan. In and out of equilibrium. *Nature*, 433(7023):222–225, 2005.

[136] G. S. Agarwal. Fluctuation-dissipation theorems for systems in non-thermal equilibrium and applications. *Z. Physik*, 252:25, 1972.

[137] P. Hänggi and H. Thomas. Stochastic processes: Time evolution, symmetries and linear response. *Phys. Rep.*, 88:207, 1982.

[138] A. Crisanti and F. Ritort. Violation of the fluctuation-dissipation theorem in glassy systems: basic notions and the numerical evidence. *J. Phys. A: Math. Gen.*, 36:R181, 2003.

[139] U. Marconi, A. Puglisi, L. Rondoni, and A. Vulpiani. Fluctuation-dissipation: Response theory in statistical physics. *Phys. Rep.*, 461:111–195, 2008.

[140] T. Speck and U. Seifert. Extended fluctuation-dissipation theorem for soft matter in stationary flow. *Phys. Rev. E*, 79:040102(R), 2009.

[141] J. Prost, J.-F. Joanny, and J. M. R. Parrondo. Generalized fluctuation-dissipation theorem for steady-state systems. *Phys. Rev. Lett.*, 103:090601, 2009.

[142] T. Speck. Driven soft matter: Entropy production and the fluctuation-dissipation theorem. *Progr. Theor. Phys. Suppl.*, 184:248–261, 2010.

[143] G. Szamel. Self-diffusion in sheared colloidal suspensions: Violation of fluctuation-dissipation relation. *Phys. Rev. Lett.*, 93:178301, 2004.

[144] R. Mauri and D. Leporini. Violation of the fluctuation-dissipation theorem in confined driven colloids. *Europhys. Lett.*, 76:1022, 2006.

[145] M. Krüger and M. Fuchs. Fluctuation dissipation relations in stationary states of interacting Brownian particles under shear. *Phys. Rev. Lett.*, 102(13):135701, 2009.

[146] M. Zhang and G. Szamel. Effective temperatures of a driven, strongly anisotropic Brownian system. *Phys. Rev. E*, 83:061407, 2011.

[147] A. Ziehl, J. Bammert, L. Holzer, C. Wagner, and W. Zimmermann. Direct measurement of shear-induced cross-correlations of Brownian motion. *Phys. Rev. Lett.*, 103(23):230602, Dec 2009.

[148] R. Kubo. Fluctuation-dissipation theorem. *Rep. Progr. Phys.*, 29:255, 1966.

[149] L. Onsager and S. Machlup. Fluctuations and irreversible processes. *Phys. Rev.*, 91:1505, 1953.

[150] G. I. Taylor. Dispersion of soluble matter in solvent flowing slowly through a tube. *Proc. R. Soc. London A*, 219:186, 1953.

[151] F. El Azhar, M. Baus, J.-P. Ryckaert, and E. J. Meijer. Line of triple points for the hard-core Yukawa model: A computer simulation study. *J. Chem. Phys.*, 112(11):5121–5126, 2000.

[152] M. P. Allen and D. J. Tildesley. *Computer Simulation of Liquids*. Clarendon Press, Oxford, 1987.

[153] D. R. Foss and J. F. Brady. Brownian dynamics simulation of hard-sphere colloidal dispersions. *Journal of Rheology*, 44:629–651, 2000.

[154] D. M. Heyes. Some physical consequences of large shear rates on simple liquids. *J. Chem. Phys.*, 85:997, 1986.

[155] P. T. Cummings, B. Y. Wang, D. J. Evans, and K. J. Fraser. Nonequilibrium molecular dynamics calculation of self-diffusion in a non-Newtonian fluid subject to a Couette strain field. *J. Chem. Phys.*, 94:2149, 1991.

[156] S. R. Rastogi, N. J. Wagner, and S. R. Lustig. Rheology, self-diffusion, and microstructure of charged colloids under simple shear by massively parallel nonequilibrium Brownian dynamics. *J. Chem. Phys.*, 104(22):9234–9248, 1996.

[157] X. Qiu, H. D. Ou-Yang, D. J. Pine, and P. M. Chaikin. Self-diffusion of interacting colloids far from equilibrium. *Phys. Rev. Lett.*, 61(22):2554–2557, Nov 1988.

[158] R. Besseling, E. R. Weeks, A. B. Schofield, and W. C. K. Poon. Three-dimensional imaging of colloidal glasses under steady shear. *Phys. Rev. Lett.*, 99(2):028301, Jul 2007.

[159] A. V. Indrani and S. Ramaswamy. Shear-induced enhancement of self-diffusion in interacting colloidal suspensions. *Phys. Rev. E*, 52(6):6492–6496, Dec 1995.

[160] J. F. Morris and J. F. Brady. Self-diffusion in sheared suspensions. *J. Fluid Mech.*, 312:223, 1996.

[161] J. Bławzdziewicz and M. L. Ekiel-Jeżewska. How shear flow of a semidilute suspension modifies its self-mobility. *Phys. Rev. E*, 51(5):4704–4708, 1995.

[162] T. G. M. van de Ven and S. G. Mason. The microrheology of colloidal dispersions. *Colloid and Polymer Science*, 255:794–804, 1977.

[163] E. J. Hinch. *Pertubation Methods*. Cambridge texts in applied mathematics, 1991.

[164] M. D. Ediger, C. A. Angell, and Sidney R. Nagel. Supercooled liquids and glasses. *J. Phys. Chem.*, 100(31):13200–13212, 1996.

[165] K. Schätzel and B. J. Ackerson. Density fluctuations during crystallization of colloids. *Phys. Rev. E*, 48:3766–3777, 1993.

[166] J. L. Harland and W. van Megen. Crystallization kinetics of suspensions of hard colloidal spheres. *Phys. Rev. E*, 55:3054–3067, 1997.

[167] C. Sinn, A. Heymann, A. Stipp, and T. Palberg. Solidification kinetics of hard-sphere colloidal suspensions. *Prog. Colloid Polym. Sci.*, 118:266, 2001.

[168] U. Gasser, E. R. Weeks, A. Schofield, P. N. Pusey, and D. A. Weitz. Real-space imaging of nucleation and growth in colloidal crystallization. *Science*, 292:258, 2001.

[169] U. Gasser. Cyrstallization in three- and two-dimensional colloidal suspensions. *J. Phys.: Condens. Matter*, 21:203101, 2009.

[170] A. Onuki. Phase transitions of fluids in shear flow. *J. Phys.: Condens. Matter*, 9:6119, 1997.

[171] J. Vermant and M. J. Solomon. Flow-induced structure in colloidal suspensions. *J. Phys.: Condens. Matter*, 17:R187–R216, 2005.

[172] S. Butler and P. Harrowell. Factors determining crystal-liquid coexistence under shear. *Nature*, 415(6875):1008–1011, 2002.

[173] S. Butler and P. Harrowell. Simulation of the coexistence of a shearing liquid and a strained crystal. *J. Chem. Phys.*, 118(9):4115–4126, 2003.

[174] J. F. Lutsko and G. Nicolis. Theoretical evidence for a dense fluid precursor to crystallization. *Phys. Rev. Lett.*, 96:046102, 2006.

[175] T. Schilling, H. J. Schöpe, M. Oettel, G. Opletal, and I. Snook. Precursor-mediated crystallization process in suspensions of hard spheres. *Phys. Rev. Lett.*, 105:025701, 2010.

[176] W. Lechner, C. Dellago, and P. G. Bolhuis. Role of the prestructured surface cloud in crystal nucleation. *Phys. Rev. Lett.*, 106:085701, 2011.

[177] J. Russo and H. Tanaka. The microscopic pathway to crystallization in supercooled liquids. *Sci. Rep.*, 2, 2012.

[178] S. Auer and D. Frenkel. Quantitative prediction of crystal-nucleation rates for spherical colloids: A computational approach. *Annu. Rev. Phys. Chem.*, 55:333, 2004.

[179] P. D. Kaplan, J. L. Rouke, A. G. Yodh, and D. J. Pine. Entropically driven surface phase separation in binary colloidal mixtures. *Phys. Rev. Lett.*, 72:582, 1994.

[180] A. D. Dinsmore, P. B. Warren, W. C. K. Poon, and A. G. Yodh. Fluid-solid transitions on walls in binary hard-sphere mixtures. *Europhys. Lett.*, 40:337, 1997.

[181] S. Auer and D. Frenkel. Line tension controls wall-induced crystal nucleation in hard-sphere colloids. *Phys. Rev. Lett.*, 91:015703, 2003.

[182] A. Cacciuto, S. Auer, and D. Frenkel. Onset of heterogeneous crystal nucleation in colloidal suspensions. *Nature*, 428:404, 2004.

[183] S. Auer and D. Frenkel. Suppression of crystal nucleation in polydisperse colloids due to increase of the surface free energy. *Nature*, 413:711, 2001.

[184] C. Dellago, P. G. Bolhuis, and P. L. Geissler. Transition path sampling. *Adv. Chem. Phys.*, 123:1, 2002.

[185] A. C. Pan and D. Chandler. Dynamics of nucleation in the Ising model. *J. Phys. Chem. B*, 108:19681, 2004.

[186] R. J. Allen, P. B. Warren, and P. R. ten Wolde. Sampling rare switching events in biochemical networks. *Phys. Rev. Lett.*, 94:018104, 2005.

[187] R. J. Allen, C. Valeriani, and P. R. ten Wolde. Forward flux sampling for rare event simulations. *J. Phys.: Condens. Matter*, 21:463102, 2009.

[188] G. M. Torrie and J. P. Valleau. Non-physical sampling distributions in Monte-Carlo free-energy estimation - umbrella sampling. *J. Comput. Phys.*, 23:187–199, 1977.

[189] D. Frenkel and B. Smit. *Understanding Molecular Simulation: From Algorithms to Applications*. Academic Press, San Diego, 2002.

[190] M. O. Robbins, K. Kremer, and G. S. Grest. Phase diagram and dynamics of Yukawa systems. *J. Chem. Phys.*, 88:3286, 1988.

[191] E. J. Meijer and D. Frenkel. Melting line of Yukawa system by computer simulation. *J. Chem. Phys.*, 94:2269, 1991.

[192] L. V. Woodcock. Entropy difference between the face-centred cubic and hexagonal close-packed crystal structures. *Nature*, 385(6612):141–143, 1997.

[193] J. Zhu, M. Li, R. Rogers, W. Meyer, R. H. Ottewill, STS-73 Space Shuttle Crew, W. B. Russel, and P. M. Chaikin. Crystallization of hard-sphere colloids in microgravity. *Nature*, 387(6636):883–885, 1997.

[194] W. Ostwald. Studien über die Bildung und Umwandlung fester Körper. *Z. Phys. Chem.*, 22:289, 1897.

[195] P. R. ten Wolde and D. Frenkel. Homogeneous nucleation and the Ostwald step rule. *Phys. Chem. Chem. Phys.*, 1:2191, 1999.

[196] P. J. Steinhardt, D. R. Nelson, and M. Ronchetti. Bond-orientational order in liquids and glasses. *Phys. Rev. B*, 28:2, 1983.

[197] W. Lechner and C. Dellago. Accurate determination of crystal structures based on averaged local bond order parameters. *J. Chem. Phys.*, 129:114707, 2008.

[198] P. R. ten Wolde and M. J. Ruiz-Montero. Numerical calculation of the rate of crystal nucleation in a Lennard-Jones system at moderate undercooling. *J. Chem. Phys.*, 104:9932, 1996.

[199] R. L. Jack, M. F. Hagan, and D. Chandler. Fluctuation-dissipation ratios in the dynamics of self-assembly. *Phys. Rev. E*, 76:021119, 2007.

[200] M. Radu and T. Schilling. Solvent hydrodynamics affect crystal nucleation in suspensions of colloidal hard-spheres. *arXiv:1301.5592*, 2013.

[201] A. Brünger, C. L. Brooks, and M. Karplus. Stochastic boundary conditions for molecuar dynamics simulations. *Chem. Phys. Lett.*, 105:495, 1984.

[202] P. Strating. Brownian dynamics simulation of a hard-sphere suspension. *Phys. Rev. E*, 59:2175, 1999.

Danksagung

Schließlich möchte ich allen danken, die zum Gelingen dieser Arbeit beigetragen haben. Besonderer Dank gilt hierbei

- Herrn Prof. Dr. Seifert für die Ermöglichung dieser Arbeit, die wissenschaftliche Betreuung und das gute Arbeitsklima,
- Dr. Thomas Speck für die sehr kompetente Betreuung,
- Herrn Jun.-Prof. Dr. Axel Arnold für die Übernahme und das Erstellen des Mitberichts,
- Herrn Prof. Dr. Bechinger für die gelungene Zusammenarbeit,
- David Abreu, Dr. Valentin Blickle und Dr. Jakob Mehl für die vielen Gespräche und Diskussionen nicht nur über Physik,
- Anja Steinhauser für die stets freundliche Hilfe bei allen organisatorischen Fragen,
- Timo Bihr und Robert Wulfert für die gute Zusammenarbeit bei der Systemadministration,
- David Abreu, Timo Bihr, Felix Lander, Dr. Jakob Mehl, Daniel Schmidt, Robert Wulfert und Eva Zimmermann für das Korrekturlesen der Arbeit und dem ganzen Institut für eine schöne Zeit!
- Meinen Eltern Maritta und Berthold Lander sowie meiner Frau Diana danke ich für die Unterstützung während der gesamten Zeit.

Ehrenwörtliche Erklärung

Ich erkläre, dass ich diese Arbeit selbstständig verfasst habe und keine anderen als die angegebenen Quellen und Hilfsmittel verwendet habe.

Stuttgart, den 09. April 2013 Boris Lander